Australian National University

Interactions of crude oil and salt solutions with mineral surfaces

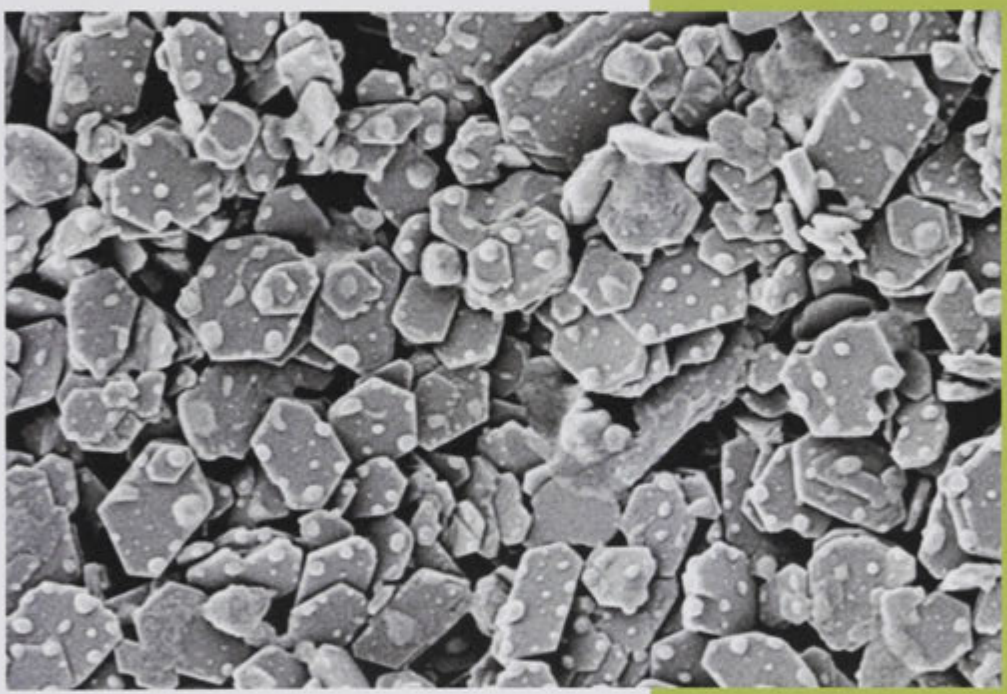

Evgenia V. Lebedeva

A thesis submitted for the degree of
Doctor of Philosophy of
The Australian National University

August 2011

(The front page shows a SEM image of a kaolinite-coated substrate decorated by crude oil nano-droplets).

Preface

This thesis is an account of research carried out at the Department of Applied Mathematics, Research School of Physics and Engineering, within the Australian National University.

The thesis represents my original work; however, some aspects were undertaken in collaboration:

The work in Chapter 2 on salt effects at carbonate surfaces was performed under the supervision of Prof. Mark Knackstedt and Prof. Tim Senden, and in collaboration with a group from the Department of Chemical and Petroleum Engineering, University of Wyoming, led by Prof. Norman Morrow. In Chapter 2 the analysis of calcite surfaces was carried out at the Ian Wark Research Institute, University of South Australia, in collaboration with Dr John Denman, where he assisted with the use of Time of Flight Secondary Ion Mass Spectrometry. Michael Turner (ANU) assisted with the micro-Computed Tomography (micro-CT) and some aspects of sample preparation.

The work in Chapters 3-6 was performed under the supervision of Dr. Andrew Fogden. Michael Turner, Jill Middleton, Adrian Sheppard and Mark Knackstedt (ANU) helped with some aspects of the micro-CT analysis.

This thesis does not contain material that has been accepted for the award of any other degree or diploma in any university. To the best of my knowledge, it includes no material previously published or written by another person, except where due reference or acknowledgement is made in the text.

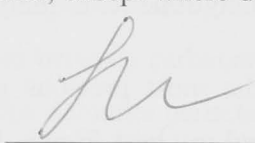

Evgenia Lebedeva

31 August 2011

Acknowledgements

It is a pleasure for me to thank everyone who directly or indirectly helped me with this work. Firstly, I am incredibly indebted to my supervisor, Andrew Fogden, who gave ideas for most of the projects, helped me to design and carry out experiments, and was always ready to help, answer any stupid question with patience and in detail, gave advice and supported me at all times.

I was very fortunate and privileged to study at the Australian National University and in particular, be a part of the Department Applied Mathematics and work among the best scientists and people. I thank Mark Knackstedt for giving me this opportunity and helping to start my research, together with Tim Senden and Norm Morrow (University of Wyoming), and I am very proud of working together with such brilliant people. Jill Middleton was always ready to help, together with Adrian Sheppard, Andrew Kingston, Shane Latham, Holger Averdunk, Paul Veldkamp, Rob Sok, Trond Varslot, Tim Sawkins and Anthony Hyde. Lab times were never boring if Michael Turner, Shaun Howard and Munish Kumar were there. Jan James and Margo Davis were reliable on all occasions. I always enjoyed listening to the incredible stories of Vince Craig and Stephen Hyde, and speaking in Russian with Drew Parsons, though I understood him better when he spoke English. Every single member of the Department, with whom I had chance to interact, made an important input to my progress and I am very grateful to everyone. Of course, I would not have survived without the constant support on all matters from people who became, I can proudly call, my friends - Vivianne Deniz, Abid Ghous, Anthony Jones and Mahyar Madadi.

Thanks to the most precious people in my life - my mother Elena and grandma Valentina, and my best friends from Russia – Olga Kudryavtzeva, Nadya Popova and Liza Tritentko for staying in touch and being fantastic friends throughout all these years. Thanks to my former Russian supervisor Michael Zhurba for letting me go to Australia and start a new PhD project.

The member companies of Digital Core Consortium/Wettability Satellite are thanked for expressing interest in our research and providing funding.

Abstract

Understanding the fundamental interactions of liquids with mineral surfaces and their relation to larger scale mechanisms and phenomena in porous media is relevant to a wide range of applications in oil recovery, soil remediation, water filtration and other areas. Most previous imaged-based studies related to these applications were limited to two-dimensional space and rarely included multi-scale observations. Studies of idealised systems, comprising monomineralic model porous media containing simple liquids such as salt solutions and model oils, have been successful in demonstrating predictable and reproducible trends. However, once the system is set closer to real environmental conditions, using realistically complex porous media in which several minerals are present, and including variable aqueous conditions (e.g. salinity, ion valency or pH) and complex oils (e.g. crude oil), the results typically become too difficult to interpret and therefore to predict. This thesis aims to unravel some of these complexities associated with the physics and chemistry of aqueous and hydrocarbon phases and mineralogy. The studies further underline the importance of interfacial interactions for industrial processes in porous media, which include carbonate and/or silicate minerals.

In the first part of the thesis, sandstone cemented with dolomite and anhydrite was the porous medium for a case study of the effect of salinity on particle mobilisation. Rock samples were imaged with micro-CT before and after flooding with salt solutions, and analysed digitally. Significant redistribution of the carbonate phase was observed after flooding, due to partial dissolution. This study was complimented by Atomic Force Microscopy (AFM) measurements of the adhesion forces between carbonate and quartz surfaces to better understand the initial attraction between dolomite particles and quartz grains. The experiments showed that sulphate salts with monovalent cations give rise to a strong attraction.

The second part of the thesis was devoted to systems relevant to silicate minerals, in particular kaolinite and quartz, in contact with both an aqueous phase (salt solutions) and crude oil. The major focus was on the wettability alteration of such minerals, and its dependence on salinity, ion valency, pH and waterflooding. Wettability alteration was characterised by contact angle measurements and imaging of adsorbed/deposited crude oil polar compounds by scanning electron microscopy (SEM) and AFM. To study

kaolinite wettability, a special procedure for kaolinite substrate preparation was developed, giving thin and smooth kaolinite coats, which remained stable in contact with liquids. The results showed that the wettability alteration of kaolinite by crude oil was generally similar to quartz, displaying a decrease in oil-wetness with increase in salinity and pH of the aqueous phase. The adsorption/deposition from crude oil generally followed similar trends to the contact angles. The nano-scale deposition on kaolinite displayed different localities depending on ion valency and concentration of the salt solution. At high concentrations of sodium ions, deposits tended to accumulate at the edges of all kaolinite platelets. Higher concentrations of calcium ions led to deposition mainly on the uppermost platelet faces, while the layers below remained largely pristine. The effect of subsequent waterflooding on wettability alteration was studied on glass and sandstone substrates. The preparation procedures developed consistently showed that initial wettability alteration towards oil-wetness decreases, and its flooding-induced reversal towards water-wetness increases, with rising salinity and pH of the aqueous phase, again in line with expectations from the interfacial electrostatic interactions. Oil deposits after flooding were distributed as nano-blobs, with their substrate coverage and size similarly dependent on salinity and pH. It was found that the use of organic solvents to remove the bulk oil to inspect the deposits can introduce preparation artifacts, which can result in overestimation of deposit coverage. Analogous experiments on sandstone rock samples supported all findings for the glass model substrates. The final part of the thesis unified these new methodologies for wettability analysis with micro-CT analysis to study the pore-scale distribution of residual crude oil in sand pack plugs after waterflooding and relate this to their wettability state. The results showed that even a very small fraction of kaolinite in the sand can have a substantial effect on oil recovery and wettability during waterflooding.

List of papers

Journals

1. Lebedeva, E.V., Fogden, A. Micro-CT and wettability analysis of oil recovery from sand packs and the effect of waterflood salinity and kaolinite. *Energy & Fuels* (Manuscript submitted).

2. Lebedeva, E.V., Fogden, A. Nano-scale structure of crude oil deposits on water-wet substrates: Dependence on aqueous phase and organic solvents. *Colloids & Surfaces A* **2011**, *380*, 280-291.

3. Lebedeva, E.V., Fogden, A. Wettability alteration of kaolinite exposed to crude oil in salt solutions. *Colloids & Surfaces A* **2011**, *377*,115-122.

4. Lebedeva, E.V., Fogden, A. Adhesion of oil to kaolinite in water. *Environmental Science & Technology* **2010**, *44*, 9470–9475.

Conference Proceedings

1. Fogden, A., Lebedeva, E.V. Changes in wettability state due to waterflooding. *International Symposium of the Society of Core Analysis*, 18-21 September, Austin, Texas, USA. **2011**, SCA2011-15 (Accepted).

2. Lebedeva E.V., Fogden, A., Senden, T.J., Knackstedt, M.A. Kaolinite wettability – the effect of salinity, pH and calcium. *International Symposium of the Society of Core Analysis*, 4-7 October, Halifax, Nova Scotia, Canada. **2010**, SCA2010-11.

3. Lebedeva E.V, Senden T.J., Knackstedt, M.A., Morrow, N.R. Improved oil recovery from Tensleep sandstone: studies of brine-rock interactions by micro-CT and AFM. *15th European Symposium on Improved Oil Recovery*, 27-29 April, Paris, France, **2009**.

Contents

List of tables

List of figures

1 Introduction

This thesis uses a multi-scale approach to study brine-oil-rock systems to aid in connecting phenomena at the core-scale, pore-scale and molecular-scale, in particular to improve understanding of oil recovery from reservoirs by waterflooding. Given the various complexities of rock structure and mineralogy, crude oil composition and their interactions with multicomponent brines, interpretation of the mechanisms of multiphase transport is far from straightforward. When brine is injected into the reservoir formation, a multitude of phenomena may simultaneously accompany and affect oil recovery, such as dissolution/precipitation, particle mobilisation and adsorption/desorption of oil components from pore walls. This work aims to analyse these sub-processes separately, using model substrates to better understand the fundamental surface chemical aspects of them, and apply this insight to interpret behaviour in realistic rock systems.

1.1 Particle mobilisation during waterflooding

Mobilisation of fine mineral particles is of significant importance to the petroleum industry, as released fines can migrate and plug regions in the formation, causing damage and hence reduction in production (1), or vice versa, improve sweep efficiency of the oil recovery (2). Fines migration can be triggered by flow rate, pH, temperature and/or change in brine ion composition. Fines migration triggered by flow rate is typical for drainage zones close to the well, particularly in highly permeable rocks, whereas in regions further from that zone, aqueous-mineral interactions due to change in pH and ion composition could become more dominant. The interface between mineral and aqueous phase is semi-quantitatively described by the Derjaguin-Landau-Verwey-Overbeek (DLVO) theory. The electrical double layer at this interface is determined by the surface charge, the decay of the electrostatic potential away from the surface, and the concentration and distribution of cations and anions in both the compact (Stern) and diffuse (Gouy-Chapman) layers needed to neutralise the surface charge, as a function of pH and ion concentration (3). Presumably, uncemented fines are initially attached to

grain surfaces by attractive van der Waals forces, which prevail at high electrolyte concentrations (4). If the electrolyte concentration decreases then the repulsive double layer forces become stronger and help fines to detach from the grain surface. Brine compositional changes can also dissolve mineral cements to thus liberate fines. The major challenge is to relate small-scale measurements at aqueous-mineral interfaces to macroscopic processes. The basic compositional and structural features of many geochemically important systems remain poorly understood.

1.2 Rock wettability

Wettability is the tendency of one fluid, e.g. crude oil, to spread preferentially over a substrate, e.g. rock surface, in the presence of a second immiscible fluid, e.g. connate or injected brine. Wettability affects relative permeability, electrical properties, nuclear magnetic resonance relaxation times and saturation profiles in the reservoir. The wettability state of a reservoir greatly impacts recovery by waterflooding or spontaneous imbibition. Wettability of a smooth, flat mineral surface is usually measured by the contact angle of an oil drop in the brine. The subset of minerals available in such ideal form is very limited (e.g. mica and calcite). Wettability characterisation is thus problematic for other clay minerals such as kaolinite, which is very widespread in sandstone reservoirs. Wettability can also be defined at the core-scale, for which the most popular methods are the Amott and USBM (U.S. Bureau of Mines) tests. The Amott test estimates the amount of water or oil spontaneously or forcibly imbibed, while the USBM test estimates the work required to do the imbibitions. However, the major limitation of core-scale tests is that they do not give any information on local oil and water distribution or surface chemistry within the rock. While multiphase flow in strongly water-wet or oil-wet porous media is widely studied, most reservoirs are thought to be in neither of these extreme states. Instead, a mixed-wet state is presumed to be most common. This state can naturally arise from the distribution of oil and brine in the reservoir, with rock pore surface subareas in contact with oil being prone to wettability alteration by adsorption/deposition of crude oil polar components. This propensity for wettability alteration depends on the local oil-brine-mineral interactions. This aspect is of particular relevance to secondary or tertiary recovery by waterflooding, during which the rock surface may experience sequential exposure to oil and to brines of varying ion composition and pH, and thus varying wettability-alterating tendency.

1.3 Thesis outline

The effect of various aqueous environments on the interaction of mineral surfaces with each other and with crude oil was studied at multiple scales in 2D and 3D using model substrates and rocks by a combination of micro-tomographic, microscopic and spectroscopic techniques, as mentioned below.

Chapter 2 focuses on the molecular-scale interactions of carbonate minerals with quartz surfaces in various salt solutions and their possible effects on the spatial distribution of carbonate phase in a sandstone rock at the pore-scale and core-scale. Adhesion forces between model mineral surfaces were measured using Atomic Force Microscopy (AFM). The extent of ion adsorption onto these carbonate surfaces was quantified by Time of Flight Secondary Ion Mass Spectrometry (ToF-SIMS). Finally, the distribution and mobilisation of carbonate phase due to flooding with high and low salinity solutions was imaged with micro-Computed Tomography (micro-CT) and interpreted in terms of the interactions.

Chapter 3 focuses on the short-term wettability alteration of kaolinite surfaces due to crude oil in various salt solutions. A method for preparing kaolinite substrates in the form of a uniform, thin, smooth coat of kaolinite platelets on glass, suitable for surface chemical analysis, was developed. These model substrates were characterised with AFM and white-light profilometry. Wettability alteration was assessed by measuring oil drop contact angles.

Chapter 4 continues and extends the wettability studies of the kaolinite model substrates in Chapter 3. The analysis of wettability alteration now focused on identification of the extent and the location of the adsorbed/deposited polar components of the crude oil after long-term exposure. High-resolution imaging of these nanoscopic deposits was performed with Field Emission Scanning Electron Microscopy (FESEM) and AFM. Deposit amount was determined by fluorescence spectroscopy and related to measured contact angles.

Chapter 5 further extends the studies in Chapters 3 and 4 of wettability alteration due to crude oil as a function of aqueous environments, by addressing the effect of waterflooding on its state, and combining model silicate substrates with sandstone rock. Four preparation procedures were developed for analysis of wettability alteration by crude oil and changes in this initial wettability state due to flooding with various salt

solutions. Wettability was again characterised by FESEM and AFM of deposits and contact angle goniometry of oil drops, to quantify the influence of waterflooding and the solvent rinsing procedures used to remove bulk oil.

Chapter 6 analyses the residual distribution of crude oil after high and low salinity flooding of model rocks. Micro-CT experiments were performed on quartz sand packs without or with their grains lined with kaolinite. The amount and location of residual oil were correlated to the effect of salinity and kaolinite on the wettability of the grains using uncoated and kaolinite-coated model substrates, analysed with the techniques developed in Chapters 3-5.

2 Salt effects at carbonate surfaces

Chapter 2 is divided into two parts, the first one (Chapter 2.1) of which investigates surface chemical interactions between model quartz and carbonate substrates in various salts, using microscopic and spectroscopic techniques. The second part (Chapter 2.2) studies possible implications of these interactions at quartz and carbonate surfaces for macro-scale rock structure and its changes.

2.1 Reactions at interfaces

2.1.1 Introduction

Any member of the family of minerals that contain the carbonate ion, CO_3^{2-}, as the basic structural and compositional unit is called a carbonate mineral. The carbonates are among the most widely distributed minerals in the Earth's crust and make up 10-15% of sedimentary rocks. Over 90% of the carbonate sediments found are biological in origin and form under marine conditions (5; 6; 7). These sediments generally are deposited near the site of their origin. Carbonate rocks largely consist of two types: limestones, which are composed mostly of calcite ($CaCO_3$) or high magnesium calcite [$(Ca,Mg)CO_3$], and dolostones, which are composed mostly of dolomite [$CaMg(CO_3)_2$].

The dissolution and precipitation behaviour of calcite has been widely studied (8; 9), since it plays an important role in rock weathering and soil chemistry, and therefore these processes impose controls on the natural sequestration of CO_2. At depth, the precipitation of calcite underlies processes in diagenesis such as pressure solution compaction, stylolite formation, and crack healing in calcite-bearing sediments and rocks. The growth of biogenic calcium carbonate in shells and corals within marine environments provides the starting material for the formation of limestone.

Chemical interactions occurring at or near the solid-aqueous interface exert major influences on the behaviour of carbonate minerals in natural environments (10). The interface of a solid in contact with a solution represents a discontinuity in the system that has unique characteristics. The surface of a solid or liquid is a region where

structure is disrupted and bonding requirements are not satisfied in a manner typical of the bulk phase. Because of the excess free energy and disrupted bonding occurring in the surficial region, it is a particularly likely area for interaction to occur. Studies of calcite (11) showed that its surface structure does not vary over a broad pH range, other than in the degree of protonation, contradicting earlier conclusions about calcite surface species (12).

Different ions in electrolytes react differently with carbonates in aqueous environments, which can lead to carbonate precipitation or dissolution. Surface reactions of metal ions with calcite are inherently more complicated than pure calcite kinetics, because dissolution (of the calcite) and growth (of the new metal carbonate) can occur simultaneously, and the new phase itself may be either pure or a solid solution (13).

In Chapter 2.1, interfacial interaction forces between carbonate and quartz model substrates were measured in 29 salt solutions of various ion valency and concentrations using Atomic Force Microscopy (AFM). The extent of ion adsorption onto carbonate surfaces was then measured for 10 salt solutions with Time of Flight Secondary Ion Mass Spectrometry (ToF-SIMS).

2.1.2 Materials and methods

Substrates

Calcite has been a substrate of choice for AFM and ToF-SIMS studies because it is naturally abundant, geochemically important, and easily cleaves into locally monomolecular planes with well-defined lattice structure and surface chemistry. For AFM, calcite ($CaCO_3$) and dolomite ($CaMgCO_3$) substrates were prepared by gluing small cleaved pieces (~4x4 mm^2) onto cover glass (diameter 10 mm, thickness 0.17 mm; Smiec, China) with non-volatile epoxy melt (Epon, Shell), then gluing the glass onto a steel mounting stub with double-sided tape. Finally, the substrate was cleaned with high-pressure CO_2 snow followed by water-vapour plasma (18MHz, 10W for 30s, P_{H2O}=0.065 Torr, P_{Ar}=0.02 Torr) immediately prior to use. For ToF-SIMS, freshly cleaved calcite and dolomite samples were soaked in brine solution for 18 h., then immersed in MilliQ water for 1 s, and then dried with N_2.

Salt solutions

The aqueous salt solutions were made from analytical grade chemicals in MilliQ water at their natural pH (5.7±0.3). The salt combinations studied by AFM and ToF-SIMS are

summarised in Table 2.1.

Table 2.1. *Matrix of salt solutions tested, with + indicating solutions for AFM experiments and ● indicating solutions for ToF-SIMS experiments.*

Concentration, M / Salt	0	0.001	0.005	0.0075	0.01	0.05	0.1	0.15	1
Calcite									
NaCl			+	+	+	+	+	+	
KCl		●			+		+		●
LiCl			+		+		+		
$CaCl_2$			+	+	+	+	+	+	
$MgCl_2$					+				
$LaCl_3$			+	+		+	+	+	
Na_2SO_4	●	●			+ ●		+ ●		●
K_2SO_4					+		+		
$MgSO_4$					+		+		●
Dolomite									
KCl					+		+		●
$CaCl_2$					+		+		
$MgCl_2$					+		+		
Na_2SO_4					+		+		●
$MgSO_4$					+		+		

AFM

A Multimode NanoScopeIIIa (Veeco, Inc., Santa Barbara, CA) was used to image cleaved calcite or dolomite surfaces and to measure adhesion forces between silica and calcite/dolomite in different brines. All experiments were conducted at ambient temperature (20±2 ^{o}C). The ultra-sharp "golden" silicon cantilevers (NT-MPT Co., Russia) with a low nominal spring constant of 0.1 N/m, and the fluid cell, were both cleaned with water-vapour plasma to eliminate any organic contamination before each experiment. Imaging of the calcite was performed for all solution conditions, and there was no discernible variation in calcite topography. Water was used as a control.

ToF-SIMS

Experiments were performed with a Gallium source at 15kV in vacuum ($2.5x10^{-8}$ Torr). Surface spectroscopy analysis was carried out at first for positive ions on 6 spots, and then for negative ions also on 6 spots, with raster size 100x100 μm^2. Depth profiles were conducted at 15-25 min. acquisition time, with electron neutralisation applied (5 s

of sputter, 5 s of compensate). Pure calcite was used as a control sample.

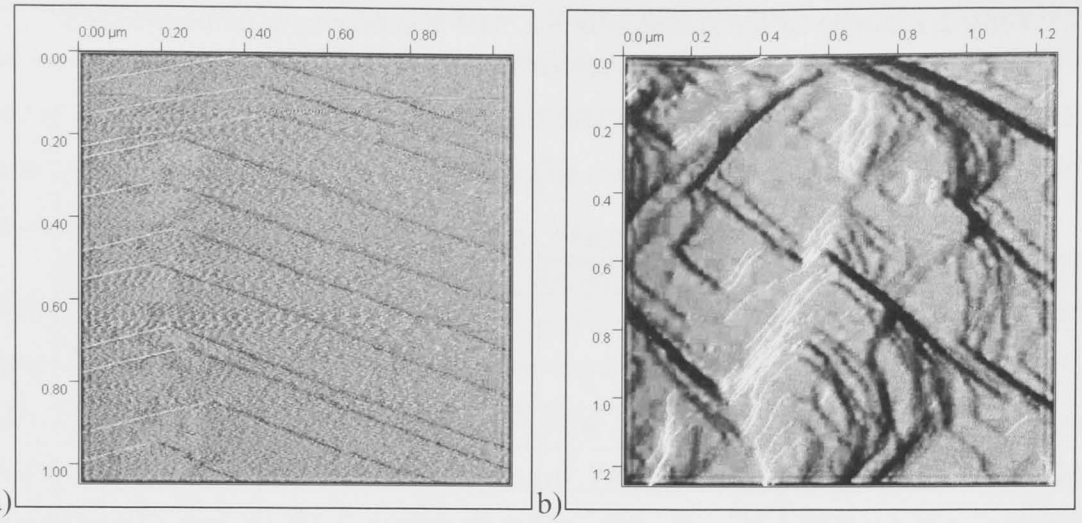

a) b)

Figure 2.1. *AFM images of a) calcite and b) dolomite surfaces under water, showing areas of approximately 1x1 μm^2.*

2.1.3 Results and discussion

AFM images of freshly cleaved calcite and dolomite under water are presented in Figure 2.1. Figure 2.2 summarises the results of AFM adhesion measurements between the silica tip and calcite or dolomite surface. Each such point on the graph represents an average of 50-100 single measurements. These experiments measured the adhesive force, which is only semi-quantitative and needs to be referenced to an internal calibration at the time of measurement. In our case we have chosen to normalise each measurement by the average value recorded in pure water. Unlike other colloid probe measurements, one therefore does not need to calibrate either the spring constant or the radius of the silica tip. This allows one to rapidly screen the different solutions for adhesion, while foregoing some of the finer detail about the forces upon approach of the two surfaces. In all cases studied, no strong repulsion was noted upon approach and so this data has not been shown here.

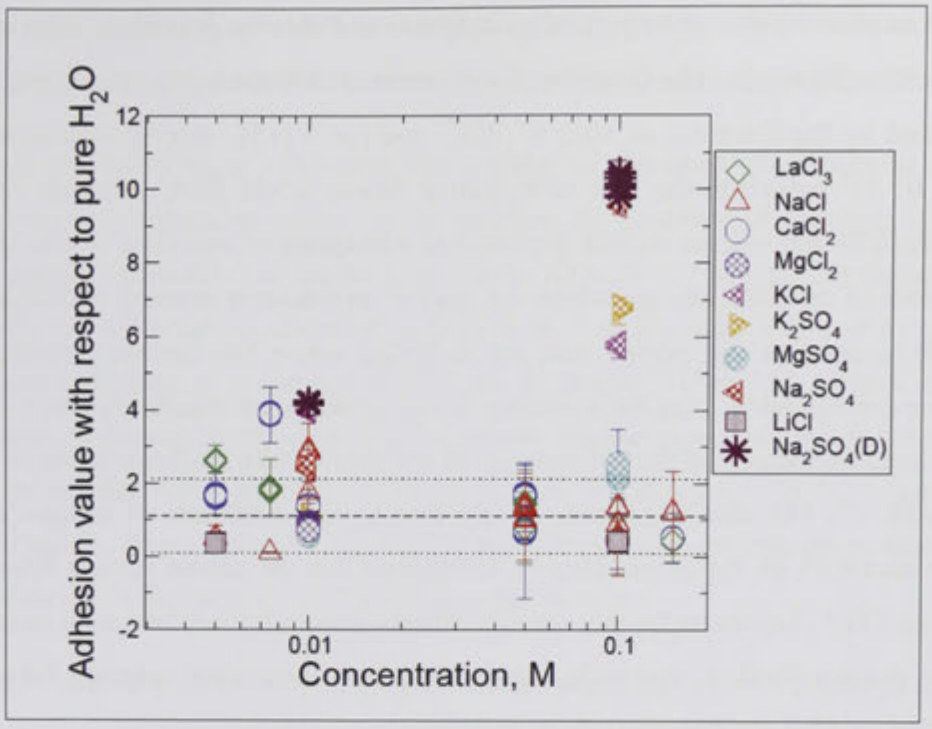

Figure 2.2. *Averaged value of adhesion force between silica and calcite in different brines. All values have been normalised by the average adhesion recorded for pure water. "D" in the legend denotes the one experiment on dolomite. The black dashed line corresponds to pure water values and their standard deviation.*

The fact that no repulsion was seen at any stage of the experiments implies that calcite was at its isoelectric point, which is around the pH of the salt solutions studied (14). This is not unreasonable, given the low surface charging. At no stage in the concentration series does calcite develop a substantial surface change, nor is the van der Waals adhesion noticeable. In addition, no short-range repulsion typical of hydration forces is seen. Only three salts showed any discernible effects at 0.1 M, namely the sulphates of sodium and potassium, and potassium chloride. At 0.005 M, adhesion increases slightly as the valency of the cation increases, this is mainly due to the larger electrostatic attraction of the multivalent cations. As concentration rises further (0.0075 M), lanthanum reacts with CO_3^{2-} and chemisorbs onto the calcite surface, forming very insoluble lanthanite ($La_2(CO_3)_3 \cdot 8H_2O$), thus compensating the surface charge. On the other hand, calcium chloride increased adhesion at this concentration by introducing extra positive charge to the surface. Above 0.01 M, multivalent cations do not have an effect on adhesion between silica and calcite, mainly due to the electrostatic screening of the mineral surface. Monovalent cations start to have more pronounced effect, in particular in combination with a divalent anion like sulphate. For example, at 0.1 M the highest adhesion value for both calcite and dolomite surfaces occurs in the presence of

sodium sulphate, followed by potassium sulphate and then by potassium chloride. This ion-specific effect cannot be described by classical DLVO theory (as the valency effect was tested by the chlorides of Na^+, K^+, Ca^{2+} and La^{3+}) (15), nor by hydration forces (tested by Li^+, which in the case of hydration forces would show strongest repulsion (16)). Specific ion effects include preferential adsorption of one type of ion over and above ions of the same charge, which can lead to increased or decreased charging. It is possible to imagine that certain ions act to bridge across two surfaces, mediating an adhesive configuration. Like the hydration forces, specific ion effects are also very short range. Such an affinity of the sulphate anion towards calcite has been noted in several studies (8; 17; 18), and it has been shown that at concentrations of sodium sulphate greater than 0.01 M, the anion starts to incorporate into the calcite surface structure by replacing CO_3^{2-}. Interestingly, this specific affinity is only for sulphate with monovalent cations, and not divalent, as seen in Figure 2.2, where magnesium sulphate did not have any effect on adhesion between calcite and silica.

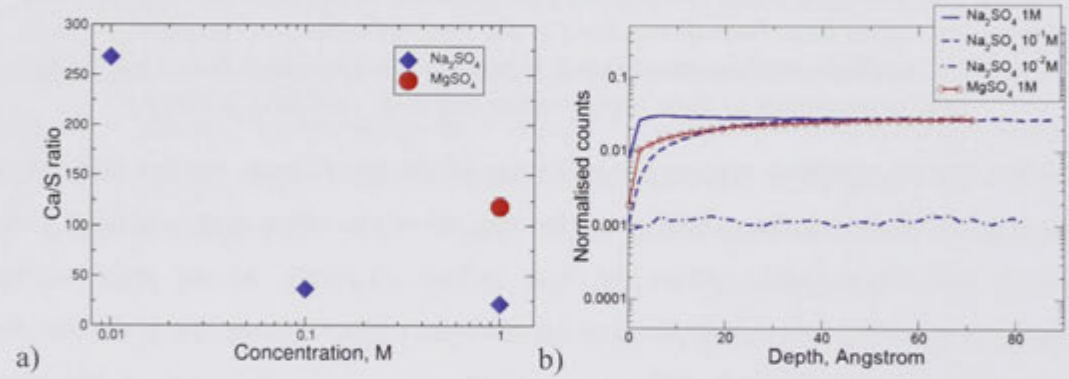

Figure 2.3. *ToF-SIMS results: a) Calcium to sulphur ratio versus concentration of salt, b) Sputter depth profile of the thin film of SO_4^{2-} deposits on calcite plotted as normalised counts of sulphur versus concentration of salt.*

To compliment AFM measurements and test whether sulphate incorporates into the calcite surface and to what depth, a surface elemental analysis was performed with ToF-SIMS. This technique allows one to analyse the concentration of ions as a function of depth by removing secondary ions from atomic monolayers on the surface. The experiments estimated the calcium to sulphur ratio of the calcite piece pre-soaked in salt solution as a function of salt concentration. Calcium and sulphur counts were normalised with respect to pure calcite and averaged. Figure 2.3a shows the results of Ca/S ratio versus salt concentration. This ratio decays (sulphur content increases) in accordance with a power law as the concentration of Na_2SO_4 increases. In particular, a sharp transition occurs from 0.01 M to 0.1 M, in which the 10-fold increase in

concentration results in around 5-fold reduction in Ca/S ratio. Sulphur from Na_2SO_4 incorporates better into the calcite surface than from $MgSO_4$, as seen in Figure 2.3a.

The depth profiles (Figure 2.3b) show that sulphur incorporated into calcite as deep as 80 Å at all concentrations (clean calcite showed no presence of sulphur), with the highest concentration for 1 M Na_2SO_4 and lowest for 0.01 M Na_2SO_4. The highest peak of sulphur concentration is observed at 6.45 Å in 1 M Na_2SO_4, followed by a slight decay and flattening to a plateau around 40 Å. Sulphur from 1M $MgSO_4$ did not accumulate so densely in the outer layer of calcite compared to 1 M Na_2SO_4, though at depths greater than 40 Å the concentrations equalise for all salts, with the exception of 0.01 M Na_2SO_4. This could be explained by faster dissolution of deposits on the calcite surface formed in the presence of $MgSO_4$ than for Na_2SO_4.

Both Mg^{2+} and SO_4^{2-} play important roles in the geochemistry of calcium carbonate-water systems and strongly influence calcite growth and morphology. Studies (19) show that increase in concentration of SO_4^{2-} ions can cause increase in incorporation of Mg atoms into calcite. This is due to the tendency of magnesium to form strong ion pairs with sulphate, an effect similar to chelation, in which SO_4^{2-} lowers the concentration of strongly hydrated Mg^{2+} ions in solution. In case of Na_2SO_4, it seems that sodium does not incorporate into the calcite structure, but only SO_4^{2-} (19; 8), probably forming calcium sulphate at the interface. Incorporation of both SO_4^{2-} and Mg^{2+} may cause more distortions in the calcite crystal than incorporation of only SO_4^{2-}, and consequently may raise the surface free energy and form a compound of higher solubility. This could explain the lower amount of sulphur on calcite in the presence of the divalent cation.

2.2 Case study

2.2.1 Introduction

Although waterflooding has been by far the most widely used oil recovery technique for over eighty years, the displacement mechanisms that determine recovery efficiency are not well understood. Evidence has accumulated over the last fifteen years that recovery efficiency can depend on the salt solution composition of the waterflood (20; 21; 22; 23; 24). Increased recovery is often observed for salinities below about 5000 ppm. Salt solutions below this concentration are referred to as low salinity brines, LSB, and salt solutions of higher salinity as HSB. Laboratory observations of increased recoveries with LSB injection have been supported by field tests (23; 25; 26). Evidence for

improved oil recovery due to specific ions has also been reported (27; 28). Necessary conditions for increased recovery by LSB flooding of sandstones were the presence of connate water, the presence of clay, adsorption of polar components from crude oil (20), and the presence of the crude oil/salt solution interface (28).

Sufficient conditions for increased recovery have not yet been established. Many possibilities have been suggested as to the mechanism(s) of increased recovery; however, many uncertainties remain. An exception to the requirement of clay for increased low salinity recovery was recently reported for Tensleep sandstone from Wyoming (2). This sandstone is eolian and well sorted, but is generally heterogeneous from small to large scales due to the presence and varied distribution of interstitial dolomite and anhydrite. The anhydrite is mainly present as pore filling cement, whereas the dolomite is commonly distributed as small crystals including pore filling aggregates. The crystals are about an order of magnitude smaller in diameter than the quartz sand grains. The Minnelusa formation of Wyoming is also eolian, with comparable depositional history to the Tensleep. The two formations account for one third of Wyoming's current oil production. For the essentially clay-free Tensleep sandstone, it has been suggested that the dolomite crystals play a role in the low salinity recovery mechanism. If the rock is treated with hydrochloric acid to remove the dolomite crystals, oil production no longer responded to change from HSB to LSB injection (2).

2.2.2 Materials and methods

Rocks

A sample of the Tensleep sandstone was taken from the Tensleep formation at the Teapot Dome oilfield in Northern Wyoming, USA. SEM images of fracture surfaces of the sandstone are shown in Figure 2.4. The presence of iron lends itself to colour the dolomite present an orangey-pink hue. The presence of some illite was also noted in the section.

Salt solutions

Two synthetic salt solutions were prepared from MilliQ water and reagent grade chemicals. The compositions of the brines were based on the 38651 ppm Minnelusa reservoir brine and a representative 1316 ppm coalbed methane water with low salt concentration (2); and are detailed in Table 2.2. These two salt solutions will be referred to as the high salinity and low salinity brines (HSB and LSB), respectively.

Table 2.2. *Composition of Minnelusa reservoir brine and coalbed methane water, and their total dissolved solids (TDS).*

Salts	Minnelusa formation water (mg/L) (HSB)	CBM Water (mg/L) (LSB)
NaCl	29,803	915.7
KCl	-	28.7
$CaCl_2$	2,104	191.5
$MgCl_2$	-	180.4
Na_2SO_4	5,903	-
$MgSO_4$	841	-
TDS	38,651	1,316.3

Scanning Electron Microscopy (SEM)

High resolution images of the Tensleep sample were acquired with a Hitachi 4300 SE/N Field Emission SEM (2006). Backscattered images of fracture surfaces and of thin sections were obtained. XRD analysis was performed on the fracture surfaces.

Micro-Computed Tomography (micro-CT)

For the tomographic experiments, 4 mm diameter cylinders of Tensleep core ~10 mm in length were cored from a 4-inch core sample. The tomograms were obtained using the ANU micro-CT facility (29); 2880 projections of 2048^2 pixels were acquired for the tomogram; the pixel size was 2.4 μm. Tomograms were typically acquired using filtered Bremsstrahlung with the X-ray source set to a voltage of 80 kV and current of 100mA. The projections were reconstructed and a raw tomographic image was obtained. Typically, two data sets were obtained. Firstly, the sample was scanned dry, and then vacuum saturated with the HSB and then flushed with the LSB and scanned again.

Mass Spectrometry

Ion analysis of the effluent from the Tensleep sandstone after HSB and LSB flooding was performed by Varian Vista AX CCD Simultaneous ICP-AES (cations) and by Dionex Ion Chromotograph Series 4500i (anions).

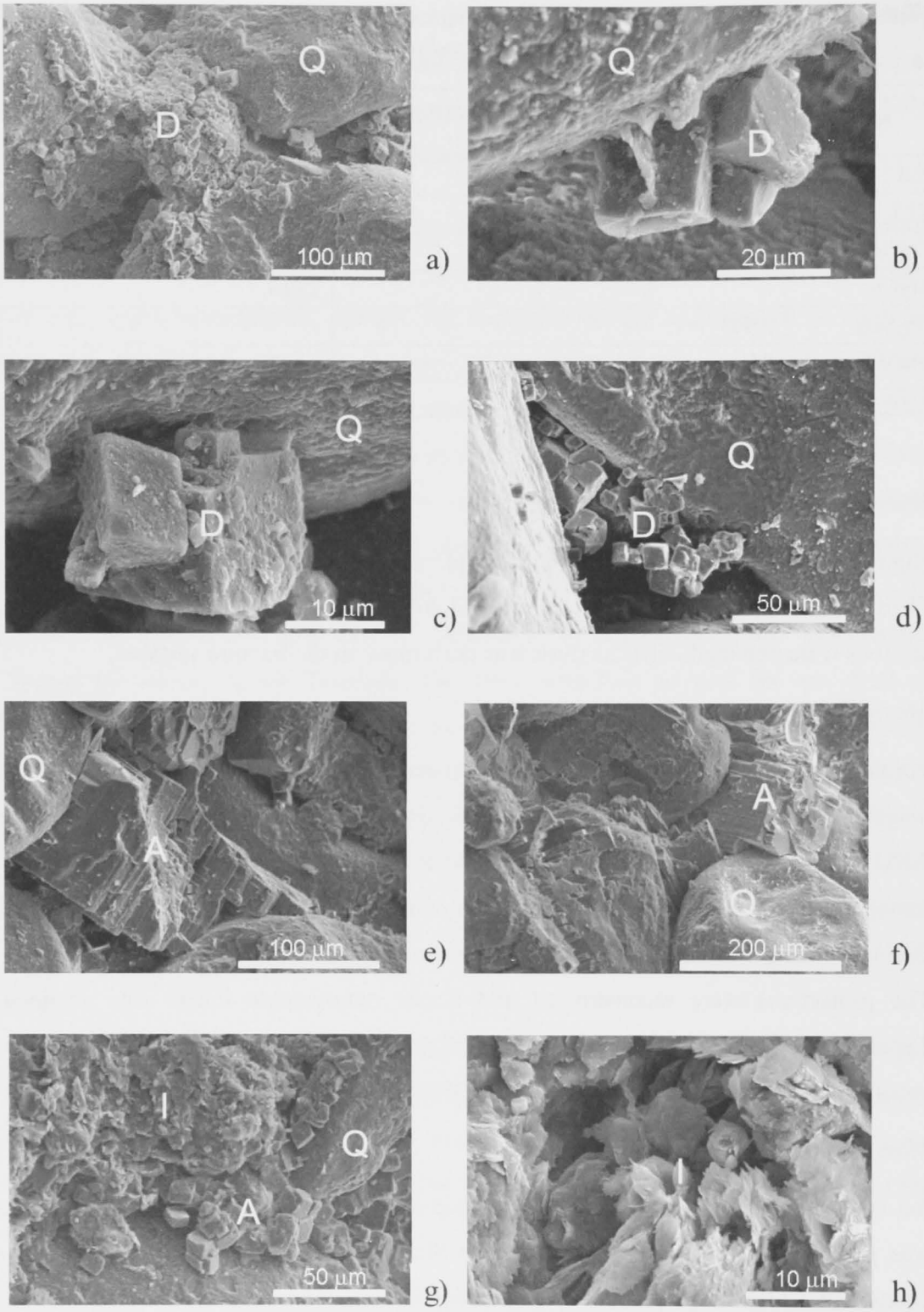

Figure 2.4. *SEM images of Tensleep sandstone: a,d) agglomeration of dolomite (D) particles at grain contacts; b,c) dolomite particles attached to the quartz (Q) surface; e,f) interstitial growth of anhydrite (A); g,h) illite (I) with dolomite.*

2.2.3 Results and discussion

Micro-CT imaging and phase separation

The raw tomographic data set is made up of a 3D array of x-ray attenuation values that are related to the density of the material at each array element. A slice from a tomogram of dry Tensleep sandstone is shown in Figure 2.5 (a,b) at different magnifications. The attenuation histogram for the sample is shown in Figure 2.6. The range of x-ray densities result in three discernible attenuation peaks. These peaks are associated with the pore space (low attenuation), the quartz grains (intermediate) and the dolomite grains and anhydrite cement (high). Dolomite could not easily be distinguished from anhydrite, and so the two are combined. Differentiating the attenuation map into these three distinct phases by simple thresholding is problematic. The presence of features with intermediate attenuation (in particular small dolomite particles) and other features at scales below image resolution (e.g. the presence of weathered/partially dissolved grains) results in poorer identification of the three phases by simple thresholding of attenuation (30). To analyse the tomograms, a multistage phase identification process was used to label each voxel (31). The first stage comprised a filter, which removed noise while preserving significant features, i.e. the boundary regions between the phases. Regions that are clearly pore space, quartz and dolomite/anhydrite phases were defined on the image data. Phase separation in the more ambiguous intensity regions between these phases was then made using the active contours and watershed methods. The resultant histogram with identification of the three phases is shown in Figure 2.6. Segmentation of the images in Figure 2.5 (a-b) is shown in Figure 2.5 (c-d). The image segmentation seems, to the eye, to capture the phase boundaries accurately.

A measure of the quality of the image segmentation was based on optimally aligning higher resolution micrographs, taken by sectioning the actual core scanned, to the original tomogram (32). After completion of all micro-CT imaging scans, a thin section was prepared from the imaged sample and the polished surface of the thin section was imaged at high resolution with BSEM and optical microscopy (Figure 2.7). This procedure allows preparation of high resolution images and also the direct identification of minerals by optical microscopy. By aligning the high resolution 2D BSEM image with the corresponding slice of the 3D micro-CT data, the quality of the 3D image can be assessed. The results shown in Figure 2.7 indicate that the tomographic image provides a reliable representation of the sample and reasonable phase identification.

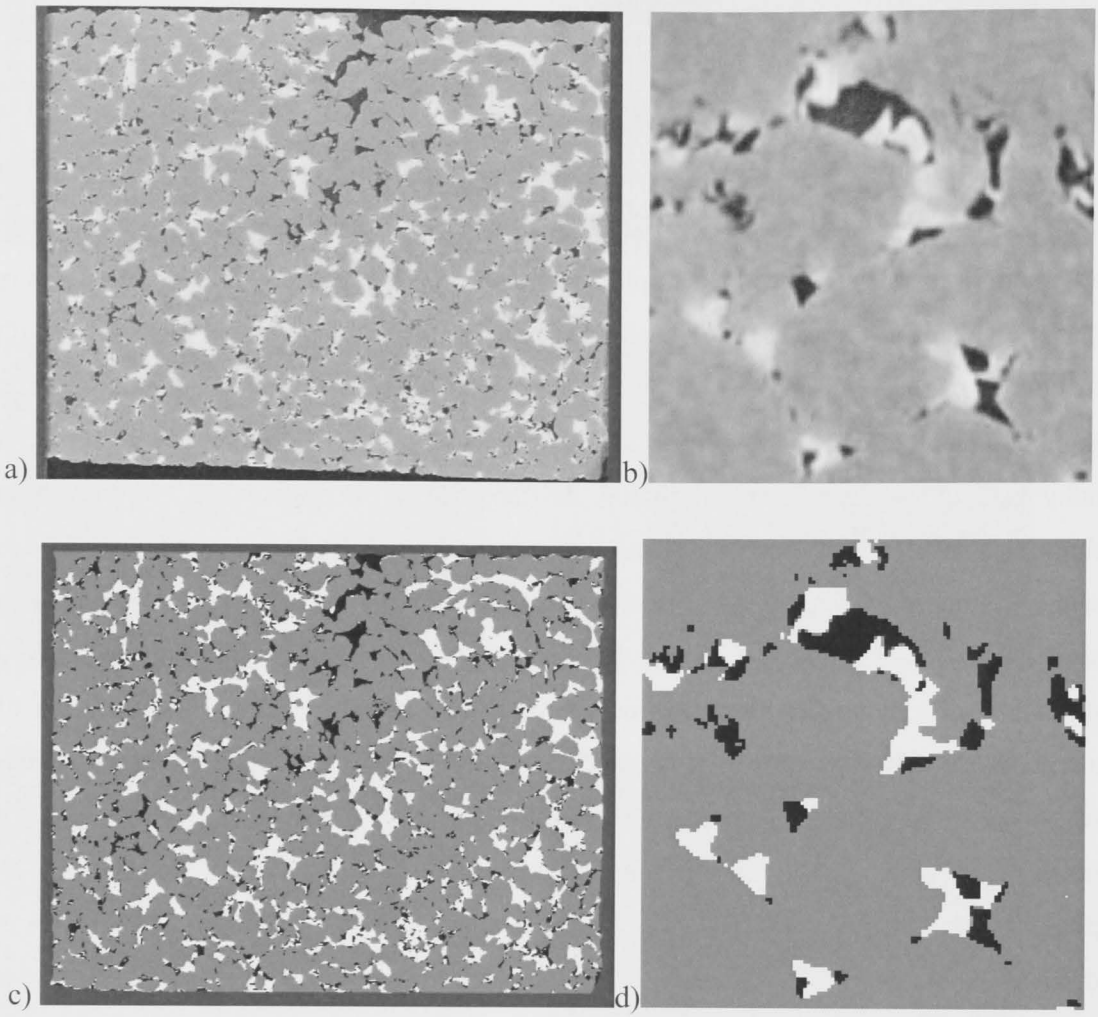

Figure 2.5. *Grey scale attenuation of a slice through Tensleep sandstone at a) full image size (4 mm diameter) and b) zoomed in on a region of 369x408 μm^2. c) and d) show the corresponding three phase segmentation into pore (black), quartz (grey) and dolomite/anhydrite (white) phases of the image.*

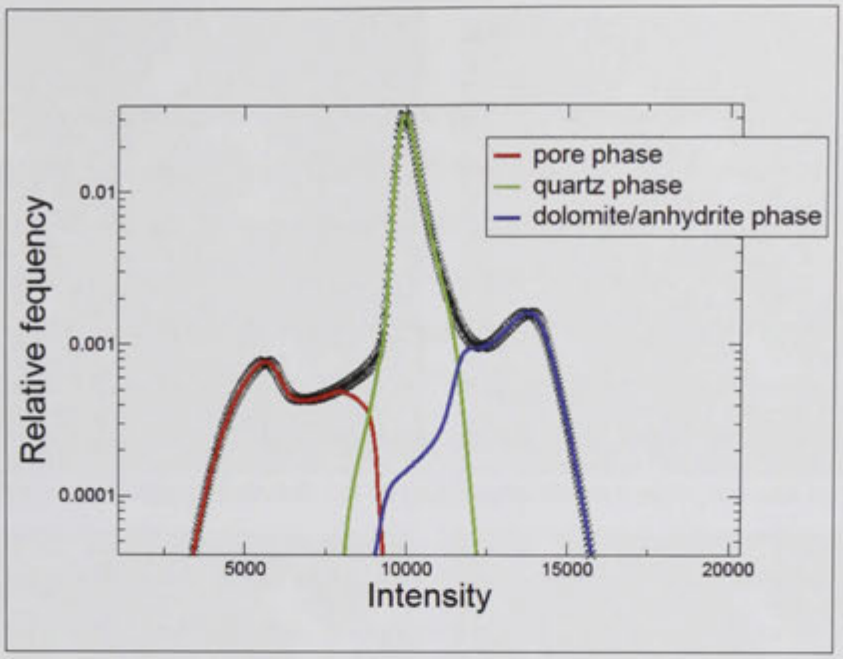

Figure 2.6. *Logarithmic relative frequency versus normalised x-ray attenuation distributions from the dry Tensleep sandstone sample. The black symbols show the overall histogram. The 3 coloured curves shows the resultant histograms of the three phases in the legend.*

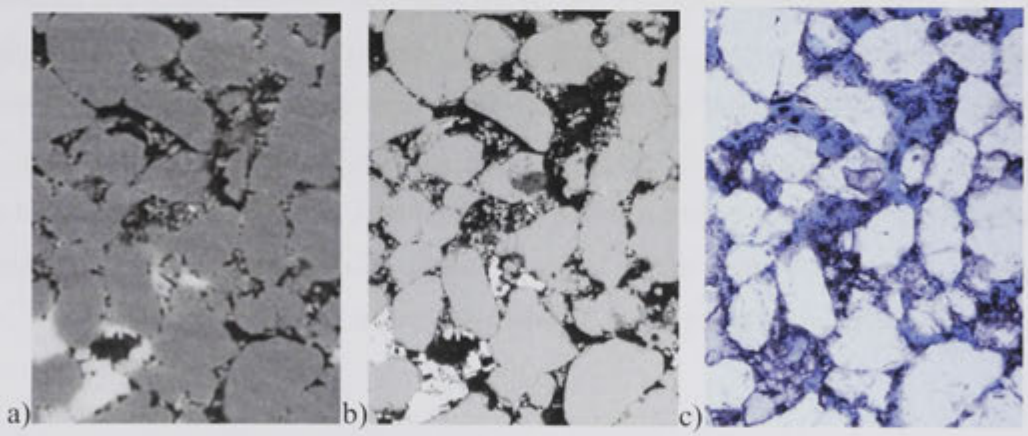

Figure 2.7. *a) Slice of the 3D tomographic image (2.4 μm per voxel) of dry Tensleep sandstone registered to the thin section image from b) BSEM (1.2 μm per pixel) and c) optical microscopy (1.3 μm per pixel). The sample size is 2x1.5 mm^2. In a) the pore space, quartz grains, anhydrite cement (bottom left) and dolomite crystals (pore filling particles) are aligned well with the respective phases in b) and c).*

Micro-CT imaging after LSB flooding

The same core was imaged after flooding with LSB. 3D image registration (32) allows one to superpose, at voxel resolution, the two core images before and after low salinity flooding. This allows direct comparison and quantification of the spatial distribution of the different phases after LSB flooding. There is clear evidence that the dolomite/anhydrite phase redistributes after LSB flooding. Examples of slices through the registered images are shown in Figure 2.8, and Figure 2.9 shows comparisons of 3D visualisations of the image data before and after flooding with LSB. In all cases, movement of the anhydrite cement phase and/or the dolomite particles is apparent.

Movement of dolomite/anhydrite phase after LSB flooding could be attributed to dissolution of anhydrite at the interphase between dolomite and quartz surfaces. The low concentration solution mainly differs from its high salinity counterpart by absence of sulphate salts (Na_2SO_4, $MgSO_4$) and presence of KCl and $MgCl_2$ (Table 2.2). As was discussed in Chapter 2.1.3, sulphate anions, in particular with monovalent cations, have specific affinity for the carbonate surface. At concentrations above 10^{-2} M, the sulphate anion starts to incorporate into the calcite surface structure by replacing CO_3^{2-} (8; 17; 18). The AFM experiments showed the largest adhesion between quartz and carbonate (both calcite and dolomite) in the presence of monovalent sulphate salts (Na_2SO_4, K_2SO_4). These observations can imply that sulphate acts as a bridging agent between dolomite particles and quartz grains at high salinity conditions (HSB). Once the sulphate-free low salinity solution (LSB) was introduced, equilibrium was disturbed and sulphate started to dissolve, which indirectly triggered dolomite/anhydrite particles to move around in the pore space of the Tensleep sandstone.

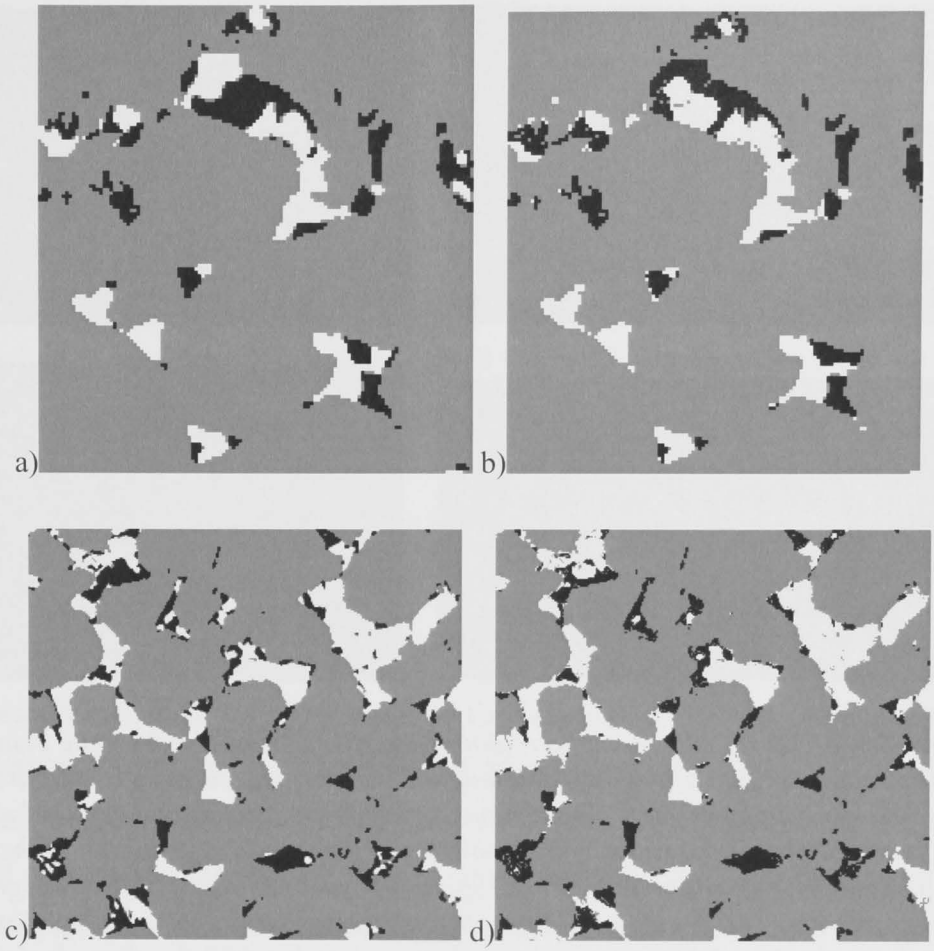

Figure 2.8. *a), c) are slices from the original dry-state tomogram and b), d) are the corresponding registered slices of the same regions after flooding with LSB. The size of the images are 369x408 μm^2 for a,b) and 819x777 μm^2 for c,d). The dissolution and/or redistribution of dolomite particles and/or anhydrite cement is evident from comparison of the two image pairs.*

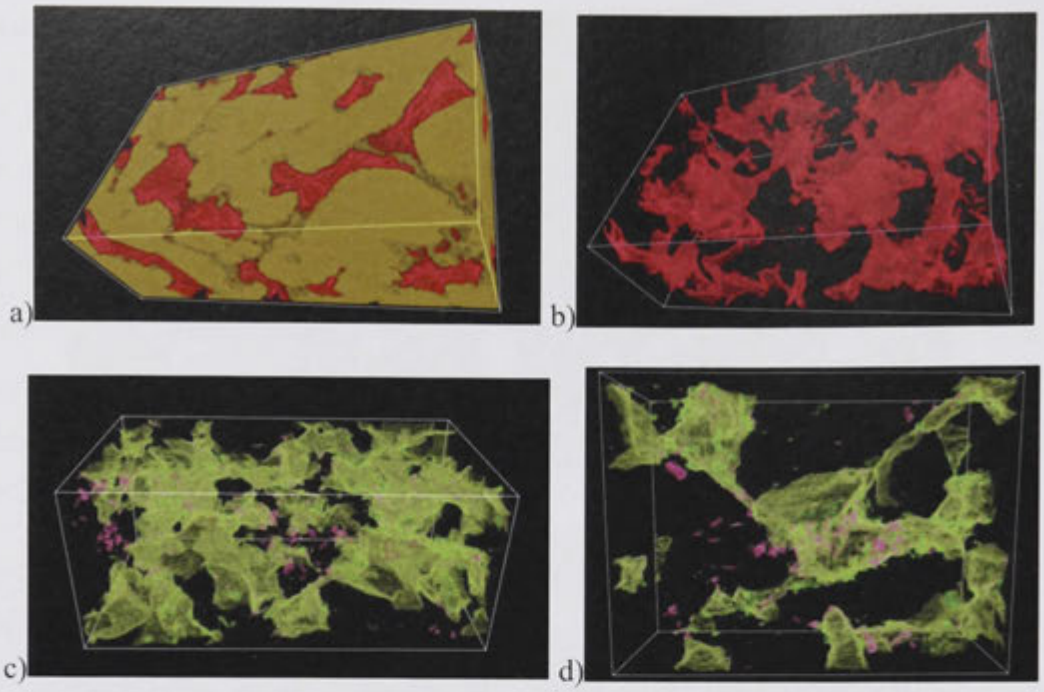

Figure 2.9. *a) 3D visualisation of a region (816x261x228μm^3) in dry-state Tensleep sandstone, showing quartz (yellow), dolomite/anhydrite (red) and pore (transparent). b) shows the dolomite/anhydrite phase in the same volume after digital removal of the quartz phase. c) shows the volume overlay of the spatial distribution of the dolomite/anhydrite phase in the same region (816x417x286μm^3) of the tomogram before and after LSB flooding. The purple and green phases show respectively the spatial distribution of dolomite/anhydrite before and after LSB flooding. d) shows a small inset of c) of volume 483x360x171μm^3.*

Mass spectrometry

The concept of dolomite/anhydrite dissolution and the role of sulphate was further tested by analysing the effluent after flooding with HSB and LSB. The ion analysis of the LSB flooding effluent indicated a significant presence of sulphate, despite its absence from the injection salt solution. This indicates that anhydrite dissolution occurs during the LSB flooding. This analysis of the LSB effluent also showed the presence of Fe; this element, again absent from the salt solution, is found by XRD to be present in the dolomite phase. No Fe was detected after flooding with the HSB or after injection of the LSB with added sulphate. Thus, it was concluded that iron is released from the dolomite only when the concentration of sulphate falls below a critical value, mostly likely related to the solubility product of anhydrite.

2.3 Conclusion

A range of measurements at the pore and molecular scales on Tensleep sandstone have been undertaken to probe more precisely the reasons for the observed improved oil

recovery under low salinity conditions:

Micro-CT imaging of a Tensleep sandstone plug before and after low salinity brine flooding was performed. Pore scale analysis coupled with image registration led to the observation that the dolomite crystals and anhydrite were locally mobilised within the pore space on changing from high to low salinity injection.

The ion analysis of the effluent from LSB flooding of Tensleep sandstone with CBM brine indicated a significant presence of sulphate, despite its absence from the injection brine. This indicates that anhydrite dissolution occurs during the LSB flooding. The ion analysis of the LSB effluent also showed the presence of Fe; this element, again absent from the brine, is found by XRD to be present in the dolomite phase.

AFM was used to probe the adhesion of quartz:calcite surfaces in aqueous electrolytes. The interactions which may play a role in the adhesion of silica to carbonate surfaces were tested. DLVO and hydration forces do not explain the adhesion of silica to carbonate surfaces. Specific ion effects play a role in the interaction. K^+, Ca^{2+} and SO_4^{2-} showed discernible effects, which are consistent with the increased adhesion of dolomite particles under HSB conditions observed in Tensleep sandstone.

This leads to a proposed model for brine/rock interactions in Tensleep sandstone in Figure 2.10. Firstly, and under geological conditions, the dolomite is surface nucleated, the crystallite growing 'keyed-into' the quartz surface. Under HSB conditions this configuration is stable, the balance of ions being sufficient to leave the dolomite at the quartz surface. In the presence of sulphate at HSB conditions, the surface of the dolomite becomes exchanged to some extent by SO_4^{2-}. The higher solubility of this coating, in comparison with the parent dolomite, means that in lowering the ionic strength, the crystallite can lose its close conformal connection with the quartz surface. In addition, the native adhesion seen for HSB in the present of sulphate is also diminished. It is worth noting that the sulphate recharge can be as little as a molecular film. In future work we will investigate the dolomite interface directly with the goal of studying the role of specific ion effects on improved oil recovery in Tensleep sandstone. A longer-term goal will be to undertake micro-CT imaging studies of oil displacement in Tensleep core after HSB flooding and LSB flooding to observe, at the pore scale, the redistribution of residual oil during improved recovery processes.

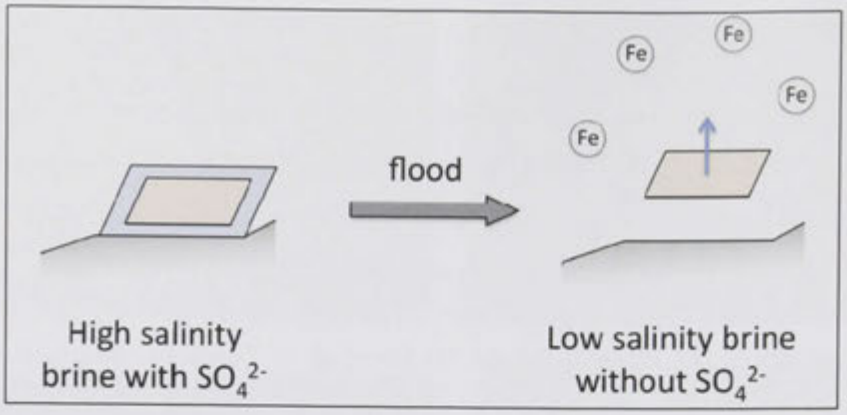

Figure 2.10. *A schematic showing the suggested mechanism for the detachment of the dolomite particles from the quartz surface in going from HSB (with sulphate-enriched layer shown in blue) to LSB (with sulphate absent). The dissolution of the sulphate-enriched surface in LSB (via dissolution of anhydrite and similarly by dissolution of a sulphate rich film) allows the particle to more readily detach, simultaneously releasing iron from the dolomite.*

3 Kaolinite model substrates and wettability

3.1 Introduction

Wettability of clay minerals, in particular kaolinite, and adhesion to them are central to a range of industries and environmental scenarios (33). Kaolinite is a layered aluminosilicate comprising a tetrahedral silica sheet bonded to an octahedral alumina sheet by sharing of oxygen atoms, with successive 1:1 layers held together by hydrogen bonds to form pseudo-hexagonal platy particles. Kaolinite is very abundant in soil, where wettability plays a key role in soil and landscape hydrology (34), contributing to such phenomena as soil water retention, run-off and erosion (35), and the formation of preferential flow pathways in the unsaturated zone (36; 37). Kaolinite is abundant in oil reservoir rocks and strongly affects their wettability state, as is also the case for kaolinite-containing soils and subsurface environments contaminated by oil spills. The wettability state is dictated by the extent to which drainage of the originally water(brine)-filled pores by the accumulating crude oil leads to direct contact of oil with mineral surfaces and adsorption or deposition of oil components there to alter the mineral's local surface chemistry from water-wet towards oil-wet (38). This in turn strongly influences strategies and efficiencies of oil recovery, e.g. by flooding with brine, and similar issues for oil spill remediation. As one example, recent evidence that injection of brines of low salinity can improve oil recovery from sandstone reservoirs suggests that kaolinite, and oil adhesion to it, plays an key role, although the mechanisms are still debated (20; 27; 39). In other environmental applications, kaolinite is used in filters to treat wastewater contaminated with heavy metals and oil (40) and in bioremediation of oil spills (41; 42).

The fractions of crude oil known to most influence wettability are its asphaltenes and resins (43; 44). Asphaltenes are operationally defined as the fraction insoluble in n-alkanes (e.g. n-heptane) but soluble in toluene. They are the heaviest, most polar molecules in oil, comprised of polycondensed aromatic ring sheets bearing alkyl chains and substituted with hetero-atoms (nitrogen, oxygen and sulphur) forming acid and base groups (45; 46). Resins are lower molecular weight analogues, accordingly soluble in n-

alkanes. Asphaltenes in crude oil are thought to occur as polydisperse colloidal aggregates stabilised by resins, in a manner depending on composition, interactions between asphaltenes and with the solvent medium, and thermodynamic conditions (45; 46).

Wetting and spreading of aqueous phases on kaolinite in air have been previously studied by preparation of relatively flat beds of the particles, on which contact angles are measured (47), or intermolecular interactions are measured, e.g. using AFM (48). A variety of dry preparation procedures have been proposed, including pressing of kaolinite powder into disks (49), sprinkling of particles onto double-sided adhesive tape (50), polishing of mineral chunks (51), or gluing of kaolinite platelet aggregates onto a substrate or AFM cantilever (52). Wet preparation procedures involve the coating of an aqueous kaolinite suspension onto a substrate, e.g. glass slide, followed by ambient evaporation to a porous coat layer and oven drying (53; 54; 48; 47).

Measurement of wetting, spreading and adhesion of crude oil on and to kaolinite in scenarios relevant to oil recovery and remediation must deal with the more complex system in which oil contacts the kaolinite substrate in an aqueous environment. This poses a number of experimental challenges. Any re-suspension of kaolinite particles in the surrounding aqueous phase during measurement, particularly for adhesion where a pulling force is applied, will invalidate results. Further, crude oils are very complex liquids which re-equilibrate quite slowly (55), so the duration of their contact with the kaolinite substrate must be sufficient for wettability alteration by adsorption/deposition of asphaltenic components to have become measurable.

Owing to these challenges, wettability alteration and adhesion studies have not previously been performed on kaolinite. Instead, oil-brine contact angle measurements have focused on smooth, impervious model substrates such as quartz (44; 56), mica (57; 58; 59; 60), glass (61; 62; 44; 60) and calcite (38). There are two basic types of measurement, directed at either the tendencies over shorter interaction times (61; 62; 44; 57; 63) or the equilibrium state after long times (62; 44; 57; 58). This chapter considers the former, while Chapter 4 addresses the latter. The contact angle of a captive pendant drop of crude oil on a horizontal flat substrate immersed in the salt solution of interest is first measured after initial growth of the drop (causing the water to recede, thus referred to as the receding angle). After the short period in contact, the oil drop is retracted (causing the water to advance) and the contact angle is re-measured (now called the

advancing angle). Alternatively, using the Wilhelmy plate technique, the vertical model substrate is moved up and down through the oil-brine interface (44; 56). In either case, the difference from receding to advancing conditions is termed the contact angle hysteresis, and thus gives a measure of the wettability alteration and adhesion developed. In many studies, the hysteresis is simply classified as either high (i.e. oil remains on the substrate after retraction) or low (clean removal), reflecting whether or not adhesion is manifested at these early stages (61; 62; 44; 57).

These contact angle studies have contributed enormously to current understanding of the intermolecular mechanisms by which wettability alteration and adhesion occur through thinning and rupture of the water film between oil and mineral substrate, and subsequent interfacial bonding of these two contacting phases. This behaviour is strongly dependent on the salts present in the aqueous phase. For simple 1:1 electrolytes, the majority of crude oils tested have displayed decreasing adhesion to silicate substrates with increase in NaCl salinity and/or pH (38; 64; 44; 61; 62; 58; 59; 65). This is a consequence of the pronounced acid-base character of the asphaltenes and resins at the oil-water interface. They exhibit protonated base groups at low pH and deprotonated acid groups at higher pH, which respectively attract and repel the predominantly negatively charged water-silicate interface. These trends are qualitatively reasonably consistent with expectations from Derjaguin-Landau-Verwey-Overbeek (DLVO) theory, in which the interfacial interactions are taken as the sum of van der Waals attractive forces and electrical double layer forces. The latter electrostatic forces are highly sensitive to the salts present. Quantitative comparison of experiments to DLVO theory, using zeta potential measurements of the two interfaces, and incorporating charge regulation (66; 64; 61), served to further pinpoint the agreement and the discrepancies. In the presence of divalent cations in the aqueous phase, the experimental results are more variable and system dependent, and the scope for non-DLVO interactions due to ion-specific and ion-binding effects is increased (62; 57).

Kaolinite can give rise to even more complex intermolecular mechanisms for adhesion (27) than the above-mentioned silicate substrates, due to its cation exchange capacity and differences between platelet faces and edges. Thus, there is a need to extend the contact angle studies of kaolinite substrates exposed to an aqueous phase in air, and smooth, impervious mineral substrates exposed to oil in brine, to begin to address these more complex oil-brine-kaolinite systems. Chapter 3 describes the development of smooth, thin, porous kaolinite coats, which uniformly cover their glass substrate and

remain unperturbed in brines and in contact with oil. These are used to investigate contact angle hysteresis of crude oil drops after relatively short exposure times. A matrix of sodium chloride brines is considered first, followed by mixtures with calcium chloride. The adsorption and deposition of crude oil components on kaolinite after longer aging of these same systems is addressed in Chapter 4.

3.2 Materials and methods

3.2.1 Preparation of kaolinite substrates

Well-crystallised kaolinite KGa-1b (Washington County, Georgia; Clay Minerals Society Source Clay Repository) comprises 96% kaolinite and trace dickite, 3% anatase and 1% crandallite plus mica and/or illite, and has cation exchange capacity 3.0 meq/100g and BET surface area 11.7 m^2/g (67; 68; 69). Elemental analysis by energy-dispersive x-ray spectroscopy is presented in Table 3.1.

Table 3.1. *Atomic composition of kaolinite KGa-1b, as determined by energy-dispersive x-ray spectroscopy. A dried cake of kaolinite was carbon coated and analysed using Oxford Instruments ISIS on a JEOL 6400 scanning electron microscopy operated at 15 kV and 1 nA. The titanium content is consistent with the presence of anatase as the primary impurity (67).*

Element	O	Al	Si	Ti	Na	Fe
Atomic %	63.69	17.84	17.81	0.54	0.06	0.06

No further cleaning of the kaolinite was performed. An aqueous suspension was prepared from 10 g kaolinite in 150 g deionised water from a Millipore Milli-Q reverse osmosis system (as used throughout this thesis, unless otherwise specified), with rapid magnetic stirring followed by sonication for 10 min. The pH was adjusted to 9.8 using NaOH and maintained so in all subsequent steps. The suspension was centrifuged at 160 g for 3 min., after which the suspended upper phase was decanted (rejecting the sediment), then rapidly stirred and sonicated for 10 min. This process of centrifugation, decanting, stirring, sonication and pH adjustment was repeated at the centrifugal forces of 640 and 1000 g, for 3 min., and finally at 1000 g for 5 min. The resulting dilute suspension of fine kaolinite was heated at 85 °C under rapid stirring until its concentration reached 7 wt%. Approximately 0.05 g of suspension was pipetted as several drops onto a pre-cleaned microscope glass slide (76x26 mm^2), and thinly spread

over the majority of its area. Immediately after, a heat gun (T ~120 °C) was swept in one direction over the wet coat to rapidly immobilise the particles. After drying, each coated slide was flushed under tap water, and then dried.

3.2.2 Salt solutions, crude oil and organic solvents

A total of 25 aqueous salt solutions were prepared from analytical grade NaCl and $CaCl_2$, and were degassed under vacuum for 15 min. prior to any pH adjustment. All solutions were prepared at their unadjusted natural pH, in the range 5.5-6.1. Solutions without $CaCl_2$ were also prepared in acidic (pH 4±0.2) and alkaline (pH 9±0.2) states, by addition of HCl and NaOH. The oil is an asphaltic crude oil from the Minnelusa formation (Gibbs Field, Wyoming). It has density 0.9062 gcm^{-3}, viscosity 77.2 mPa.s, n-C_7 asphaltene content 9.0 wt%, and acid and base numbers 0.17 and 2.29 mg KOH/g oil, all at room temperature (70). The crude oil was filtered and centrifuged before use. Solvents used were decalin (decahydronaphthalene, 98%, Sigma Aldrich) and n-heptane (99%, Riedel-de Haen).

Zeta potential of the fine kaolinite suspension and the crude oil were separately determined in each salt solution using a Zetasizer Nano-ZS (Malvern Instruments), based on standard preparation procedures (71; 64). Results are plotted in Figures 3.1 and 3.2 and summarised in Table 3.2.

Table 3.2. *Matrix of 25 salt solutions at pH 4, natural (pH 5.5-6.1, denoted n) and 9, and the corresponding statistics of zeta potential of the kaolinite suspension and crude oil emulsion, receding and advancing crude oil-brine-kaolinite contact angles, and their difference (hysteresis).*

pH	[NaCl], M	[$CaCl_2$], M	ζ kaolinite, mV	ζ crude oil, mV	Reced., degrees	Advanc., degrees	Hysteresis, degrees
n	0	0	-23.7 ± 0.3	-66.6 ± 1.6	39 ± 4	74 ± 9	35 ± 13
n	0.01	0	-18.5 ± 0.7	-51.2 ± 2.0	35 ± 4	72 ± 21	36 ± 24
n	0.1	0	-18.1 ± 0.8	-17.1 ± 0.3	37 ± 1	62 ± 6	24 ± 6
n	1	0	-11.1 ± 1.9	-12.5 ± 1.4	44 ± 6	53 ± 5	9 ± 11
n	0	0.001	-12.0 ± 0.9	-44.3 ± 0.8	30 ± 2	87 ± 25	57 ± 23
n	0	0.01	-7.5 ± 0.2	-27.5 ± 1.2	30 ± 2	90 ± 5	60 ± 3
n	0.01	0.01	-6.8 ± 0.4	-13.9 ± 0.6	32 ± 4	52 ± 5	20 ± 7
n	0.1	0.01	-11.9 ± 0.4	-16.3 ± 1.5	32 ± 3	41 ± 0	8 ± 3
n	1	0.01	-10.2 ± 0.9	-12.9 ± 1.5	35 ± 4	36 ± 3	2 ± 4
n	0	0.1	0.9 ± 3.0	-7.8 ± 3.1	37 ± 4	50 ± 5	13 ± 10
n	0.01	0.1	-2.6 ± 0.1	-7.6 ± 0.4	37 ± 3	46 ± 9	9 ± 12
n	0.1	0.1	-3.4 ± 0.9	-7.6 ± 0.2	40 ± 2	57 ± 13	17 ± 15
n	1	0.1	-6.2 ± 0.5	-9.6 ± 1.3	39 ± 4	40 ± 3	1 ± 4
n	0	1	2.5 ± 0.8	0.1 ± 1.4	36 ± 0	47 ± 1	11 ± 1
n	0.01	1	1.6 ± 1.0	-2.1 ± 1.1	35 ± 5	51 ± 4	16 ± 9
n	0.1	1	1.5 ± 1.4	1.6 ± 0.5	28 ± 2	30 ± 1	2 ± 2
n	1	1	1.3 ± 0.5	1.6 ± 0.9	40 ± 1	49 ± 4	9 ± 5
4	0	0	-15.8 ± 0.8	21.6 ± 1.5	33 ± 3	121 ± 5	88 ± 3
4	0.01	0	-16.7 ± 1.1	-7.1 ± 0.8	44 ± 16	110 ± 8	66 ± 17
4	0.1	0	-14.5 ± 0.9	-5.7 ± 0.5	43 ± 6	89 ± 29	46 ± 23
4	1	0	-5.1 ± 0.2	-9.8 ± 1.1	38 ± 1	50 ± 7	13 ± 8
9	0	0	-54.6 ± 0.9	-127.0 ± 5.3	32 ± 4	44 ± 7	12 ± 3
9	0.01	0	-47.6 ± 0.8	-78.9 ± 1.0	30 ± 2	62 ± 11	32 ± 8
9	0.1	0	-39.9 ± 2.0	-24.4 ± 0.5	36 ± 4	64 ± 6	28 ± 8
9	1	0	-15.1 ± 1.0	-16.0 ± 0.6	23 ± 2	30 ± 6	7 ± 8

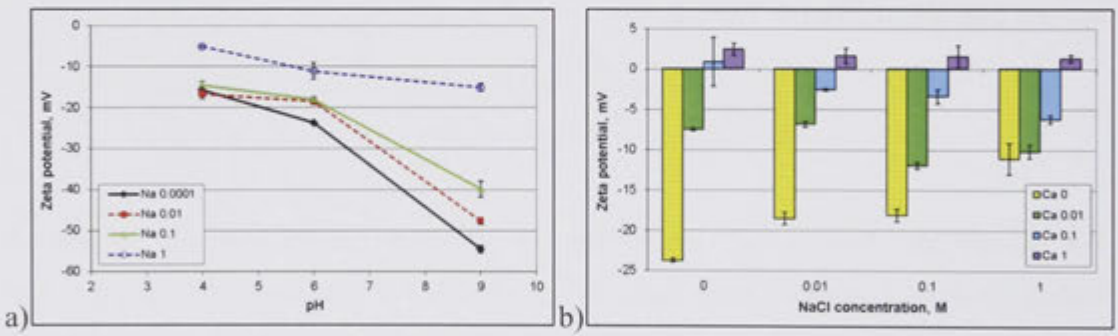

Figure 3.1. *Zeta potential of kaolinite in aqueous suspensions of a) sodium chloride solutions of the four given molarities at the three suspension pH values of 4, 6 (close to the natural pH) and 9, and b) solutions of sodium and/or calcium chloride (each at the four given molarities) at their natural suspension pH, in the range 5.5-6.1. The same suspension of fine kaolinite in water as used to coat the glass slides was diluted to 0.022 wt% using the same stock salt solutions and pH adjustment procedures as for the contact angle brines, with 2 h. equilibration prior to zeta potential analysis. The zeta potential statistics are from 3 measurements, each comprising 10-100 runs, with electrophoretic mobility of the particles converted to zeta potential using the Smoluchowski equation.*

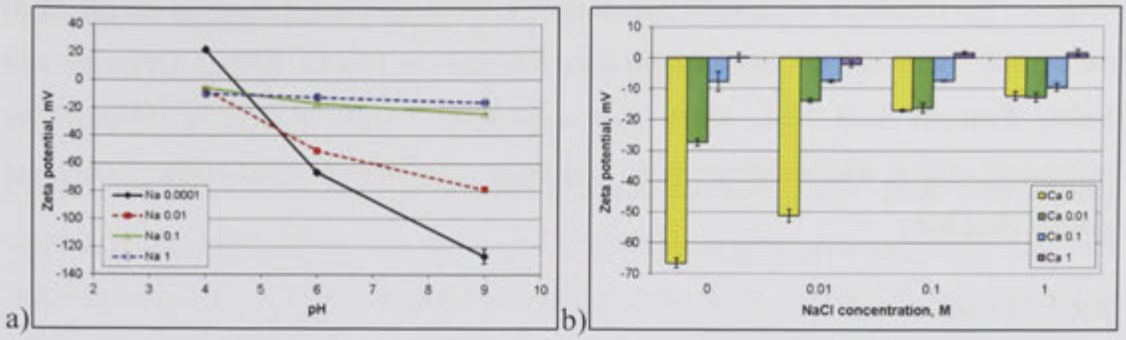

Figure 3.2. *Zeta potential of Minnelusa crude oil emulsified in aqueous suspensions of a) sodium chloride solutions of the four given molarities at the three solution pH values of 4, 6 (close to the natural pH) and 9, and b) solutions of sodium and/or calcium chloride (each at the four given molarities) at their natural solution pH, in the range 5.5-6.1. In each of these brines, prepared using the same salt solutions and pH adjustment procedures as for contact angle, 1 wt% oil was emulsified by sonication for 5 min., then diluted to 0.2 wt% with the same brine and again sonicated for 5 min., and equilibrated for 2 h. prior to zeta potential analysis. Zeta potential statistics are from 3 measurements, each comprising 10-100 runs, with electrophoretic mobility of the particles converted to zeta potential using the Smoluchowski equation*

3.2.3 Microscopy of substrates

FESEM

Kaolinite substrates, lightly sputter coated with platinum (and never reused), were imaged with a Field Emission Scanning Electron Microscopy (FESEM, Zeiss UltraPlus Analytical) in secondary electron mode at 1 kV.

AFM

A Nanoscope III (Digital Instruments) with high sensitivity Super A scanner (maximum scanning area 1.3x1.3 μm^2) was used in tapping mode at 0.89 Hz. The cantilever (Tap300Al, BudgetSensors) had resonant frequency 300 kHz and force constant 40 N/m. AFM images were not processed with any noise reduction filter.

Profilometry

To obtain height maps over much larger areas, a white-light profilometer (Wyko NT9000, Veeco) was operated with 20x microscope objective, 2.0x zoom and numerical aperture of 0.4. Substrate pieces were mapped over 157x118 μm^2 areas, at 0.25 μm/pixel resolution, using vertical scanning interferometry, averaging 10 frames to reconstruct each map. In vertical scanning interferometry (VSI), an internal translator scans vertically during the measurement as the camera periodically records frames. As each point on the surface comes into focus, the modulation on that point reaches a maximum, and then tapers off as the translator passes through focus. By recording the

height of the translator at maximum modulation, the system can determine the height of each pixel. The maximum scan length for a VSI scan is 10 mm. System Overview and Safety Features 1-13 VSI, which uses a broadband light source, is effective for measuring objects with rough surfaces, and those with adjacent pixel-height differences greater than $\lambda/4$.

3.2.4 Contact angle

Captive pendant drop measurements of receding and advancing angle at the crude oil/brine/kaolinite contact (Figure 3.3) were performed at 23-24 °C with a contact angle goniometer (KSV Instruments), using a rectangular prism fluid cell (Hellma OG). A piece of kaolinite-coated glass, ~10x10 mm^2, was mounted on a chuck, immersed in the salt solution-filled fluid cell for 1 h. to equilibrate, and affixed to the fluid cell lid with coated side facing down. A Minnelusa crude oil drop was pumped out upwards at a rate of 0.8 µl/s from the stainless steel hooked syringe (Hamilton; outer and inner diameter 0.65 and 0.31 mm), and left for 10 min. at the tip to equilibrate with the aqueous phase. The drop was contacted with the kaolinite layer and grown slightly more (to ~4 µl), directly after which the drop profile in this water-receded state was imaged. Instrument software fits this profile to the Young-Laplace equation to determine the slope at the contact line, with contact angle taken through the water. The drop was left for 30 min. to give oil the opportunity to partially adhere to kaolinite, then retracted at the same rate for the water-advancing contact angle to be similarly measured. The procedure was duplicated for a second drop on a clean area of the piece. Averages and standard deviations are summarised in Table 3.2 and discussed further in Chapter 3.3.2.

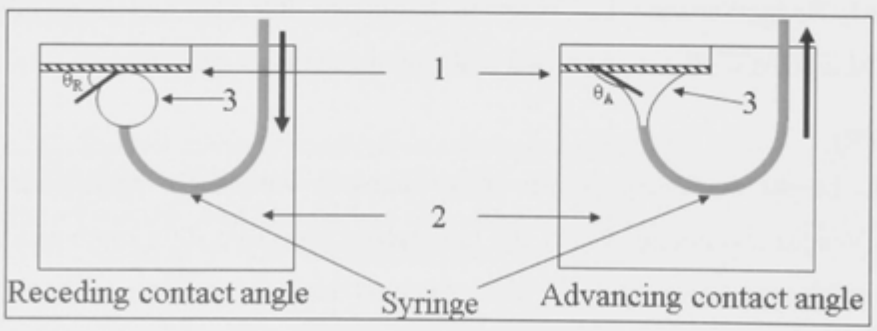

Figure 3.3. *Schematic of measurement of receding (at left, θ_R) and advancing (at right, θ_A) contact angles after oil drop growth and subsequent retraction: 1 – kaolinite-coated substrate, 2 – aqueous solution of interest, 3 – Minnelusa crude oil. A similar contact angle procedure is used in Chapter 4, but with the following differences: 1 - aqueous/oil-aged kaolinite-coated substrate, 2 – pure water, 3 – decane.*

3.3 Results and discussion

3.3.1 Analysis of kaolinite substrates

Figures 3.4 and 3.5 display representative high-resolution images, from FESEM and tapping mode AFM, of the top surface of a kaolinite-coated glass substrate. The vast majority of particles possess a platy morphology; the very occasional, more isotropic particles (e.g. near the bottom of Figure 3.4a) presumably correspond to the anatase or crandallite. Kaolinite particles are present as single plates and stacks of several of these, which remain hydrogen-bonded after sonication. From measuring 250 particles in FESEM images, their broadest dimension has a number average of 280 nm, with standard deviation 150 nm, equivalent to a volume average of 320 nm. In many stacks, larger plates are overlain with smaller plate fragments, so what might be regarded as a large face in reality bears a number of edge steps. Although particle orientation is predominantly parallel to the substrate, many are tilted (most apparent from Figures 3.4b and 3.5a), and some are standing vertically to present only their edge. As kaolinite is a non-swelling clay incapable of forming a sealed barrier, all coats possess some porosity. The coats here typically exhibit pore throat sizes less than 100 nm.

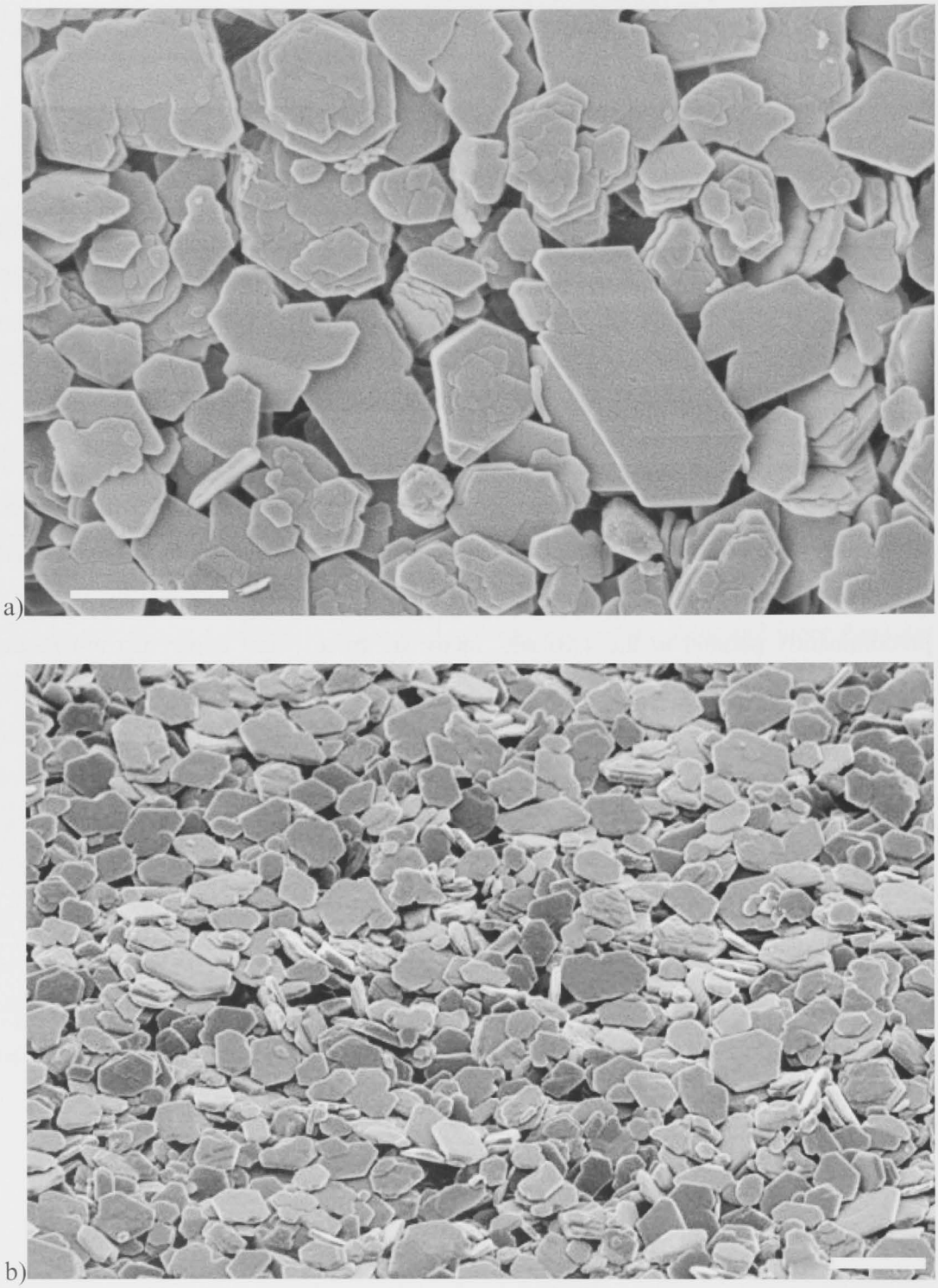

Figure 3.4. *High-resolution FESEM images of the kaolinite coat viewed a) from above and b) tilted 45^{o} downwards from bottom to top edges. Scale bars are 500 nm.*

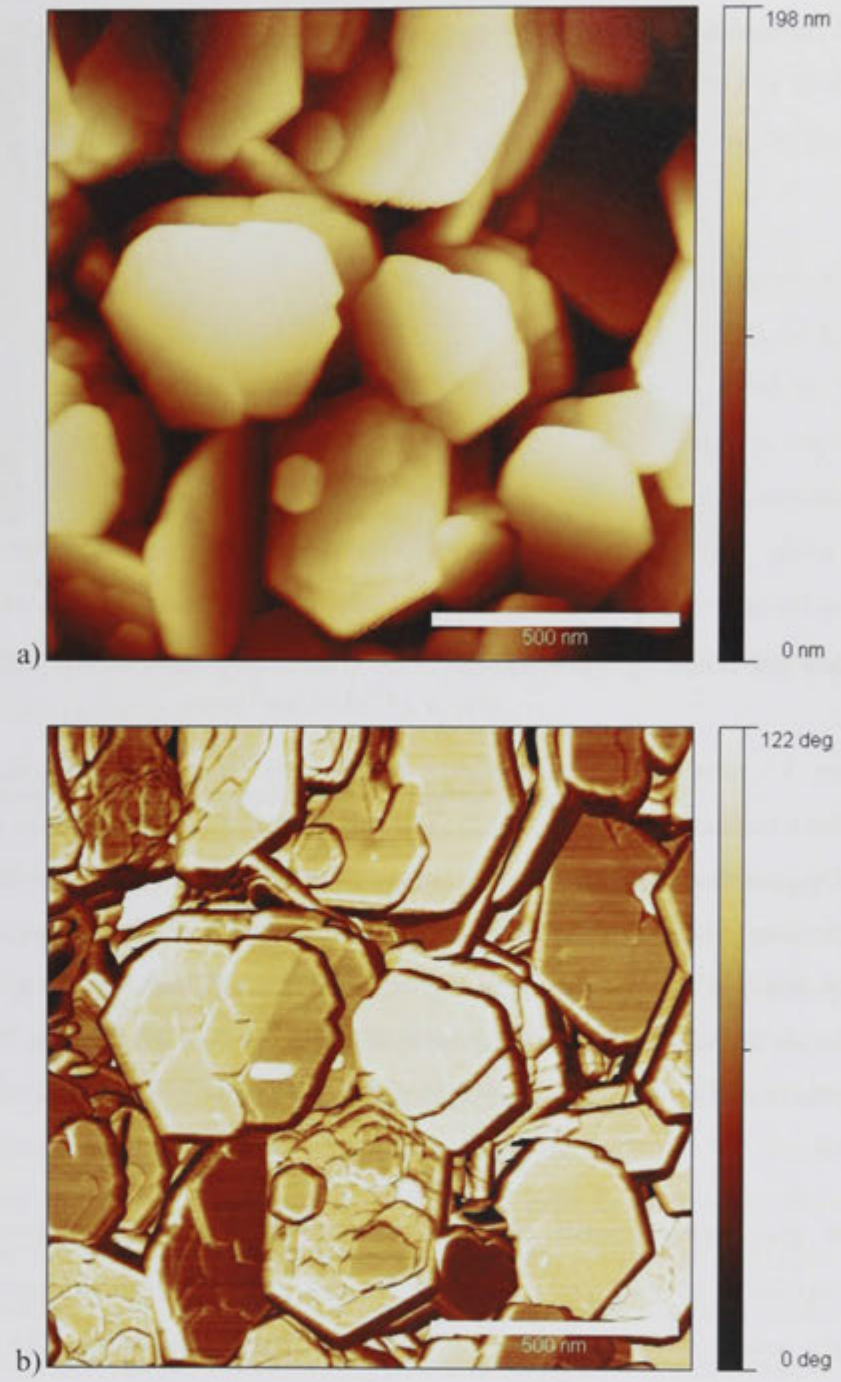

Figure 3.5. *AFM tapping mode images of the kaolinite coat in a) height mode, and b) phase mode, with scale bar 500 nm in both.*

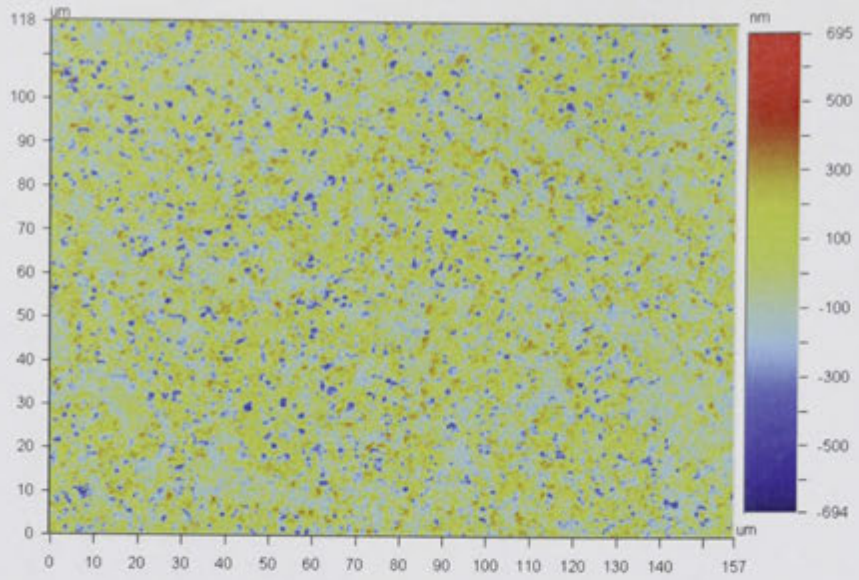

Figure 3.6. *White-light profilometry map of local height (in nm) of a kaolinite substrate over a 157x118 μm^2 area.*

Figure 3.6 provides a representative height map from optical profilometry. Samples exhibit a random speckling of somewhat higher and lower subregions, corresponding to locally greater and lesser coat thickness. Overall surface roughness derives from these longer-range variations and finer-scale features of individual particles and their packing. Three areas of the dimensions in Figure 3.6 were analysed on each of four slide pieces to extract the arithmetic-mean absolute roughness Ra of all features from pixel size to the area size. These 12 values gave an average Ra of 137 nm, with standard deviation of 14 nm.

From gravimetric measurements, the average wet layer thickness is ~40 µm, corresponding to just over 1 µm for the dry coat. FESEM and optical profilometry images near a coat edge support this estimate. Analogous methods in the literature for deposition and evaporation of aqueous kaolinite suspensions to cover smooth substrates produce coats of about 20 µm thickness (53; 54; 47). Our approach attains much lower thickness without sacrificing uniform coverage by combining a high quality suspension and rapid immobilisation post-application. The repeated size fractionation, plus sonication and somewhat higher pH to render all kaolinite faces and edges strongly anionic, yields a very stable, fine suspension. This facilitates metering of a thin wet layer over the glass, and the comparatively high solids content and unidirectional drying at elevated temperature serve to quickly lock-in the structure. This minimises non-uniformities from convective transport towards more rapidly evaporating zones

(producing stick-slip bands of high-low deposition) or premature immobilisation in the vicinity of larger particles and aggregates (rupturing the wet film) (72). The thin, dry coats thus serve to maximise smoothness and particle stability to aid in probing the true oil-kaolinite adhesion via contact angle measurements.

Our coats are naturally much thicker than the incomplete scattering of kaolinite particles on smooth glass and alumina substrates used by Gupta and Miller (48) to favour outwards exposure of the silica and alumina faces, respectively, for AFM force measurement. Even for multilayered coats of kaolinite, it might generally be expected that, at the coat bottom, the less anionic, alumina face preferentially orients towards the more anionic glass substrate, and at the coat top, the more hydrophobic silica face orients towards air. However, in our case the high pH and high solids content of the suspension, coupled with its rapid immobilisation, probably lead to a mixture of the two face types at the coat surface.

3.3.2 Contact angle of kaolinite-crude oil in aqueous solution

If the aqueous thin film between oil and substrate does not rupture, oil contacts the chemically homogeneous, rough surface of the aqueous-filled and -sheathed kaolinite coat, and a Wenzel-type wetting situation pertains. If local rupture and adsorption occurs, so that oil contacts the chemically heterogeneous, rough surface of oil-deposited kaolinite outer surfaces interspersed with residual bulk brine menisci between particles, a Cassie-type model pertains. Both situations, and intermediates to these, are encountered in the results below. Examples of low and high hysteresis are shown in Figure 3.7. In addition to any wettability alteration occurring, substrate topography also contributes to hysteresis, although usually comparatively little for roughness below 100 nm (73). We observe no stick-slip behaviour on drop growth, in line with other studies (54), and for salt solutions allowing little or no oil-kaolinite adhesion; the measured angle hysteresis is often close to zero. Thus, roughness does not appear to contribute significantly to the results. This is partly due to the fact that the porous coat is filled by, and completely or partially lined by, incompressible dense aqueous phase (not air, as for most contact angle experiments), which also has the effect of sealing pores and sheathing tightly curved local geometries, reducing the effective roughness from its value measured in air.

It should also be noted that no kaolinite particle removal during drop growth or more

pertinently, during retraction, was observed, as evidenced by FESEM images of identical locations on the coat before and after the contact angle experiment (Figure 3.8, for the sample with largest hysteresis in Table 3.2). Moreover, as shown in Figure 3.9 the contact angle hysteresis bears no overall correlation to the roughness of the individual kaolinite piece, determined after the contact angle experiment, but equally applicable to the "before" state due to the particle immobilisation. Thus, roughness does not contribute significantly, and hysteresis values directly reflect the intermolecular adhesion of oil to kaolinite. Owing to the increased difficulty of measuring contact angles in the presence of two liquids, especially crude oil requiring equilibration at each step, the number of duplicates for each oil-brine pair was usually only two. The graphs on the following pages plot average values, with standard deviations as error bars.

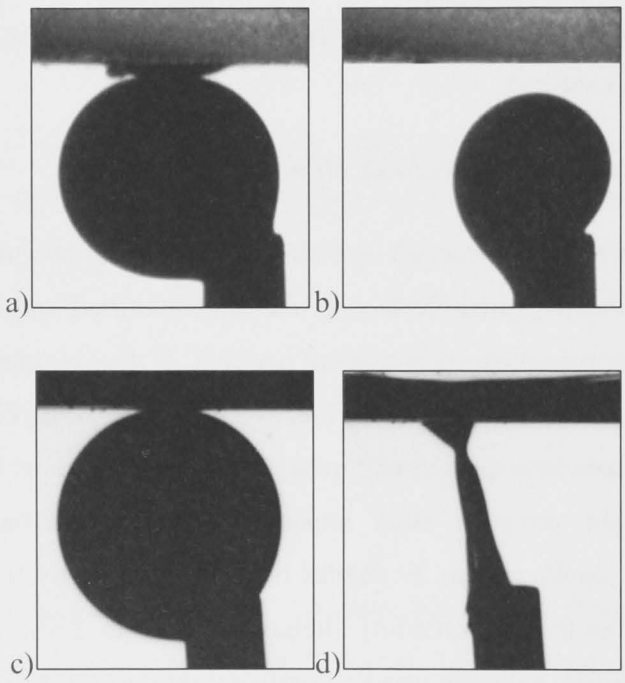

Figure 3.7. *Images during contact angle measurement of an oil drop on kaolinite in NaCl solutions of 1 M at pH 9 (after a) growth, b) retraction) and 0.005 M at pH 4 (after c) growth, d) retraction), giving average angle hysteresis of 7° (non-adhesive) and 88° (adhesive), respectively.*

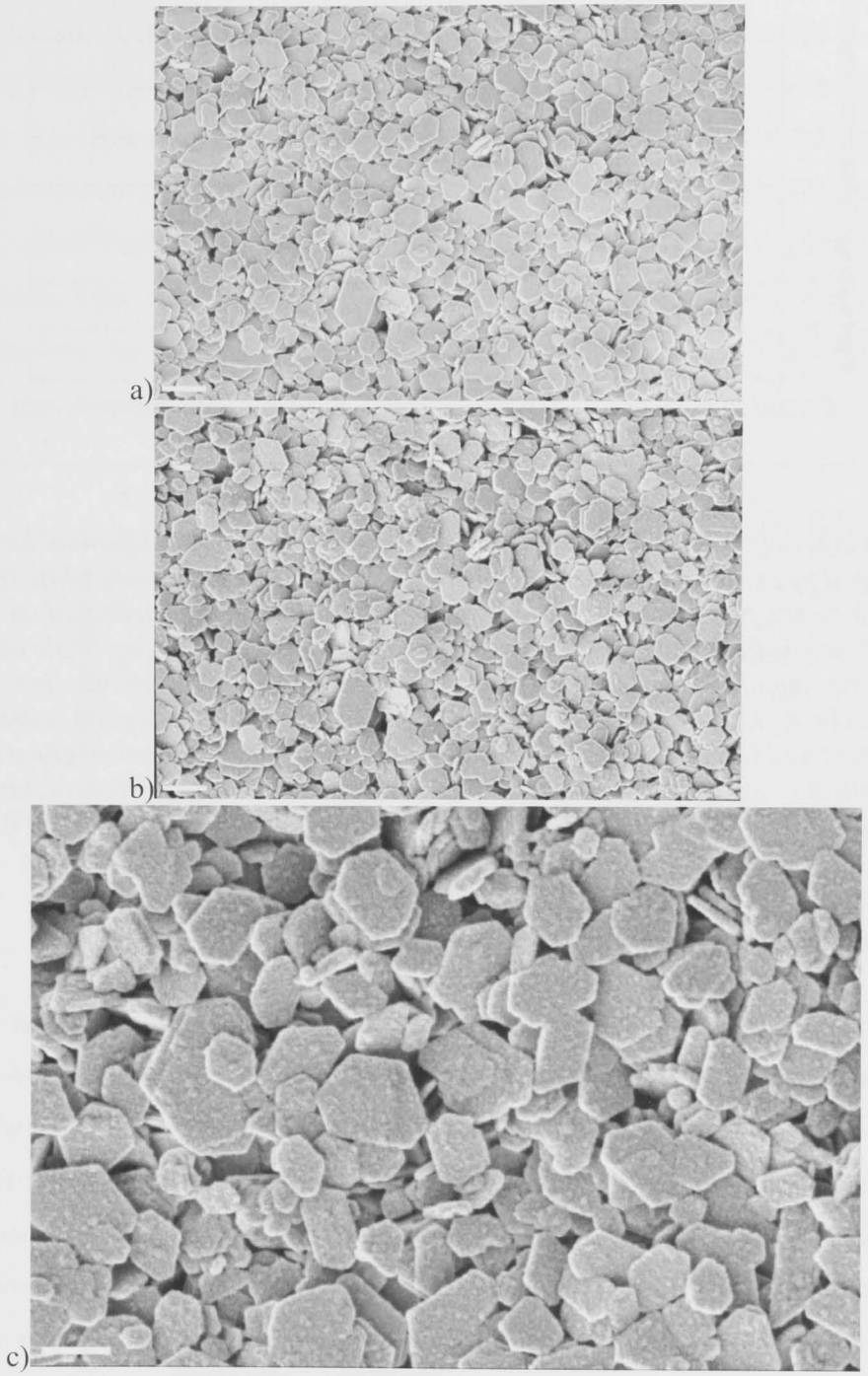

Figure 3.8. *a-b) FESEM micrographs, with scale bar 500 nm, of the same kaolinite coat area a) before, and b) after, a contact angle experiment in water at pH 4. After the experiment, the piece was immersed first in decalin, to dissolve non-adsorbed bulk oil, and then in n-heptane, so only asphaltene-based adsorbate remains. Both stages a-b were imaged without a conducting coat. c) Close-up image, with scale bar 250 nm, of a subarea after the contact angle experiment, showing at higher magnification the nodule texture of asphaltene-based adsorbate on kaolinite particles.*

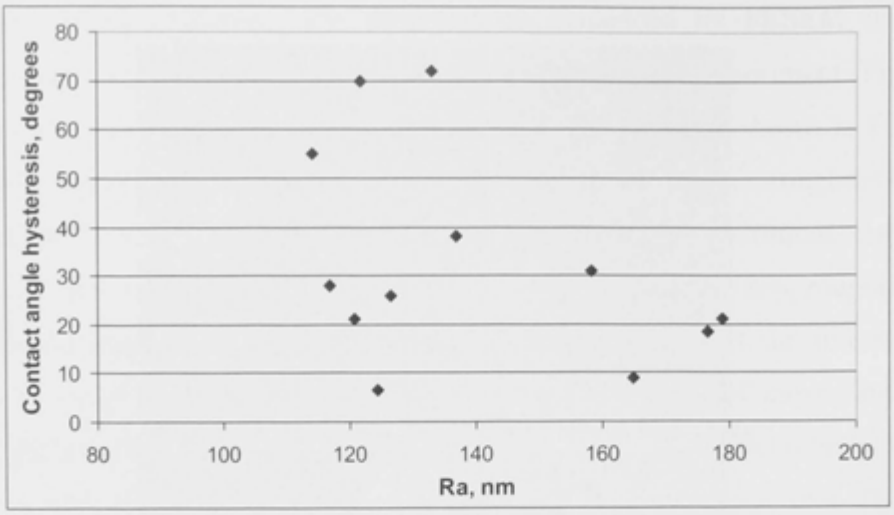

Figure 3.9. *Arithmetic-mean absolute roughness Ra of various individual kaolinite-coated pieces, averaged over four subareas of 157x118 μm^2 from white-light profilometry, plotted versus oil-drop contact angle hysteresis measured on it for particular salt solutions. Profilometry was performed after the contact angle experiment and post-rinsing of the oily coat by immersion of the piece first in decalin and then in n-heptane. Owing to the lack of movement of kaolinite particles during the contact angle experiment and solvent rinsing, evidenced in Figure 3.8, the plotted roughness values are identical to their values before the experiment. Least squares fitting of this data to simple functional forms yield a maximum coefficient of determination, R^2, of 0.16 for a linear fit, demonstrating the lack of correlation.*

Sodium chloride brines

Figure 3.10 plots the contact angle results for the NaCl-only brines, at the four concentrations from 0 to 1 M, each at the three pH values of 4, natural (5.5-6.1), and 9 in Table 3.2. Receding and advancing angles are presented in Figure 3.10a, while their difference is plotted as the hysteresis in Figure 3.10b. Receding angle varies little, with an average of 36.1° and standard deviation 6.1°, and without dependence on salt concentration or pH. This is expected for forced drop growth prior to adhesion onset, given that oil-brine interfacial tension varies little over this matrix of brines for crude oils very similar to ours (56; 74). After aging in this grown state for 30 min., followed by retraction, the brine-advancing angle now displays a wide range of values, from 30° to 121°, and clear trends. Advancing angle always exceeds receding angle, indeed for all experiments in this study, again as expected. Owing to the constancy of the receding angle, the hysteresis in Figure 3.10b displays almost identical trends to the advancing angle. It increases with decreasing pH, apparently somewhat weakly from pH 9 to the natural state, then much more pronounced from natural to pH 4. At pH 4 the oil-kaolinite adhesion increases strongly with decreasing NaCl concentration. This is

supported by an extra duplicate pair of experiments at 0.005 M NaCl and pH 4, which gave hysteresis of 87.6±5.0°. These four non-zero concentrations at pH 4 exhibit a strong negative, linear correlation between hysteresis and logarithm of concentration (Figure 3.13). Hysteresis apparently reaches a plateau at around 0.005 M, as its value there is similar to pure water at pH 4 in Figure 3.10b. At natural pH, oil-kaolinite adhesion, albeit weaker, also increases linearly with decrease in the logarithm of NaCl concentration from 1 M (Figure 3.13), but appears to reach its plateau earlier, around 0.01 M. In turn, for pH 9, maximum hysteresis occurs already just below 0.1 M, with concentration decrease below 0.01 M now resulting in an adhesion reduction.

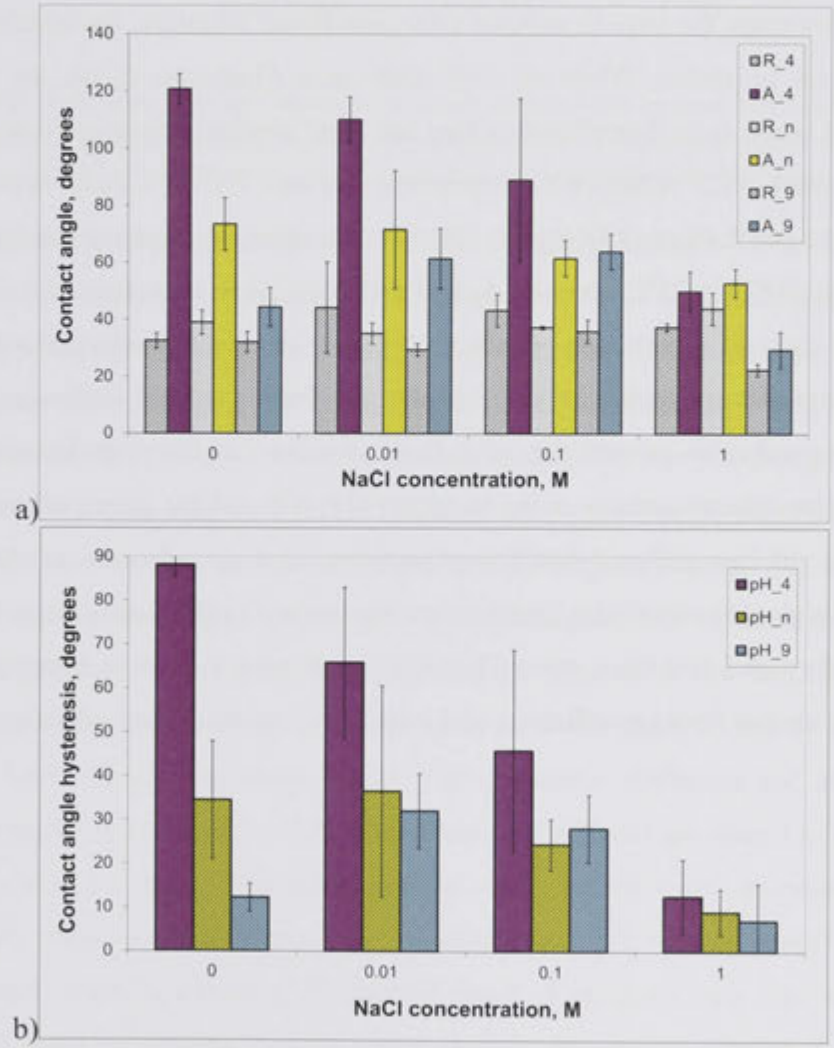

Figure 3.10. *Effect of NaCl concentration and acidity, for the three cases of pH 4, natural (n, close to 6), and 9, on oil drop contact angle on kaolinite for a) receding (R) and advancing (A) angles, and b)their hysteresis A-R.*

The angles in Figure 3.10b are replotted in the matrix of Figure 3.11, together with an annotation as to whether retraction of the oil drop leaves its bulk adhering to the kaolinite surface due to snap-off (adhesion, A), or results in clean removal (non-

adhesion, N), or gives the intermediate situation in which the bulk is removed while a small droplet(s) remains (transition, T). Brine compositions giving complete or partial adhesion are shaded. Generally, high hysteresis is associated with adhesion, e.g. the bottom-left extreme of 0.01 M NaCl at pH 4 in Figure 3.11, and low hysteresis characterises non-adhesion, e.g. top-right extreme of 1 M NaCl at pH 9. For compositions between these extremes, the correlation is not exact, with lower pH tending to give adhering droplet residues at comparable hysteresis values for which pH 9 results in complete removal.

Use of this simple binning into A, T and N behaviours allows a more direct comparison with adhesion maps for smooth mineral substrates in the literature, for which hysteresis values are not presented. While no such study used Minnelusa crude, the frequently investigated crude A-93 from Prudhoe Bay has quite similar properties (density 0.8942 gcm^{-3}, viscosity 21.2 mPa.s, n-C_7 asphaltene content 7.1 wt%, and acid and base numbers 0.14 and 2.42 mg KOH/g oil (44; 57)). Its adhesion maps on borosilicate glass (44) and mica (57) at 25°C give the dashed and dotted line boundaries in Figure 3.11, above and right of which non-adhesion (N) was observed. Some differences exist between these and our protocols; in particular, the former use pH buffers and only a 2 min. oil drop-substrate contact time. All three systems, and the vast majority of other crude oil-brine-silicate systems in the literature (44; 60), exhibit strong adhesion for the combination of low pH and NaCl concentration, and no adhesion at the opposite extreme of high pH and salinity. Distinctions thus reduce to the more precise location of their boundary and transition states. Kaolinite and mica appear to behave similarly, while glass shows stronger adhesion and a reduced region of non-adhesion in Figure 3.11.

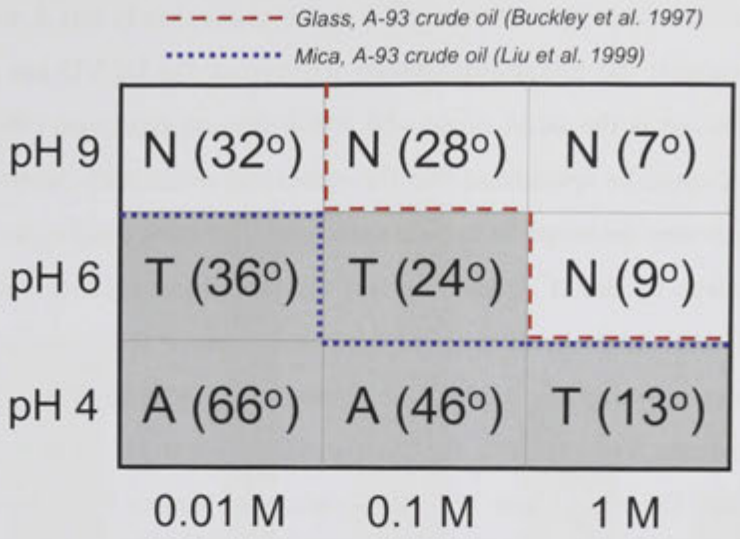

***Figure 3.11**. Adhesion map for Minnelusa crude on kaolinite versus NaCl concentration and pH, with A denoting adhesion, N non-adhesion, and T transition state. Boundaries, above and right of which non-adhesion occurs, are compared to literature systems.*

The charges of the oil-water and water-kaolinite interfaces in Table 3.2 and Figure 3.2a and Figure 3.1a explain, within the DLVO framework, most of the adhesion trends in Figure 3.10b, especially for lower salinity. At pH 4, polar oil components at the water interface are substantially protonated; Figure 3.2a is consistent with a reported isoelectric point (IEP) at pH 4.1 for Minnelusa crude (75). The net charge on the oil-water interface is thus positive (10^{-4} M NaCl) or only very weakly negative (>0.01 M NaCl) with a considerable population of positively charged domains (61). Kaolinite is net negatively charged; Figure 3.1a is in line with literature IEP values at pH 2-3 (71). The resulting electrostatic attraction is only slightly screened at low salt, and together with van der Waals attraction, leads to rupture of the water thin film and oil adhesion to substrate. Under these conditions Figure 3.8b-c directly evidences the alteration of uppermost kaolinite surfaces towards oil-wetness. On pH increase from 4 to 6, kaolinite becomes somewhat more negatively charged, and the oil-water interface becomes substantially more anionic (Table 3.2), switching their DLVO electrostatics towards repulsion and lessening adhesion. Further pH rise to 9 increases only the magnitude of these large negative charges, resulting in a smaller decrease in hysteresis in Figures 3.10b and 3.11.

Increasing salinity shrinks the range of electrostatic interaction, i.e. the Debye screening length, and thus zeta potential magnitudes decrease in Figures 3.1a and 3.2a. At pH 4, the increased screening of locally positively-charged oil domains from net negatively-charged kaolinite reduces hysteresis, although further adhesion may occur over much

longer times. The weaker hysteresis at pH 6 and 9 also exhibits this downward trend in Figure 3.10b, despite the increasing salinity decreasing the DLVO net repulsion. One possible explanation is the onset of non-DLVO hydration repulsion (60) above 0.1 M. Alternatively, it could be speculated that the increasing overlap of electric double layers at lower salt provides the scope to induce attraction. One such mechanism is protonation of the oil interface by the H^+ counterions of the acid-dissociated mineral surface (61; 64). A second mechanism could involve repulsion-induced reorientation of surface oil groups to expose polyaromatic asphaltene sheets, which may bind Na^+ ions and attract the mineral substrate. For kaolinite, the variety of charges on its faces and edges offers a third mechanism. Despite its low IEP, the amphoteric broken Si-O and Al-O bonds at edges remain negatively charged up to neutral pH (71), and some evidence points to alumina faces acting similarly (48). At natural pH, these edges and faces could attract deprotonated groups at the oil interface, and silica faces could attract the minority of protonated oil groups, to provide local adhesion.

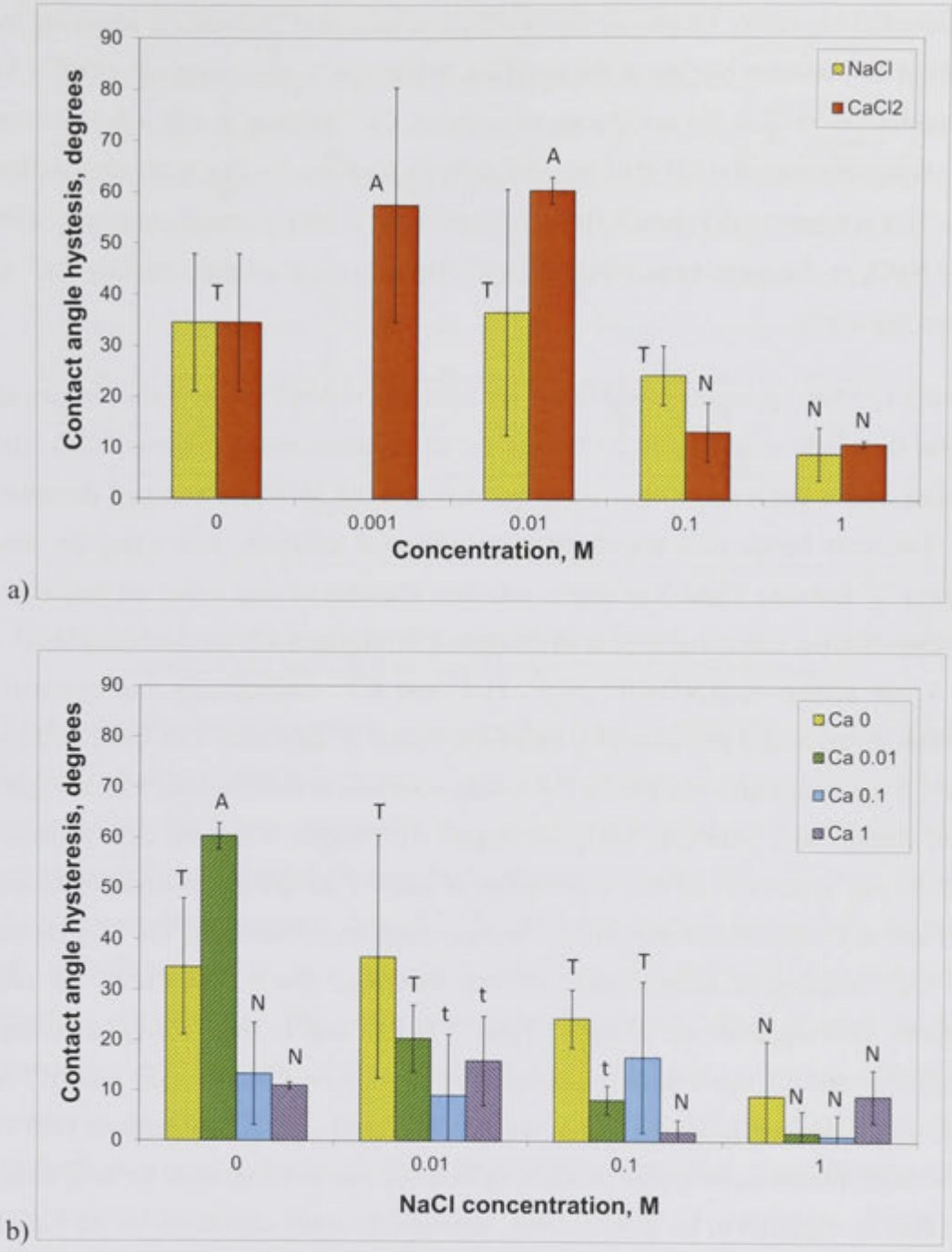

Figure 3.12. *Effect of NaCl and $CaCl_2$ concentrations on hysteresis at natural pH, for a) the single salts, and b) all solutions tested, including mixtures of these two.*

Effect of divalent cations

The presence of divalent ions in the aqueous phase is rarely addressed in the oil-mineral contact angle literature, as effects are ion- and oil-specific, and equilibration times can be lengthy (57; 62). However, they are an important reality in most environments. Table 3.2 and Figures 3.1b and 3.2b show the effect of calcium ions on the zeta potential of the two separate interfaces at natural pH. For both kaolinite and oil, Ca^{2+} reduces the

zeta potential negativity via the combined effects of increased electrostatic screening by dissolved ions and ion binding at the interface. While $CaCl_2$ concentrations of 0.1-1 M are required to reverse the net charge to positive, Ca^{2+} binding is still substantial at lower concentrations of 0.001-0.01 M, especially for kaolinite (in line with other studies (71)). This is apparent in Figure 3.1b from the increase in zeta potential magnitude with rising NaCl, as the more weakly binding Na^+ displaces more strongly binding Ca^{2+} to reassert negativity.

Figure 3.12 plots hysteresis in Table 3.2 for solutions of NaCl and/or $CaCl_2$ at natural pH, for the single salts (Figure 3.12a) and for all solutions tested (Figure 3.12b). The receding angles again show little variation, with average 35.7° and standard deviation 4.3°. The letter beside each bar classifies the observed adhesion, now using the sub-category "*t*" between *T* and *N* to denote substrate retention of only a tiny oil droplet(s). The classification correlates well with hysteresis in Figure 3.12; the hierarchy *A*, *T*, *t* and *N* has average angles 58.9°, 26.5°, 11.1° and 6.7°, emphasising that hysteresis provides a reasonably reproducible, indirect measure of adhesion. The most striking feature is the strong adhesion for the $CaCl_2$-only solutions at 0.001 and 0.01 M in Figure 3.12a, despite both interfaces being net negatively charged. From the zeta potential analysis, this appears to be due to attraction of anionic oil groups to kaolinite-bound Ca^{2+}, and to a lesser extent attraction of anionic kaolinite to oil-bound Ca^{2+}, combined with Ca^{2+} bridging of anionic sites on both interfaces. For 0.1 M $CaCl_2$, the two interfaces have opposite net charges (Table 3.2), but due to their strong screening, adhesion is virtually non-existent (although may develop over much longer times). The window of enhanced adhesion, within which multivalent cations can partially bind to one or both interfaces, or bridge them, at sufficiently low concentration for long-range attraction, is expected to be quite general, although naturally dependent on the cation exchange and binding properties of the particular mineral substrate and oil (57).

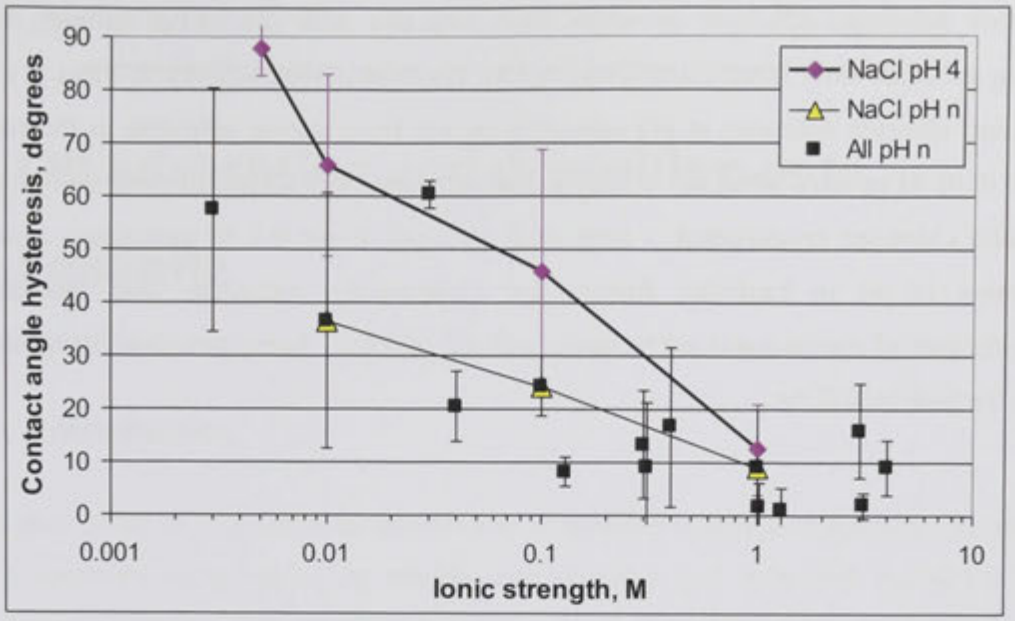

Figure 3.13. *Contact angle hysteresis versus ionic strength, for all 15 brines tested at natural pH, and the four NaCl brines at pH 4 (pink diamonds).*

The trend to decreasing hysteresis with increasing ionic strength again generally applies for $CaCl_2$ and its mixtures with NaCl. Figure 3.13 re-plots all data in Figure 3.12, and compares the NaCl-only subset with its counterparts at pH 4. At natural pH, all salt solutions with ionic strength above 0.1 M give hysteresis less than 17°, while all below 0.1 M give hysteresis greater than 20°. The pH 4 line is much steeper than for natural pH, reinforcing that H^+ is a potential determining ion, especially for the oil-water interface (Figure 3.2a). The two highest points for natural pH in Figure 3.13 (with hysteresis ~60°) are the above-mentioned Ca^{2+} pair, also potential determining, especially for the kaolinite-water interface (Table 3.2). Strong adhesion of oil to kaolinite in aqueous systems, at least over relatively short times, thus demands weakly screened electrostatics and a sufficiently high density of oppositely charged, or chargeable, domains on the two interfaces, and would be qualitatively consistent with DLVO modelling properly incorporating acid/base charge regulation and ion binding.

3.4 Conclusion

Uniform coats of kaolinite particles on a flat glass substrate were prepared to be sufficiently smooth and thin to allow reliable measurement of contact angles of captive crude oil drops in a range of salt solutions, without any particle removal. The contact angle hysteresis was used to infer the extent of oil adhesion via rupture of the intervening water film and anchoring of charged groups to kaolinite. For sodium

chloride solutions, adhesion decreases monotonically with pH and/or salinity, with strong adhesion only manifested under acidic conditions with salinity at most 0.1 M. Calcium chloride solutions at pH around 6 switch from strong adhesion in the range 0.001-0.01 M to weak adhesion at higher concentrations. For all mixtures of sodium and calcium chlorides investigated, a total ionic strength above 0.1 M guarantees a weak adhesion of oil to kaolinite. Results are qualitatively consistent with theoretical expectations of electrostatic interactions, with H^+ and Ca^{2+} being potential-determining ions for both interfaces.

4 Oil adsorption and deposition onto kaolinite

4.1 Introduction

The adsorption or deposition of dissolved or suspended organics on kaolinite is central to a spectrum of scenarios in natural environments and industrial extraction and separation processes. Owing to its two types of external basal face and the broken bonds at particle edges, combined with their cation exchange capacity from isomorphous substitution near the surfaces, kaolinite can exhibit a strong affinity for organics. As mentioned in Section 3.1, the petroleum industry alone provides many examples. Oil recovery depends on the reservoir wettability, which is dictated by the extent of adsorption/deposition of the crude oil's asphaltenes and resins to alter the originally water-wet surfaces of the minerals, such as kaolinite (76; 77; 78; 79). Recovery by water injection may dislodge oil-wet kaolinite particles, necessitating their separation from the produced water (80). Similar issues of wettability alteration and adhesion arise during remediation of soil or subsurface contamination by light or dense asphaltic products (64).

An extensive literature has been devoted to quantifying asphaltene adsorption and desorption to and from kaolinite. These studies almost exclusively use solutions, obtained by separating the asphaltenes from crude oil by precipitation in alkane and then dissolving them in a model solvent(s), most often toluene (81; 80; 82; 83). Equilibrium adsorption is then conveniently analysed by solution depletion using UV-vis spectrophotometry. It is usually inferred that adsorption is due to polar interactions between kaolinite and asphaltenes, possibly together with asphaltene surface precipitation (83). In some studies, water is incorporated, by dissolution in the solvent or pre-wetting of kaolinite, generally resulting in suppressed adsorption (81). X-ray absorption and Fourier transform infrared spectroscopies have been used to probe the state of asphaltene adsorbed from anhydrous or water-saturated toluene solutions, indicating that asphaltenes have highest affinity for the hydroxyl groups on the alumina face and broken edges (84).

This replacement of the crude oil by a model oil comprising its extracted asphaltenes and/or resins in organic solvent(s) will inevitably change the native aggregation state of these species. Further, in the vast majority of petroleum scenarios, from recovery to remediation, kaolinite is surrounded by a salt-containing aqueous phase, which the immiscible crude oil must then drain and rupture to contact the surface. Accordingly, asphaltene adsorption/deposition behaviour for the above-mentioned idealised single-solution phases can be distinctly different from this reality. Cryogenic scanning electron microscopy studies of crude oil and brine in kaolinite-containing rock often indicate that the oil phase is strongly associated with kaolinite (79). However, observations in complex, multiphase liquid-filled, rock/pore environments are difficult to generalise, and cannot resolve whether oil ruptures the final barrier of the water thin film sheathing kaolinite particles to come into true molecular contact. X-ray photoelectron spectroscopy of kaolinite particles agitated in crude oil and brine, and then solvent-flushed and dried, showed that asphaltene-based adsorption/deposition was greater in the presence of brine (85), in contrast to the above-mentioned solution-phase findings.

Other laboratory studies (44; 57; 58; 62) have attempted to more realistically imitate the formation of oil reservoirs, while instead simplifying the mineral phases by model substrates such as quartz and mica, as follows. The planar substrate is pre-equilibrated with the aqueous phase of interest (e.g. formation brine), and then drained by immersion in crude oil and aged at elevated temperature until equilibrium adsorption or deposition of asphaltenics has been established, over days or weeks. The substrate is then rinsed with organic solvents to remove the bulk oil, with or without drying, prior to analysis. The asphaltenics on these smooth model substrates are then characterised by their effect on contact angle. Receding and advancing contact angles are usually measured on the treated substrate using simple probe liquids, e.g. a decane drop in water (44; 58; 62; 65; 86) , so as not to further alter this wettability state. Further, the fine-scale morphology of the deposits is imaged by AFM. This imaging is variously performed in air (44; 58; 65; 87; 88; 74) or under organic solvent (74; 89) or water (74; 88; 89; 90). These studies of model silicates have also shown that the wettability alteration due to crude oil is greater in the presence of brine, but also more variable, depending on the solution conditions.

Chapter 3 described a method to prepare smooth, thin and robust coats of kaolinite on glass slides and used this substrate to measure contact angles and their hysteresis after short-time exposure to a crude oil drop in various salt solutions. These substrates are used in Chapter 4 to similarly extend to the case of kaolinite the above-mentioned techniques for recreating and analysing the adsorption/deposition of asphaltenics after longer-time oil exposure. In

addition to AFM, the amount and nanoscale distribution of asphaltenics on kaolinite platelets are characterised by fluorescence spectroscopy and FESEM. The results in Chapters 3 and 4 are then compared for these same oil-brine-kaolinite combinations.

4.2 Materials and methods

4.2.1 Materials

The experiments used the same kaolinite (KGa-1b) and kaolinite-coated glass slides as detailed in Chapters 3.2.1 and 3.3.1, as well as the same crude oil (Minnelusa) and the same 25 solutions of sodium chloride and/or calcium chloride in Chapter 3.2.2, for which all zeta potentials were given in Table 3.2 and Figures 3.1 and 3.2. The probe alkane used in contact angle measurements was n-decane (99%, Sigma-Aldrich), from which surface active compounds were removed beforehand by passing it through a column of a clean silica gel and alumina powder pre-cleaned in a RF water-vapour plasma unit. In addition to the solvents decalin and n-heptane mentioned in Chapter 3.2.2, the solvents toluene (99.5%), THF (tetrahydrofuran, 99.9%), chloroform (99%) and methanol (99.8%) were also used as received from Sigma-Aldrich.

4.2.2 Oil aging of kaolinite powder and UV-vis spectroscopy

Preliminary experiments were performed on kaolinite powder to assess the best combination of organic solvents for removing asphaltene deposits. Water-washed kaolinite was dried at 60 °C, and 0.12 g was added to 4.3 g of crude oil, sonicated for 15 min., and aged (sealed) at 60 °C for 3 days, then centrifuged (1000 g for 10 min.) to decant the oil above the kaolinite sediment. To dissolve residual bulk oil, decalin (10 g) was added, then agitated, centrifuged, and decanted, and then repeated three times until the decalin was colourless, then repeated using n-heptane to remove maltenes. To 0.017 g of the treated kaolinite powder, 2.4 ml of each of six solvents was added, namely toluene, THF, chloroform, and their azeotropic blends with methanol (72.2, 31.1 and 12.7 wt% methanol, respectively). These were aged (sealed) at 50 °C for two days, centrifuged, and the discoloured solvent was decanted, then evaporated. The asphaltene-based residues were redissolved in the azeotropic chloroform/methanol blend, and analysed with a UV-vis scanning spectrophotometer (Shimatzu UV-3101PC) using 10 mm path-length quartz cuvettes, to record transmission spectra over 800-300 nm. Calibration standards were made by heptane precipitation and separation of the asphaltene fraction of the crude oil, and then dissolved at $4x10^{-4}$– $4x10^{-3}$ wt% in this

same azeotropic blend.

4.2.3 Aqueous/oil aging of kaolinite-coated substrates

For each salt solution, 4 glass vials were filled with 3.0 ml, into which a kaolinite-coated glass piece (~7.5x26 mm^2) was immersed, then lightly vacuum degassed for 10 min. The vials were equilibrated at 60 °C for 2 days, or only 20 h. for the basic solutions (after which their pH was 8.3±0.6) to avoid further acidification by CO_2 uptake. Each piece was removed with tweezers and in this water-saturated state, immediately immersed (< 2 s transfer time) in 2.0 ml of crude oil, preheated to 60 °C, in a glass vial. The sealed vials were aged at 60 °C for 8 days, and then each piece was directly transferred to a 2.5 ml bath of decalin, to dissolve bulk oil, and after 1 h. to a second such bath to soak for 40 h. This was followed by transfer to a 2.5 ml bath of heptane for 10 days, to remove maltenes, and then to 2.5 ml of 77.5/22.5 (v/v) methanol/water for 50 min., to dissolve salt. After ambient drying, the uncoated backside of each piece was wiped with water-wetted tissue to remove any oil deposits.

4.2.4 Measurements of aqueous/oil-aged substrates

As asphaltene-based residues on the kaolinite-coated pieces prepared in Chapter 4.2.3 produce a brownish tinge, a document scanner (Konica Minolta C252) provided a rapid, non-destructive means to assess deposition over this large data set. All 100 pieces (i.e. the 4 replicates for each of the 25 salt solutions tested), plus untreated control pieces, were scanned simultaneously with coated side facing the glass. From the 600 dpi image, greyscale value (GSV) statistics over each piece were obtained using ImageJ software. Calibration of average GSV to asphaltene amount was performed for 14 pieces by soaking each in a known amount (2.4-7.8 ml) of azeotropic chloroform/methanol blend (the solvent combination in Chapter 4.2.2 giving most complete deposit removal) in a sealed flask at 50 °C for 2 days. The solvent with dissolved deposit was analysed with a FluoroMax-3 spectrofluorometer (Horiba Jobin Yvon), using quartz cuvettes (10x10x40 mm^3; Starna Cells) to record emission spectra over 380-550 nm from 340 nm excitation. Calibration was performed using the same asphaltene stock solution as in Chapter 4.2.2, but diluted further to $3x10^{-6}$-$1x10^{-3}$ wt%.

Other sample pieces were analysed by microscopy, using the same FESEM and AFM techniques as described in Chapter 3.2.3, to image deposition on kaolinite particles. Other such deposit-bearing sample pieces were analysed by contact angle goniometry as

described in Chapter 3.2.4 (see Figure 3.3), but now using a decane drop in water. Further, the time for which the drop was left at the syringe tip prior to contact and receding angle measurement, and the duration of contact prior to retraction and advancing angle measurement, were both shortened to 2 min.

4.3 Results and discussion

4.3.1 Solvent dependence of oil deposit removed from kaolinite powder

The absorbance of the asphaltene solution standards at 525 nm exhibited Beer-Lambert linear dependence on concentration, from which was derived the asphaltene mass per dry kaolinite mass extracted using the six solvents in Chapter 4.2.2. In Figure 4.1a, of the pure solvents, THF removes most asphaltene, while addition of methanol in its azeotropic ratio greatly enhances the removal ability of chloroform, but decreases that of the other two solvents. The 27.4 mg/g removed using chloroform/methanol corresponds to 2.35 mg/m^2 of total kaolinite surface (69), and an average asphaltene layer thickness of 1.99 nm (assuming complete area coverage and asphaltene density 1.18 g/cm^3). Dubey and Waxman (91) measured equilibrium adsorption of asphaltene onto kaolinite from a dilute toluene/n-dodecane solution, and subsequent desorption by repeated washing in various solvents. Amounts removed by toluene, chloroform and azeotropic choloroform/methanol were 5.3, 12.3 and 31.2 mg/g, in close agreement with Figure 4.1a from adsorption/deposition in crude oil, and with the latter also being the highest amongst all solvents tested. However, their value of 8.9 mg/g for azeotropic toluene/methanol greatly exceeds that in Figure 4.1a.

Figure 4.1b replots Figure 4.1a versus literature values (92) of the total Hansen solubility parameter and its three components for the solvents, with those for the blends taken as the volume-weighted averages. All four parameters identify the chloroform/methanol azeotrope as the most optimal, with asphaltene removal rising monotonically to this maximum and similarly dropping beyond it. All three pure solvents have insufficient H-bonding capacity to disrupt the acid-base associations contributing to cohesion of asphaltene sheets in the adsorbed aggregates and their adhesion to kaolinite. Addition of the strong H-bonding methanol, as proton donor and acceptor, markedly improves the debonding capacity of chloroform, while the higher methanol contents of the azeotrope for THF, and in turn toluene, instil too much polarity, inhibiting penetration into the asphaltene matrix. While the adsorbate/deposit

is based on asphaltene (owing to the dissolution of bulk maltenes in heptane), some maltene components, most likely resins, presumably remain strongly associated with asphaltene. The deposit fractions removed by each solvent and dried could be completely redissolved in toluene for all but the chloroform/methanol sample, in which a brown sediment was also present. As asphaltenes are by definition toluene soluble (46), this azeotrope is uniquely advantaged by its ability to also remove asphaltene-associated resins. Accordingly, this azeotropic blend was chosen for deposition extraction from the aqueous/oil-treated kaolinite coats in Chapter 4.2.4 and discussed below in Chapter 4.3.2.

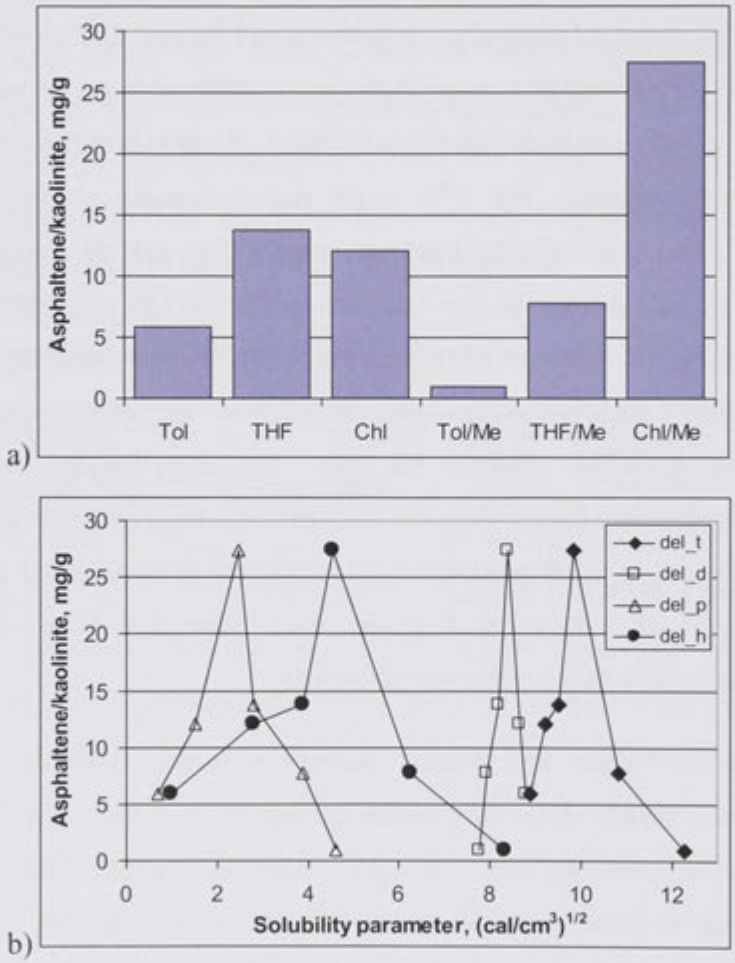

Figure 4.1. *a) Mass ratio of asphaltene extracted from kaolinite powder using the three solvents (Tol = toluene, Chl = chloroform) and their azeotropic methanol (Me) blends, and b) plotted against total (t), dispersion (d), polar (p) and H-bonding (h) solubility parameter components for each solvent and blend.*

4.3.2 Oil deposition on substrates in salt solutions

As observed in Chapter 3, the kaolinite coats all remained intact and without particle

loss during water/oil-aging and solvent post-rinsing. Any discolouration due to deposition was uniform across the piece area. The GSV of the scanned images, defined as ranging from 0 (completely dark) to 255 (white), was 238.6±1.1 for untreated kaolinite-coated pieces. The GSV of each treated piece was subtracted from this untreated mean to give a discolouration measure, termed "deposition GSV", increasing from 0 as deposition increases. For each salt solution used, the mean and standard deviation of deposition GSV over the 4 pieces was obtained. The standard deviation averaged 3.7, amounting to an average coefficient of variation of 21%. This value is somewhat high, due to some variability in deposition for a given salt solution and magnified by subtraction of two large GSV to obtain the smaller deposition GSV.

The accuracy of this scanning method was assessed on a subset of 14 pieces, spanning the gamut of deposition GSV, by the destructive technique of azeotropic chloroform/methanol solvent extraction of the deposits from the kaolinite coats and spectroscopy of their resulting solutions. Since the kaolinite, and hence deposit, amount per coated piece is very small, UV-vis spectroscopy is insufficiently sensitive, necessitating the use of fluorescence spectroscopy, which utilises the polyaromatic asphaltenes' natural fluorescence (46). The solution standards of pure asphaltene in chloroform/methanol gave peak fluorescence for 340 nm excitation, with broad emission maximum at 493 nm. The difference in emitted intensity between the solution and solvent blend is plotted versus concentration in Figure 4.2a. The lowest concentration is close to the detection limit, while at the high end, sensitivity begins to decrease markedly due to re-absorption of emitted fluorescence. The interval in between is very well fitted by the power law shown, with exponent close to unity.

For all solutions of deposits extracted from the kaolinite substrates, the emission peak is shifted slightly to 498 nm, presumably due to presence of resins. Dilutions were chosen for the intensity difference to lie in the interval in Figure 4.2a. Conversion of this intensity to concentration via the power law, and in turn to dry deposit mass per planar projected area of kaolinite-coated slide, gives the comparison to the corresponding deposition GSV of the 14 pieces in Figure 4.2b. The correlation is very strong, so this fit can be inverted to convert the measured deposition GSV of all samples to deposit mass/area with sufficient accuracy to identify the trends.

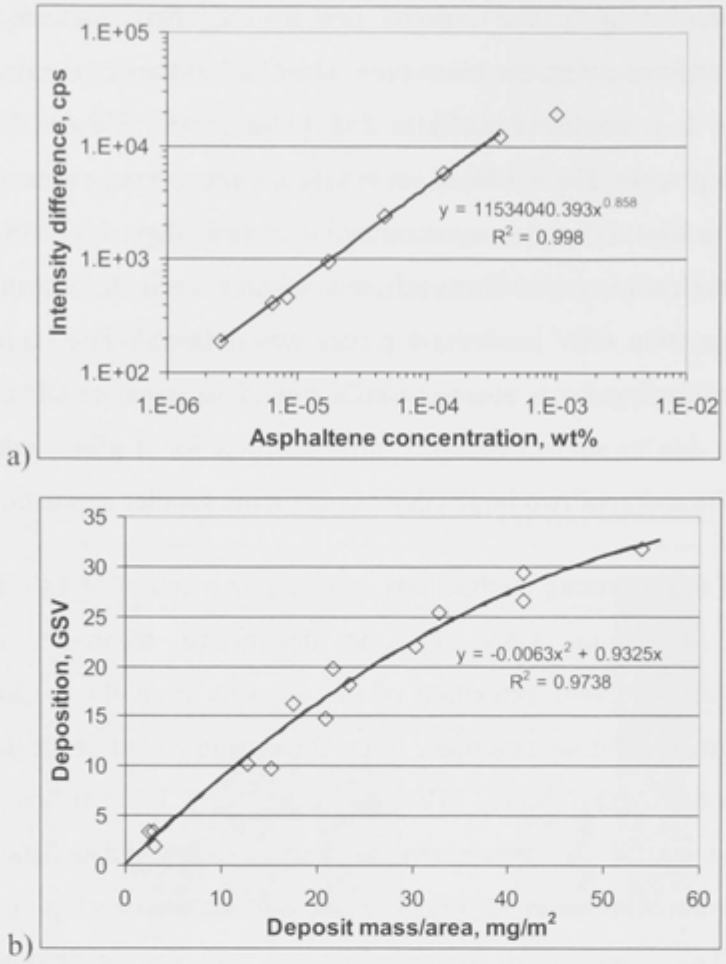

Figure 4.2. *a) Fluorescence emission intensity of asphaltenes dissolved in azeotropic chloroform/methanol blend versus concentration. b) Correlation between asphaltene-based deposition on kaolinite-coated slides measured by average greyscale value and by calibrated fluorescence of extracted solution (normalised to slide planar area).*

Figure 4.3 plots the oil deposit mass per planar area thus obtained, averaged over the 4 pieces per salt solution, and with error bars from its standard deviation, as a function of NaCl concentration (0, 0.01, 0.1 and 1M), either at the three pH values of 4, natural and 9 in Figure 4.3a (all without calcium) or with these same concentrations of added $CaCl_2$ in Figure 4.3b (all at natural pH). This quantitative information is complemented by representative FESEM surface images in Figure 4.4 of the deposit distribution for six samples. Further, Figure 4.5 shows images from one piece of the sample with highest average deposition (34.0 mg/m^2), before and after extraction in chloroform/methanol. Only thin, faint trails of residue remain post-extraction, and samples with less deposit appear to be completely cleaned, thus the values in Figure 4.3 are very close to the true deposited amounts.

In Figure 4.3a, deposition for acidic and natural pH is very similar, and both tend to

decrease with NaCl salinity, with the most significant decrease occurring at 1M. At pH 9, deposition does not exhibit this decrease, instead switching from less to more than its lower pH counterparts as salinity passes 0.1M. Only three NaCl solutions, namely 0.01M at pH 9 and 1M at pH 4 and natural, give decidedly lower deposition. Figure 4.4a and c provide FESEM images for the two NaCl extremes, 0.01M at pH 9 and 1M at pH 4, respectively, while Figure 4.4b is for intermediate NaCl salinity and acidity (0.1M at natural pH) with typically high deposition. For all salt solutions, deposits take the form of primary nanoparticles, of size on the order of 10 nm, which aggregate or merge into larger features. All solutions giving substantial deposition, i.e. excluding the three samples in Figure 4.3a, appear almost identical to Figure 4.4b, with a single layer of nanoparticles and their assemblies decorating all visible kaolinite faces and edges. Even for kaolinite well shielded by overlying plates providing tight constrictions, water has been displaced for oil to directly contact the surfaces and alter their wettability. The depth in the coat to which infiltration occurs cannot be determined from these images. In Figure 4.4c and the very similar images (not shown) for 1M NaCl at natural pH, oil has also made substantial inroads into the coat surface pores, yet has been largely hindered from depositing on faces, while edges are heavily covered, appearing thicker and fluffier than their sharp counterparts for untreated kaolinite in Figure 3.4a. At the opposite compositional extreme of low NaCl salinity and high pH in Fig. 4a, kaolinite edges are now mainly deposit-free, while outermost faces bear the majority of the sporadic deposits.

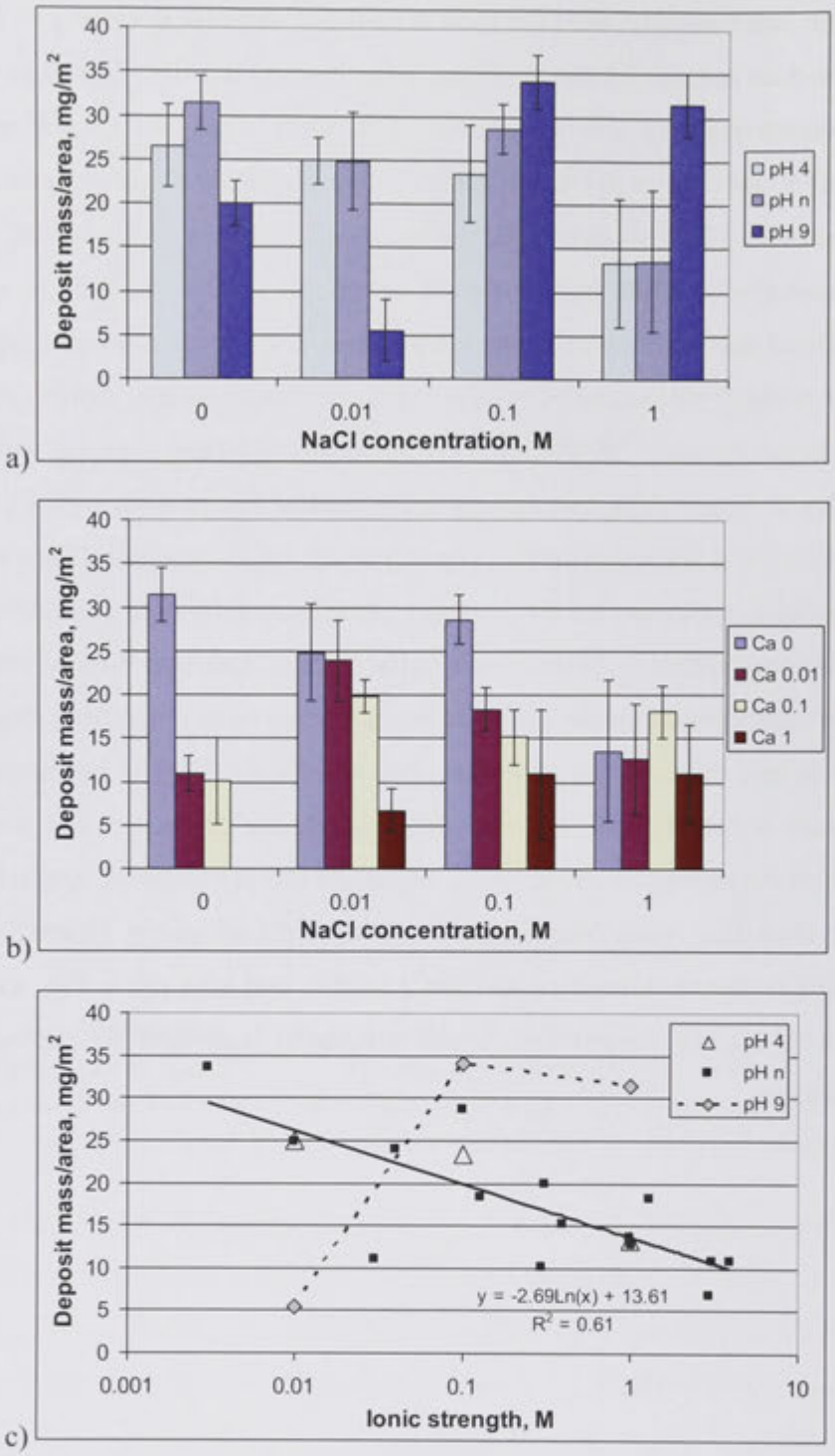

Figure 4.3. *Oil deposit mass per planar area of kaolinite-coated substrate from oil aging in salt solution, versus its NaCl concentration, and a) pH, with "n" denoting its natural value (pH 5.7±0.4), or b) concentration of added $CaCl_2$ at pH n. c) All data versus total ionic strength of salt solution, with straight line the best fit to pH n and 4, and dotted line joining pH 9 data.*

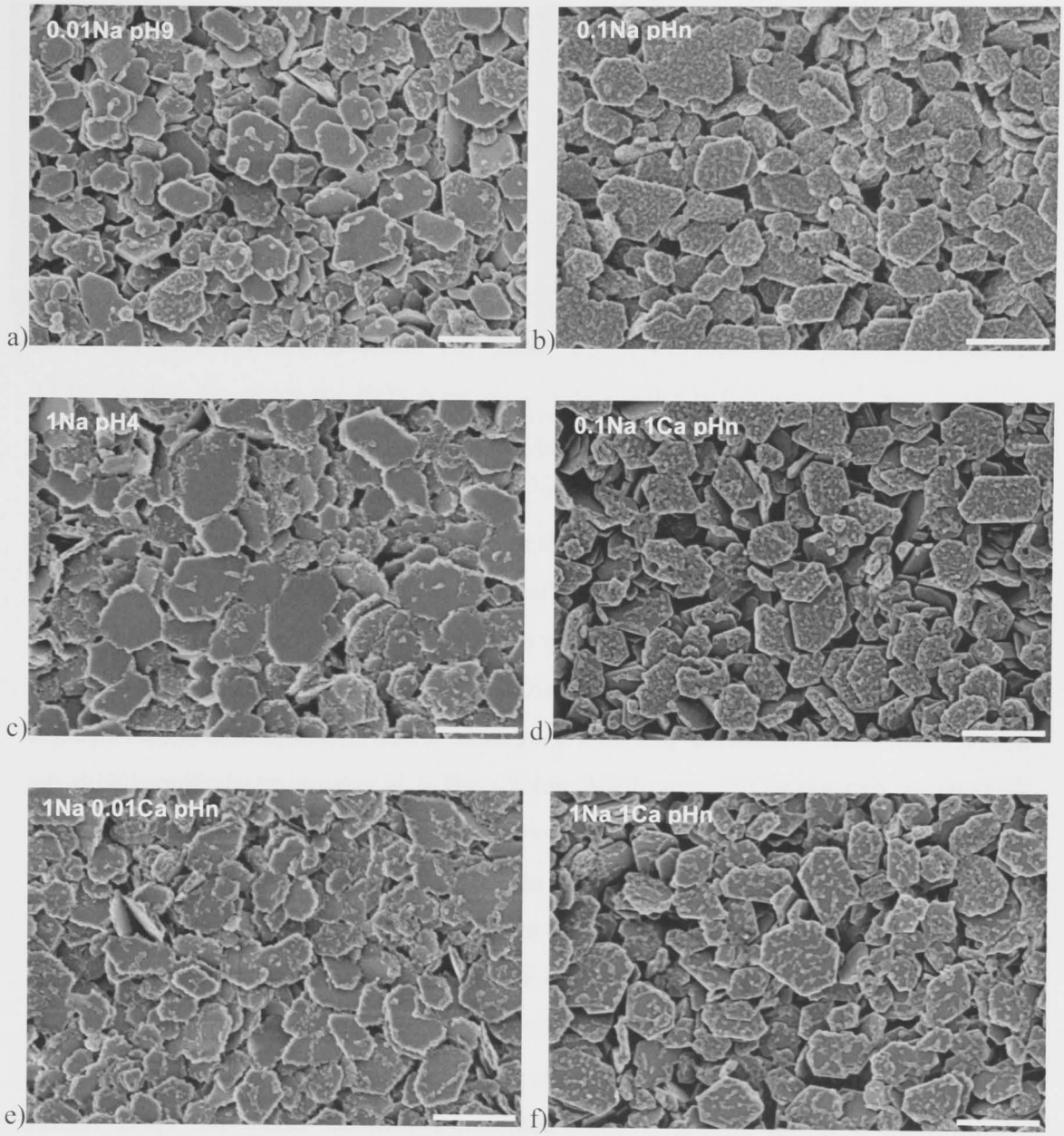

Figure 4.4. *FESEM images of kaolinite-coated substrates with oil deposits after aging, for salt solutions: a) 0.01M NaCl at pH 9, b) 0.1M NaCl at pH n, c) 1M NaCl at pH 4, d) 0.1M NaCl + 1M $CaCl_2$ at pH n, e) 1M NaCl + 0.01M $CaCl_2$ at pH n, and f) 1M NaCl + 1M $CaCl_2$ at pH n. Scale bars are 500 nm.*

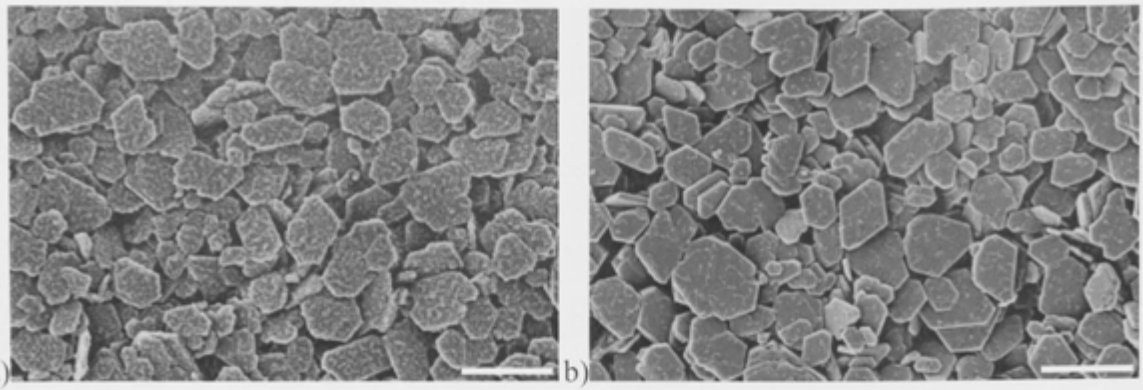

Figure 4.5. *FESEM images of substrate with oil deposits after aging, for 0.1M NaCl at pH 9, in the states a) before, or b) after, chloroform/methanol extraction. Scale bars are 500 nm.*

For the solutions containing calcium, deposition in Figure 4.3b lessens with Ca^{2+} content at fixed NaCl, although the trend is masked at 1M NaCl by this overwhelming presence of Na^{+}. Deposition also generally decreases with NaCl content at fixed $CaCl_2$, although again naturally masked at high Ca^{2+}, however the values are lower in the absence of NaCl. The scatter plot in Figure 4.3c for all salt solutions shows that the decrease in deposition for natural pH and for pH 4 is approximately linear with the logarithm of total ionic strength. For all sodium-containing solutions giving substantial deposition, i.e. all but five samples with 1M NaCl or $CaCl_2$ in Figure 4.3b, the FESEM images appear qualitatively as in Figure 4.4b, bearing deposit on all kaolinite faces and edges, both at and below the coat outer surface. Reduction in deposition, e.g. from 0 to 0.01 to 0.1M $CaCl_2$ at fixed 0.1M NaCl in Figure 4.3b, results from progressive decrease in the density of asphaltene nanoparticle coverage on each kaolinite face in Figure 4.4b. It is not known whether depth of deposition below the upper realms accessible to FESEM also decreases in tandem. On further increasing $CaCl_2$ content to 1M at this fixed 0.1M NaCl, the state of decreased deposition in Figure 4.3b is represented by the image in Figure 4.4d. While the outer faces of the outermost particles, and their edges, bear asphaltene, the vast majority of kaolinite below is deposit-free. The sample for 1M $CaCl_2$ with 1M NaCl, having similarly low deposition in Figure 4.3b, has this same limited penetration (Figure 4.4f). The main effect of high $CaCl_2$ concentration is thus to reduce oil ingress into the kaolinite aggregate. In Figure 4.4e, the (low) deposition for 1M NaCl with 0.01M $CaCl_2$ principally occurs on plate edges, as was the case for the NaCl solution without this small fraction of added Ca^{2+}, at both natural pH and pH 4 (Figure 4.4c). So for high NaCl salinity, if $CaCl_2$ is only sparingly present and pH is not too high, the main mechanism limiting oil-wetness is

stabilisation of kaolinite faces against deposition.

AFM imaging allows measurement of oil deposit thickness on the upper kaolinite particles. For 0.1M NaCl at natural pH, representative of significant deposition, Figure 4.6a shows a height image from the same sample as in Figure 4.4b, although now without the platinum coat. By recording line profiles over kaolinite bearing deposit, and subtracting the sloping linear baseline of the platelet, deposit height profiles such as those in Figure 4.6b are obtained. The peak height of individual deposit aggregates is 13.0±2.4 nm, the average height over each such feature is 6.6 nm, and their kaolinite face coverage fraction is 0.57, thus the face-averaged deposit thickness is 3.8 nm, equivalent to 4.5 mg/m^2 counted per kaolinite face area. This is almost twice the value for kaolinite powder aged only in oil in Chapter 4.3.1, and more than double the maximum amounts (2.07±0.44 mg/m^2) adsorbed on kaolinite from toluene/heptane for five different asphaltenes by Dudasova et al (80). Thus, salt solutions can greatly enhance adsorption/deposition, at least on the uppermost faces. This estimate of 4.5 mg/m^2 must be multiplied by the total ratio of kaolinite uppermost face area to planar area of the coat to be compared to the values in Figure 4.3. This ratio is presumably fairly close to unity, thus the span of 5.5-34 mg/m^2 in Figure 4.3 is roughly equivalent to 1.2-7.6 times this uppermost face amount. For the lower limit, penetration scarcely proceeds beyond this top face (in agreement with FESEM); while at the upper limit it extends to partially cover the underside face and many particles below.

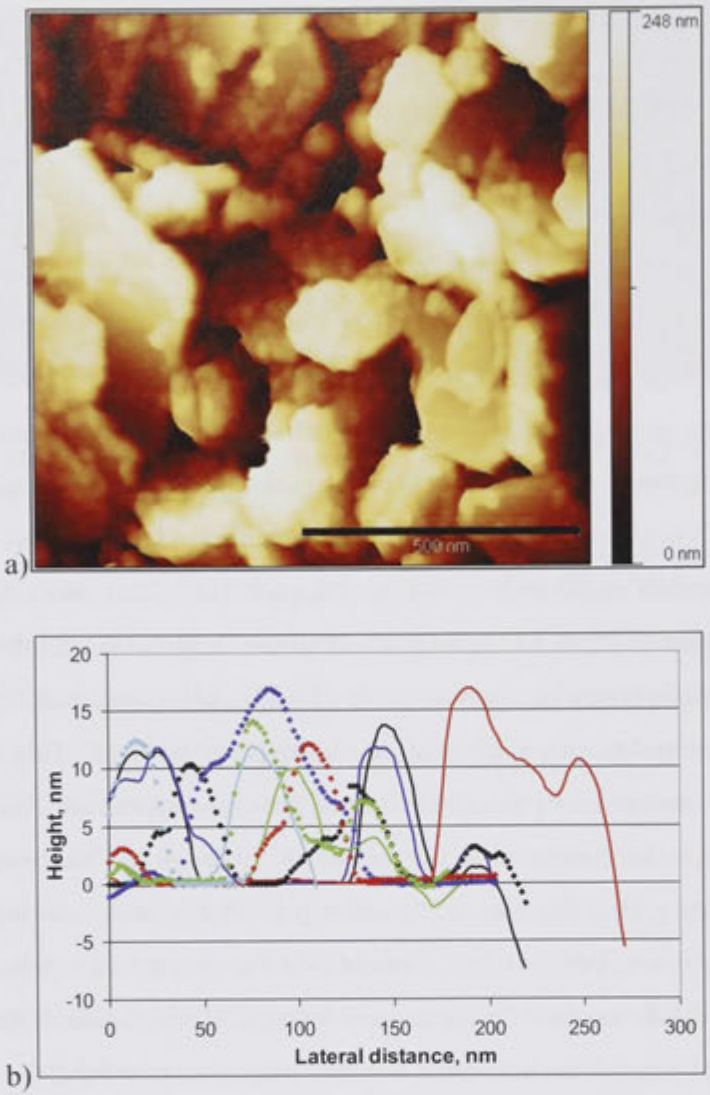

Figure 4.6. *a) AFM height image of substrate with oil deposits after aging, for 0.1M NaCl at natural pH, with scale bar 500 nm; b) 10 line profiles of deposit height on kaolinite plates.*

4.3.3 Interpretation of interfacial interactions

The results of the zeta potential measurements of kaolinite particles (ζ_k) or crude oil emulsion droplets (ζ_o) in the salt solutions in Table 3.2 and Figures 3.1 and 3.2 aid in shedding light on the intermolecular mechanisms responsible for the behaviours in Figures 4.3 and 4.4. The oil's isoelectric point is very close to pH 4, in agreement with the literature value (75), e.g. ζ_o = +21.6 mV for trace (10^{-4}M) NaCl and -7.1 mV for 0.01M NaCl in Figure 3.2a. Protonated base groups are thus plentiful at the oil-water interface. Kaolinite is already net negatively charged at pH 4, e.g. ζ_k = -15.8 and -16.7 mV at trace and 0.01M NaCl in Figure 3.1a, respectively, again in agreement with the literature (71). The prolonged aging allows ample time for protonated oil groups to

locally attract the opposite charges on kaolinite, locally rupturing the water thin film and leading to local deposition. Once some outer surfaces of the kaolinite aggregate are rendered oil-wet, the contact angle of water-oil menisci increases, switching their curvature from concave to convex and driving the emptying of water-filled surface pores to propagate deposition.

On increasing pH to 6, oil becomes decidedly more negatively charged, e.g. ζ_o = -51.2 mV for 0.01M NaCl Figure 3.2a, while kaolinite is slightly more negative (-18.5 mV for 0.01M NaCl). However, deposit amounts in Figure 4.3a remain undiminished from pH 4, thus sufficient local attraction must remain to initiate and propagate deposition. Presumably, the main source of attraction is now between deprotonated acid groups of the oil and positively charged kaolinite edges and alumina faces (48; 93). At these two pH conditions, deposition in Figure 4.3a decreases only slightly with increasing NaCl salinity, thus apparently van der Waals attraction sufficiently thins the water film for even quite strongly screened electrostatic attraction to lead to oil-kaolinite bonding. At the extreme of 1M NaCl, the deposition is decidedly less though, and restricted to kaolinite edges. One explanation could be hydration repulsion, consistent with the literature observation that the thickness of the repelling structured water film at clay edges can be ten times less than at the basal surfaces (93). Other studies (94) observed a high propensity for oil deposition onto tightly curved convex substrates, similar to kaolinite edges. Water films thinning to conform to such features will rupture under the compressive contribution of their interfacial curvature to the disjoining pressure. It is possible that kaolinite edge deposition pinches off thicker water films on faces, resisting further drainage and deposition.

At pH 9, both the oil interface and all faces and edges of kaolinite are negatively charged, e.g. ζ_o = -78.9 mV and ζ_k = -47.6 mV for 0.01M NaCl in Figures 3.1a and 3.2a, thus their long-range electrostatic repulsion at low NaCl salinity should resist wettability alteration. Figure 4.3a exhibits this trend, with lower deposition at 0.01M NaCl than for pure water, possibly due to Na^+ replacing H^+ as a more weakly bound counterion for kaolinite (93). It is not clear why this trend reverses at higher NaCl salinity. One speculation is that, during aging, the anionic groups of the polar oil molecules are repelled inwards, with this reorientation exposing the polyaromatic asphaltene sheets, which may bind Na^+ ions and attract the negatively charged kaolinite.

In the case of the salt solutions containing calcium at natural pH, the systematic

reduction in deposition with increasing $CaCl_2$ at fixed NaCl in Figure 4.3b goes hand in hand with a similar systematic decrease in zeta potential negativity of both oil and kaolinite in Figures 3.1b and 3.2b. For example, at 0.01M $CaCl_2$, ζ_o and ζ_k are reduced to -27.5 and -7.5 mV, respectively, and for all other calcium-containing salt solutions, ζ_o lies between -16.3 and +1.6 mV. This is due to the very strong screening effect of Ca^{2+} and its reduction of surface charge magnitude by binding to deprotonated acid group sites at the oil interface, and also partially displacing Na^+ as more strongly binding counterion at negatively charged kaolinite sites. Reduction in net negativity of both interfaces might be expected to enhance their attraction and thus deposition. However as discussed above, the heterogeneous charge make-up of both interfaces dictates that the main effect of calcium addition is to weaken local attraction between oppositely charged patches, principally deprotonated oil groups and positively-charged kaolinite edges and alumina faces. Thus even for situations in which the net zeta potentials have opposite sign, e.g. ζ_o = -7.8 mV and ζ_k = +0.9 mV at 0.1M $CaCl_2$, the deposition in Figure 4.3b is minimal. The fact that, even for mixed solutions with 1M $CaCl_2$, the uppermost kaolinite faces bear deposit (Figure 4.4d, f) may be a kinetic effect, as oil first encountering these faces on immersion has little time to equilibrate with the Ca^{2+}.

As crude oil compositions are highly variable, particularly with regard to their heavier, more polar species, the adsorption/deposition behaviour of the Minnelusa crude studied here cannot be expected to be universal. However, it is anticipated to be reasonably representative of asphaltic crude oils with high base number and lower acid number. Further, deviations from the trends for Minnelusa crude should be able to be traced back to differences in the zeta potential of the oil emulsified in the salt solution of interest.

4.3.4 Consequences for contact angle

While the amount and distribution of asphaltene deposition on the kaolinite substrates dictates their wettability, measurement of oil drop contact angles on these substrates in aqueous phase is required to quantify the dependence. Following literature procedures (44; 56; 57; 62), decane (incapable of dissolving asphaltene) and pure water were used as the two model phases in measurements of receding and advancing angles (through the surrounding water) on oil drop growth and retraction, respectively. Thirteen brine/oil-treated pieces, for salt solutions spanning a range of deposition in Figure 4.3, were analysed, plus an untreated control piece. Receding contact angle varies little, with average and standard deviation of 37.6±4.3°. Figure 4.7 plots the average hysteresis, i.e.

difference between advancing and receding angles (with standard deviation as error bar), for the 14 pieces against their deposition mass per planar area. As expected, hysteresis is practically absent from the clean hydrophilic control, and generally increases with deposition to a plateau around 40°. All samples with deposition above 17 mg/m^2 behave almost identically, while values below 5 mg/m^2 are required for angle hysteresis to be substantially less. All samples with low deposition and low angle hysteresis correspond to solutions with either 1M $CaCl_2$ or pH 9, both of which can limit deposition to the upper face (Figure 4.4). In such cases, the bulk and surface pores of the kaolinite coat presumably remain water-filled, and partial anchoring of the decane drop to isolated uppermost faces is insufficient to instil much adhesion. The data point in Figure 4.7 having low deposition but high hysteresis is for 1M NaCl without calcium, with deposition mainly on edges, as in Figure 4.4c. Although it apparently presents the most hydrophilic upper faces, persistence of edge deposition below the top layer provides paths for decane to penetrate into the aggregate to strengthen its adhesion.

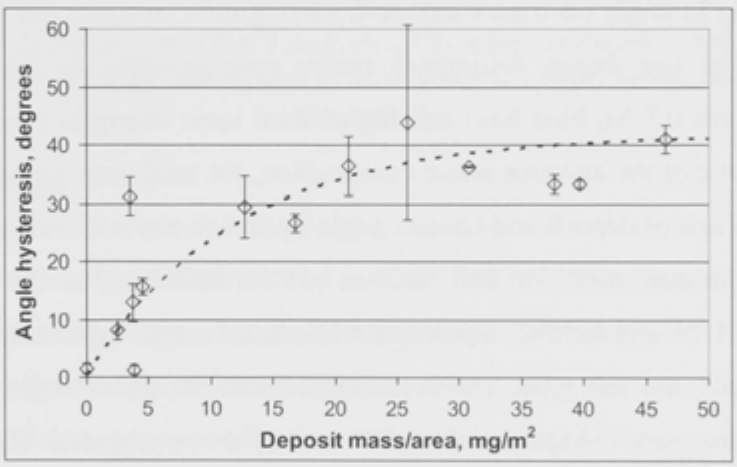

Figure 4.7. *Contact angle hysteresis of a decane drop in pure water on brine/oil-treated kaolinite coats versus their asphaltene deposit amount. The dotted curve is a simple exponential fit.*

Direct comparison of these contact angle results to literature studies on smooth impervious substrates, e.g. quartz, mica and glass, is difficult due to differences in crude oils and brines, and procedures for aging, solvent rinsing and decane/water contact angle measurement. A Wilhelmy plate study (86) of quartz aged in Minnelusa crude reports water-receding and -advancing contact angles larger than ours. Indeed, the maximum advancing angle of around 80° at the plateau in Figure 4.7 might suggest that

these kaolinite substrates are only weakly oil-wet, which is at odds with their substantial deposits evidenced by spectroscopy and FESEM. This apparent inconsistency is due to the procedure for measuring contact angle using a decane drop on the water-immersed substrate. Displacement of water by decane along tight, oil-wet pathways between kaolinite particles during the relatively brief time in contact cannot reproduce the same extent of penetration of crude oil (which created these deposits) during the prolonged aging, thus contact angle is underestimated. For smooth non-porous substrates, similar contact angles are usually obtained irrespective of whether the brine/oil-treated substrate is immersed first in water or decane (86). In our case, the contact angle of a water drop on a decane-immersed kaolinite substrate would presumably yield an overestimate of the true advancing angle.

Figure 4.8 compares the contact angle hysteresis after short-term contact of crude oil with the kaolinite-coated substrates from Chapter 3.3.2 (Figures 3.10b and 3.12) with the amount of asphaltenic deposits extracted from the kaolinite-coated substrates after long-term aging in crude oil from Chapter 4.3.2 (Figure 4.3a-b), in the presence of the same brine. The two boxes distinguish points corresponding to lower total ionic strengths (at most 0.1 M, blue box) and higher total ionic strengths (above 0.1 M, red box). Irrespective of the aqueous phase composition, for total ionic strengths above 0.1 M both the amount of deposit and contact angle hysteresis are relatively small (with the exception of the one point for 1M NaCl at pH 9). However, as the ionic strength decreases to 0.1 M and below, deposition and contact angle hysteresis become more dependent on pH and salt type. The correlation between contact angle hysteresis and deposition is strongest and steepest for pH 4 and becomes progressively poorer as pH increases. At low pH conditions, the brine film ruptures very quickly, which leads to high short-term contact angle hysteresis and moderately high long-term deposition, probably limited by a significant amount of brine trapped under the rapidly collapsing oil interface. The more stable brine films at pH 6 give less short-term adhesion, but allow more surface chemical interactions to occur over time via cation/anion exchange or charge redistribution between oil and kaolinite, to more gradually expel water and build up deposits, of amount often exceeding those for pH 4. At pH 9 there is no correlation, in which case short-term adhesion tests would not be indicative of longer-term wettability alteration.

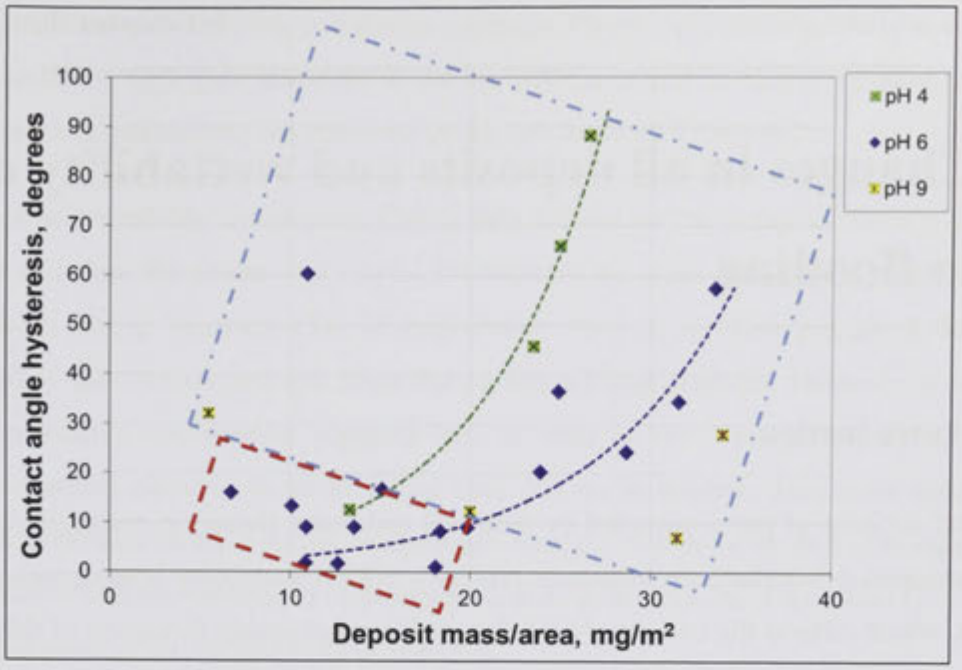

Figure 4.8. *Correlation between short-term contact angle hysteresis of crude oil on the kaolinite-coated substrates (from Chapter 3.3.2) with amount of asphaltenic deposit extracted from the kaolinite-coated substrates after long-term aging in crude oil (from Chapter 4.3.2) for the same NaCl and/or $CaCl_2$ brines at the three pH values. The dashed blue and red boxes correspond to brine ionic strengths below and above 0.1 M, respectively.*

4.4 Conclusion

Uniform, smooth coats, of thickness ~1 μm, of fine kaolinite on glass were used to analyse adsorption/deposition of crude oil components in the presence of water, relevant to oil recovery from rock and contamination remediation. These coats of immobile kaolinite are well suited to quantification of asphaltene deposit amount by fluorescence spectroscopy, and facilitate high-resolution microscopy of deposit distribution. Ingress of oil into kaolinite aggregates, by rupture of water thin films to render particles oil-wetting and so eject water from inter-particle pores, is the norm for most sodium and calcium chloride solutions investigated. Increase in concentration of either salt generally reduces overall deposition, with high sodium chloride content serving to predominantly limit deposition to kaolinite edges, while high calcium chloride salinity protects both faces and edges. The latter scenario can better preserve the water-wettability of the kaolinite aggregate, even if the outermost particles bear deposit, as it limits the ability of oil to interlock with the aggregate interior.

5 Changes in oil deposits and wettability due to flooding

5.1 Introduction

Mineral surfaces of pores occupied by crude oil and water (brine) in reservoir rocks or contaminated sub-surface environments typically exhibit wettability heterogeneity at all scales, which reflects the history of oil-brine-rock contact during formation of this state. On contact of crude oil with water, its polar molecules (asphaltenes and resins) will naturally begin to migrate to the oil-water interface. Experiments on model oils suggest that this migration leads to the build-up of a monolayer of asphaltene-resin aggregates (95). Langmuir-Blodgett monolayers were shown via AFM to give a rigid close packing of disks for pure asphaltenes, whereas resins change the film to a more compressible, open structure (96). Interfacial rheology of oscillating crude oil drops in water confirmed that the films are primarily elastic, with increasing asphaltene content increasing both elasticity and aging time required for full development of the network (90). The development of the oil-water interface occurs concurrently with the drainage of the originally water-filled pores by the accumulating oil. The capillary pressure (and thus meniscus curvature) and water-receding contact angle determine the pore wall subareas over which water is drained to a thin film (38). In these subareas, the disjoining pressure then dictates whether the thin film ruptures to allow the asphaltenes and resins to adsorb or deposit there to alter local wettability towards oil-wetness (66; 77; 78; 90). Over time, this deposition proceeds to thus define the developed wettability state of the reservoir or spill zone, i.e. its "initial" state prior to recovery or remediation.

The studies of model substrates such as quartz and mica, and their extensions in Chapters 3-4 to kaolinite, give insight into the initial wettability state of asphaltenic adsorption/deposition within these drained and aged subareas, and its consequences for contact angles. Even within such subareas, the analyses by AFM and FESEM typically reveal heterogeneous morphologies (58; 90; 96), i.e. so-called dalmation patterns of deposits separated by bare substrate. The gaps presumably correspond to aqueous nano-

drops and nano-networks trapped during drainage. These are especially likely to occur if the asphaltenic aggregate assembly at the oil-water interface is fully developed prior to its collapse en masse onto the substrate in this pre-fabricated form (90).

This initial wettability distribution (78) greatly influences the water-advancing contact angles and thus the extent and rate of oil removal by water flooding or spontaneous imbibition during recovery (38) or remediation (64). It is often presumed that the wettability distribution remains fixed during this oil displacement. However, evidence from core-scale experiments suggests that, at least in some systems, rock subareas altered towards oil-wetness in the initial state can revert towards their more water-wet pristine condition on oil removal. Such *in situ* changes in wettability during flooding are proposed to underpin enhanced recovery by lowering the salinity of the flood (27) or re-injecting some of the oil and re-flooding (97).

Some studies (59; 87) have succeeded in adapting AFM and surface forces apparatus (SFA) to measure surface force profiles versus separation in crude oil-brine-mineral systems, to provide insight into the molecular-scale mechanisms at play. As a mica substrate in salt solution approaches a pre-deposited asphaltenic layer, it experiences non-DLVO repulsions due to long-range diffuse, polymer-mediated forces and short-range hydration forces. On separation from contact, attraction due to short-range acid-base interactions is mediated by polymer bridging (59). Significantly, brine flooding of oil-treated mica led to partial or complete removal of the adsorbate at sufficiently high salinity or pH (59), giving some support to the belief that wettability alteration can be reversed.

There is thus a need to extend the model substrate studies of the aged, initial wettability state to analyse any changes due to subsequent waterflooding, and similarly assess their dependence on aqueous conditions. However, in doing so it is necessary to address one shortcoming of almost all of these above-mentioned studies. As mentioned in Section 4.1, the oil-aged substrate is typically rinsed with organic solvents to remove the bulk oil, and sometimes also dried, prior to analysis of the deposits by contact angle, AFM, FESEM or SFA. It is likely that the artificial rinsing/drying steps perturb the amount and/or nanoscale morphology of deposits, in particular depending on the solvency. As one example, contact angles and AFM thickness and roughness of deposits rose on oil rinsing with the increasingly poorer solvents toluene, decalin and cyclohexane (89). The studies in Chapters 3-4 removed the crude oil by rinsing with decalin followed by

heptane (98), similar to the procedure for preparing the so-called mixed-wet-film state in rock cores. This same solvent sequence was also used in related studies of the initial wettability state in glass bead packs (78) and the state after flooding in sandstones (99).

Preparations of model substrates in the flooded state should not employ such solvent rinsing steps prior to waterflooding, as oil should remain in its native bulk state during displacement to mimic its recovery from reservoirs. Indeed, the few existing preliminary studies (58; 90) of flooded model substrates suggest that solvent rinsing is not necessary after waterflooding, since the vast majority of bulk oil is removed by the flood. However, fair comparison of deposits remaining after flooding with those present in the initial state, in which solvent rinsing is necessary prior to inspection, demands that rinsing effects be investigated.

To this end, the studies in Chapter 5 return to a smooth model substrate (glass), on which the nanoscale morphology and coverage of asphaltenic deposits in the initial wettability state, and any reversal of this wettability alteration on flooding, are analysed. Four brine compositions are investigated, along with four preparation procedures that involve varying sequences of waterflooding, solvent rinsing (again focusing on decalin and heptane) and drying. FESEM images are compared to AFM and contact angle measurements, and to corresponding images of a sandstone rock.

5.2 Materials and methods

5.2.1 Materials

The crude oil (Minnelusa) was identical to that described in Chapter 3.2.2 and used in Chapters 3-4. The salt solutions used were a subset of those in Chapters 3-4, in particular containing only NaCl at the two concentrations of 0.01 M and 1 M, with pH adjusted to 4.0±0.1 or 9.0±0.2 by adding HCl or NaOH. Zeta potential of the crude oil in these four solutions is again given in Table 3.2 and Figure 3.2a. The model substrate was microscope glass slide (Knittel Gläser), cut into small rectangular pieces (~8x17 mm^2) and pre-cleaned with ethanol, 10% NaOH, and water, then treated in a RF water-vapour plasma unit (50 W for 1 min.). Two experiments used as more realistic substrate a quartz-based sandstone with 3% clay, porosity 11% and median pore diameter 13 μm. Slabs (7x20 mm^2, 2 mm thick) were cleaned with methanol, 50/50 methanol/toluene and toluene, and then dried at 60 °C and plasma treated as above. Organic solvents used were decalin, n-heptane and cleaned n-decane (see Chapter 4.2.1).

5.2.2 Treatment of substrates with oil and salt solutions

An experimental protocol (Figure 5.1) was developed for treating the glass substrates in various ways to simulate oil recovery and to test the effect of organic solvents subsequently used to remove the oil and salt solution for assessment of the underlying wettability state. The first three steps (1-3), common to all procedures, simulate creation of the reservoir and establishment of its initial wettability state. The substrate piece was equilibrated for 1 h. with the degassed salt solution (3.5 ml) in its sealed vial (step 1), then 2 ml of the solution was withdrawn using a pipette, so that the water level just covered the substrate, and replaced with a similar volume of crude oil (step 2). Light vacuum was applied, followed by equilibration for at least 1 h. In step 3, the salt solution was withdrawn by pipette from the vial bottom, leaving a small amount at the bottom, to which the water film surrounding the oil-immersed substrate drains. Further drainage was achieved by centrifuging the vial at 110 g for 5 min., also serving to separate the oil and aqueous phases and flatten their meniscus. The sealed vial was then aged at 60 ^{o}C for 6 days. The aged substrates, simulating the state prior to recovery, were then treated in one of four ways (procedures A-D in Figure 5.1).

Procedure A attempts to preserve this initial wettability state while removing the bulk oil and salt solution with organic solvents. The substrate was transferred to a vial of decalin, which dilutes the bulk oil but is a poor solvent for its (adsorbing) asphaltenes and resins in isolation. After 10 min., the substrate was switched to a second decalin bath for 2 h., which remained colourless. It was then transferred to a vial of n-heptane for 24 h., serving to further dissolve free maltenes, and afterwards to methanol for 24 h., to remove salt and water, and finally dried ambiently. This is very similar to the procedure used for the kaolinite-coated slides in Chapter 4.

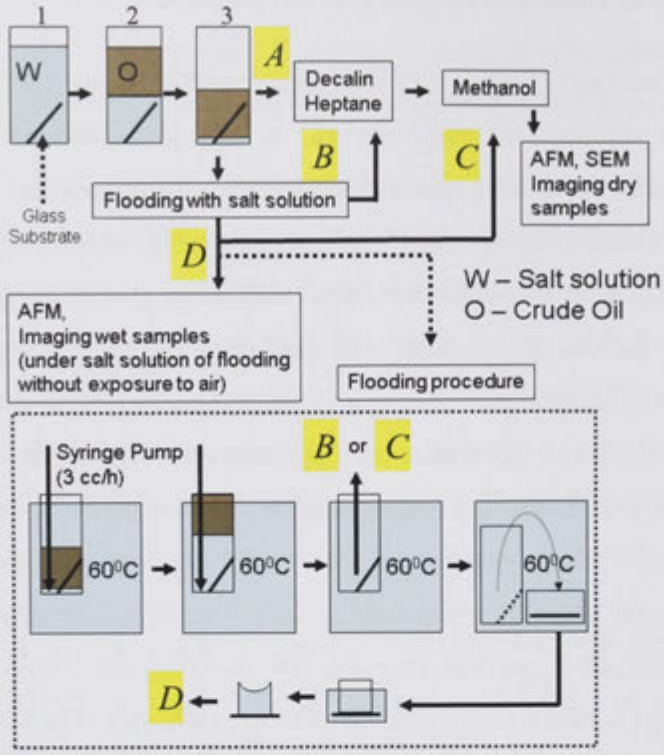

Figure 5.1. *Experimental protocol for treatment of the substrate with oil, salt solution and organic solvents. Following steps 1-3 of drainage by oil and aging, one of four procedures A-D was used for flooding with salt solution and/or rinsing with solvents to remove the bulk oil and salt solution. Centrifugation was used both in drainage step 3 and in flooding for procedures B-D.*

Procedure B employs the extra step of flooding the aged vial with salt solution (Figure 5.1), to simulate oil recovery, prior to the same solvent immersion series as for procedure A. After aging, the vial was held partly immersed in a water bath at 60 °C, and a syringe pump was used to inject the salt solution (of the same composition as in steps 1-3) through a pipette into the bottom of the vial at the fixed rate of 3 cm^3/h. Once the bulk oil had risen above the substrate, the vial was centrifuged at 1000 g for 10 min. to strip larger drops of bulk oil adhering to the substrate, after which the oil in the upper phase was removed and replaced with salt solution. The centrifugation and decantation were then repeated, and any oil remaining at the air interface was removed using lint-free tissue. The substrate was then taken from its vial to perform the decalin-heptane-methanol immersion and drying steps as for procedure A. Procedure C is identical to B, but omits the decalin-heptane immersion, so the substrate after flooding with salt solution, including centrifugation and oil removal, was transferred directly to methanol for 10 min., and then dried.

Procedure D also involves salt solution flooding, but omits the solvent immersion and

drying steps of B and C, so the substrate remains under its salt solution throughout the preparation and AFM imaging. The flooding is similar to that for B and C (Figure 5.1), although now with the 60 °C bath containing the salt solution itself. After flooding, centrifugation and removal of all oil at the air interface, the vial was submerged to the bottom of the bath, and its substrate was transferred (while submerged) with tweezers onto a Petri dish. The dish was lifted from the bath and a cylinder of clean plastic tubing (of length 4 mm, with outer and inner diameter 5 and 4 mm) was submerged to stand on top of the central area of the substrate. The salt solution retained in the tube by capillarity ensured that this central area remained submerged during substrate transfer to the fluid cell of the AFM stage. The cell's O-ring was placed on the wet area, after which it was filled with the same salt solution, without trapping air, and imaged at 23-24°C. For all procedures and salt solutions, three replicates were performed, and the upper side of the substrate (facing upwards in Figure 5.1) was always chosen for analysis.

For the rock slabs, experiments were performed in only one salt solution (0.01 M NaCl at pH 4) for only two procedures (B and C). The centrifugation at step 3 (Figure 5.1) was increased to 690 g for 10 min. to achieve substantial drainage of pores by oil. Centrifugation after salt solution flooding was increased to 1300 g for 10 min. (twice) to remove as much as possible of the oil trapped in pores. For procedure B, the decalin-immersed rock slab was similarly centrifuged, but five times rather than twice, and exchanged each time with fresh decalin until it remained colourless. The sample was then centrifuged once in heptane and then methanol.

5.2.3 Measurements of oil deposits on substrates

FESEM of oil deposits was performed as described in Chapter 3.2.3, although without the platinum coating for the rock samples. For AFM, a Nanoscope III (Digital Instruments) with high sensitivity Super A scanner was used in tapping mode at 0.89-1 Hz for imaging uncoated glass samples both in air and under salt solution, with the latter employing the special fluid cell mentioned above. For dry-state imaging, a cantilever (Tap300Al, BudgetSensors) with a resonance frequency of 300 kHz and a force constant of 40 N/m was used. Under salt solution, the cantilever (Multi75Al, BudgetSensors) had a resonance frequency of 75 kHz and a force constant of 3 N/m.

The two types of contact angle measurement described in Chapters 3.2.4 and 4.2.4 were

performed, i.e. for crude oil drop in salt solution on clean glass substrates, or a decane drop in water on substrates pre-treated with crude oil and salt solution according to the procedures in Chapter 5.2.2.

5.3 Results and discussion

5.3.1 Topography of oil deposits

The results show that morphology and amount of residual deposits on the glass substrates are strongly dependent on the salt solution composition and the solvent post-treatment. Procedures A and B, involving decalin-heptane rinsing, leave only the bound asphaltene/resin components, generally in the form of nanoparticles, while C and D leave bulk oil sheathed by these components, generally as nano-blobs. For the four salt solutions (i.e. the two NaCl concentrations each at two pH values) and four treatment procedures, the results below present representative FESEM and AFM images, together with metrics obtained from these. FESEM has the advantages of simpler, higher quality imaging of deposit textures with fewer imaging artifacts over larger areas, providing a fuller picture of the local wettability state. As deposits appear lighter than the glass background, they were segmented from the substrate by thresholding greyscale values using ImageJ software. Statistics of deposit coverage (as percentage of substrate area) and lateral size of particles (i.e. individual base area, identified using the ImageJ particle analyser tool) were thus quantified over the set of FESEM images for each sample. These measures were in good agreement with similar analyses of the AFM phase (amplitude) images. AFM has the unique advantages of providing deposit height information for all samples, as well as coverage and particle size from the less noisy phase images for wet samples (procedure D). AFM 2D height maps were analysed by ImageJ and Gwyddion software to calibrate greyscale value to height above the substrate, yielding the average thickness of deposit over the entire substrate (including covered and uncovered regions). From the presented values of average thickness, in nm, deposit mass per planar area, in mg/m^2, can be calculated via multiplication by deposit density (typically around 1.2 gcm^{-3} for asphaltene (46)).

For all 16 samples, Figure 5.2 compares the deposit coverage resulting from the four salt solutions and four procedures. Table 5.1 lists the corresponding thickness and particle area averages. Figures 5.3, 5.5 and 5.6 present FESEM and AFM images and metrics for some salt solutions using procedures A-C, and Figure 5.7 gives AFM images

for D.

Area coverage of the substrate by the oil deposits is the primary measure of its wettability alteration, and despite the quite large standard deviations (error bars) in Figure 5.2, the trends are clear. None of the 16 samples approaches the fully covered state of a complete film. For a given salt solution, coverage decreases from procedure A to B to C, and then rises somewhat to D. The coverage averages over all four salt solutions in Figure 5.2 are A: 70%, B: 47%, C: 10%, D: 27%. For a given procedure, coverage generally reduces from pH 4 to 9, and decreases from 0.01 to 1 M NaCl, although the distinction is less at the highest coverages (for A). The reduction in coverage from procedure A to B is due to the latter's extra step of salt solution flooding prior to the decalin-heptane post-rinsing common to both. Thus, some fraction of wettability alteration during immersion in crude oil can be reversed in situ during oil displacement by flooding. This reversal increases with pH and salinity, from a minimum of 13% decrease in coverage percentage units in Figure 5.2 for 0.01 M NaCl at pH 4 to a maximum of 36% decrease for 1 M NaCl at pH 9. These two salt solutions correspond to the strongest and weakest oil adhesion, respectively, as discussed at the end of Chapter 5.3.1.

The sizable reduction in coverage from procedure B to C, due to the latter's omission of decalin-heptane rinsing, suggests that this step to remove bulk oil artificially broadens deposit features. While C exhibits the same trends of decreasing deposition with increasing pH and salinity, the most oil-wet sample (for 0.01 M NaCl at pH 4) still only exhibits 20% coverage. Procedure D provides an even more realistic preservation of the state of deposition after flooding, however its large coefficients of variation in Figure 5.2 due to the limited number of usable AFM images acquired cast some doubt on the reliability of its trends, e.g. the surprisingly high coverage for 0.01 M NaCl at pH 9.

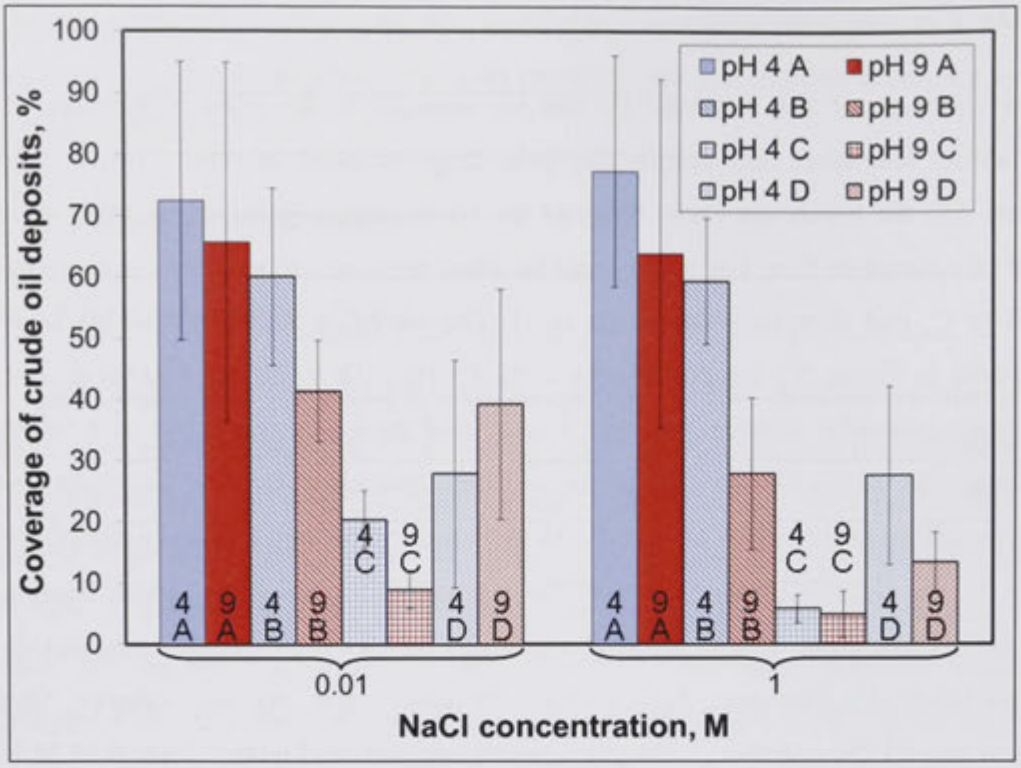

Figure 5.2. *Percentage area of glass substrate covered by crude oil deposits as a function of concentration and pH of the NaCl solution, and for the four post-aging treatment procedures A (no flooding; decalin-heptane-methanol rinsing), B (flooding; decalin-heptane-methanol rinsing), C (flooding; methanol rinsing) and D (flooding; no solvent rinsing). Coverages for A-C are calculated from FESEM images and D from AFM.*

Table 5.1. *Averages (with standard deviations) of deposit thickness from AFM images and particle area from FESEM or AFM images, for the four salt solutions and four treatment procedures A-D.*

pH	[NaCl] M	Thickness, nm				Particle area, 10^{-3} μm^2			
		A	B	C	D	A	B	C	D
4	0.01	26±14	19±6	61±22	34±13	4.2±2	13±10	18±15	18±15
4	1	19±7	14±8	23±11	69±31	3.2±2	2.8±1	1.0±1	180±110
9	0.01	23±12	54±27	53±31	60±23	6.0±2	3.2±1	2.5±1	80±70
9	1	11±6	18±9	17±13	23±8	2.6±1	5.0±3	2.2±2	11±8

The statistics for thickness and particle area of all 16 samples are presented in Table 5.1. As it combines results for procedures which remove (A, B) or retain (C, D) bulk oil, neither particle area or thickness display a universal correlation to coverage in Figure 5.2. However, particle area displays a weak trend ($R^2 = 0.41$) of exponential increase with thickness. For procedures A and C, thickness in Table 5.1 exhibits the same

decrease with pH and salinity as coverage in Figure 5.2, although with larger thickness for C due to its retention of bulk oil in deposits. Surprisingly, the flooded and decalin-heptane post-rinsed samples for procedure B at pH 9 give greater thickness than A, and on par with C. Note that thickness values for A are of similar magnitude to literature AFM studies of solvent-rinsed initial wettability states on mica, for systems in which neither the crude oil nor the solvent induces asphaltene precipitation (44; 58; 74; 88; 89).

Procedure A

Figure 5.3 displays FESEM and AFM images corresponding to the two low salinity solutions and using procedure A, yielding high coverage. In both FESEM and AFM, the deposits appear as asphaltene-rich, partially connected nanoparticle clusters, qualitatively similar to literature images for related systems (58; 89; 65). Uncovered gaps between clusters were presumably occupied by nano-domains or nano-networks of water trapped during deposition. Larger empty circles in Figure 5.3a and c correspond to micro-lenses of trapped water, thus the dalmation pattern of water patches (90) occurs on two length scales. These sporadic ring features were not included in the coverage analysis. The faint texture within the rings is due to the platinum coat, and is readily distinguishable from the oil deposit in image analysis. The substantial deposition at the ring periphery probably originated from the asphaltene/resin adsorbed at the oil-water lens interface, subsequently deposited on the substrate during either the switch to the poor solvents decalin and heptane, or expansion of the lens and retraction of the heptane on methanol immersion. The likely changes in distribution of liquids and adsorbed/deposited material during the steps in procedure A are thus as illustrated in the left hand column of Figure 5.4, with the extraneous peripheral deposit indicated by the stacks of shorter line segments. It is also conceivable that the above-mentioned uncovered nano-domains were somewhat more prevalent prior to decalin-heptane exposure, as preferential loss of resins can lead to a less open deposit structure (96).

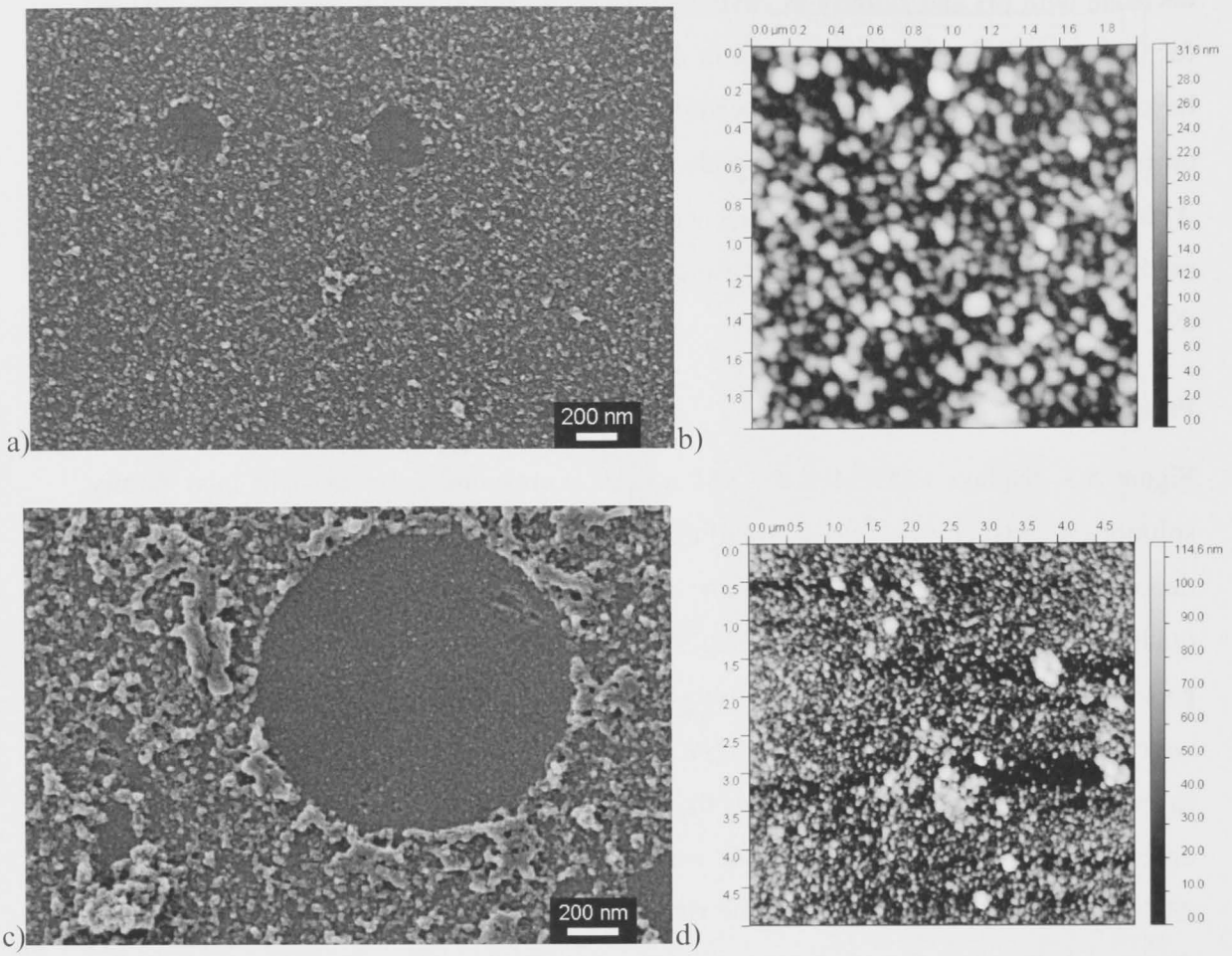

Figure 5.3. *Glass substrates treated according to procedure A with crude oil and 0.01 M NaCl, showing FESEM images for a) pH 4, c) pH 9, and AFM height images for b) pH 4 (2x2 μm^2), d) pH 9 (5x5 μm^2).*

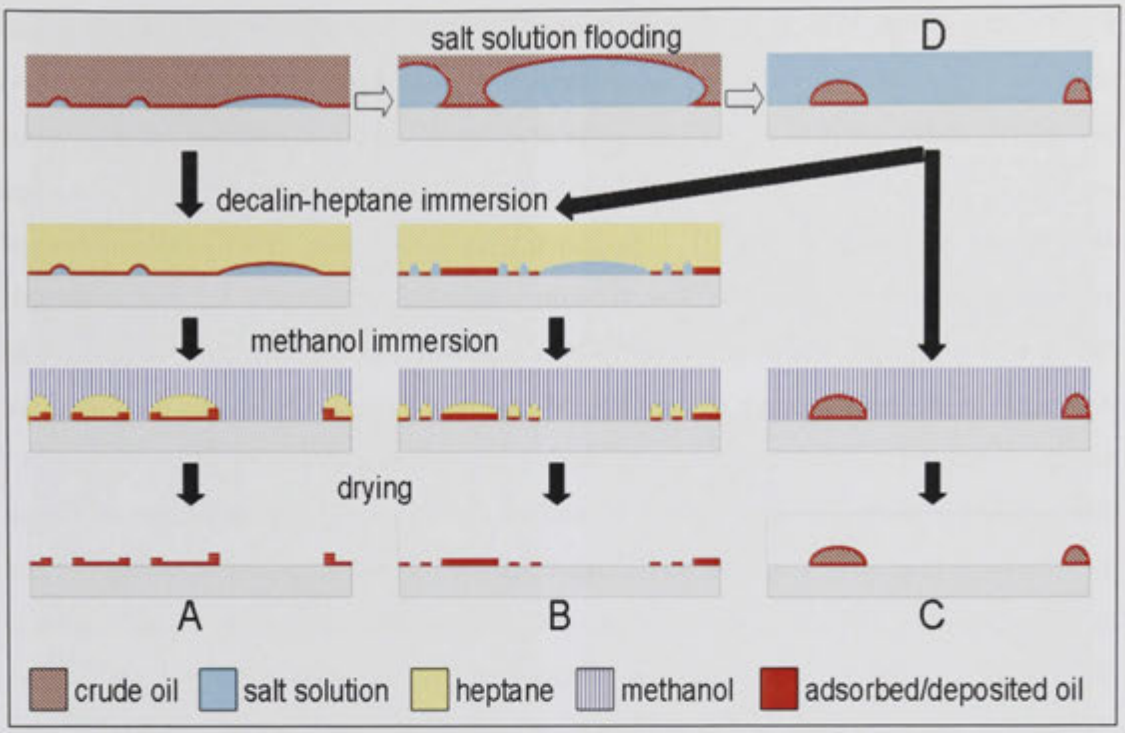

Figure 5.4. *Schematic of changes in location of liquids and adsorbed/deposited material, from the oil immersed, aged state of the substrate at the top left, due to the subsequent procedures A, B, C or D.*

Procedures B and C

Figure 5.5 provides FESEM micrographs of some samples after flooding with salt solution according to procedures B or C. For 0.01 M NaCl at pH 4, Figure 5.5a and b show the deposits from procedure B at higher and lower magnification, to be contrasted to the counterpart for A in Figure 5.3a. Figure 5.5a evidences the reduction in coverage and average thickness associated with the deposits accumulating into larger aggregates with barer substrate in between, consistent with Figure 5.2 and Table 5.1. Figure 5.5b displays the much larger and more frequent rings within which the substrate is cleaner. It appears that during salt solution flooding, the expansion of the residual water pockets and retraction of the oil causes a significant fraction of the deposits to be removed with the oil, while the remaining oil blobs become swollen by accepting retracted remnants, as illustrated in the top row of Figure 5.4. On subsequent decalin-heptane immersion, the deposits comprise both the oil blob asphaltene mounds and a scattering of surrounding asphaltene nanoparticles created by the inversion of aqueous and oleic phases (from oil-in-water to water-in-oil surface structures) and poor solvency of the asphaltene/resin-rich blobs in these solvents. Thus, coverage for B is overestimated, as illustrated in the middle column of Figure 5.4, where the extraneous deposit is indicated by the shorter, thinner line segments surrounding the thicker mounds.

Figure 5.5c and d show an analogous image pair from procedure C for this same salt solution. Omission of decalin-heptane immersion (the right hand column in Figure 5.4) avoids the above-mentioned aqueous-oleic phase inversion and creation of extraneous asphaltene deposits. Accordingly, Figure 5.5c is cleaner, with much lower coverage than Figure 5.5a, and naturally with greater thickness and blob size due to retention of resins and some bulk oil in their cores, again consistent with Figure 5.2 and Table 5.1. Some blobs appear hollow, presumably by evaporation of volatile core saturates and aromatics in the high vacuum of the FESEM chamber. Figure 5.5d shows the foam-like texture formed by surface oil retracting during salt solution flooding. Figure 5.5e and f for 0.01 and 1 M NaCl, both at pH 9, treated via procedure C, display further reduction in coverage, thickness and blob size (Figure 5.2 and Table 5.1), as increasing pH and salinity aids oil-glass repulsion across the salt solution during flooding (as discussed at the end of Chapter 5.3.1). For C, the metrics in Figure 5.2 and Table 5.1 are related. Figure 5.6 plots coverage and blob size for all FESEM images, showing a logarithmic correlation, as increasing repulsion reduces oil retention and accentuates its retraction from a foam-like form to snapped-off nano-blobs. Increased aging time in oil, observed to increase coverage by decreasing the frequency of trapped water pockets (90), may somewhat reduce the reversal of wettability alteration by limiting these initial points of water access.

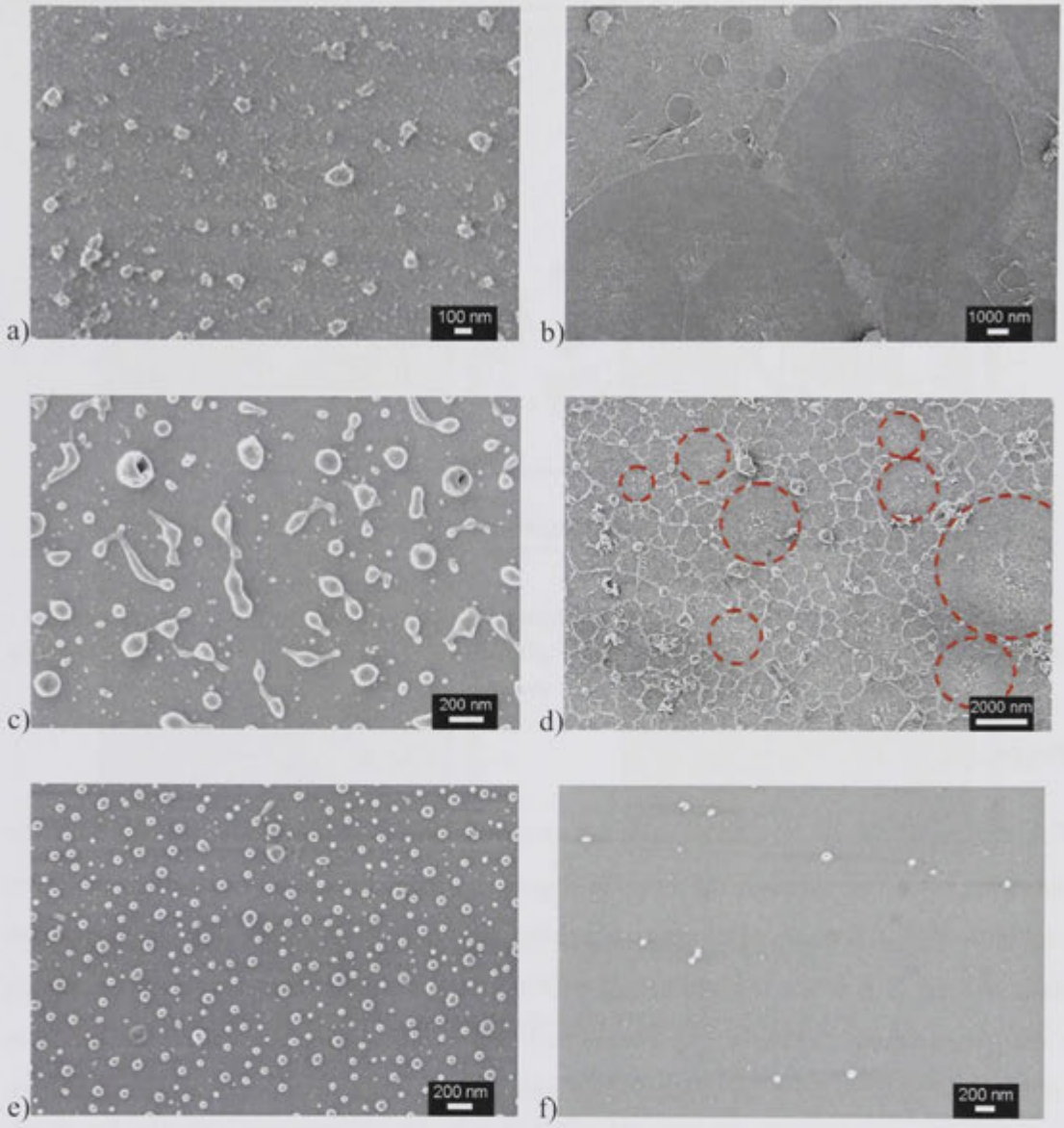

Figure 5.5. *FESEM images of glass substrates treated according to a-b) procedure B for 0.01 M NaCl at pH 4, or procedure C for c-d) 0.01 M NaCl at pH 4, e) 0.01 M NaCl at pH 9, f) 1 M NaCl at pH 9. Dashed contours on d) are formed from expanded water droplets.*

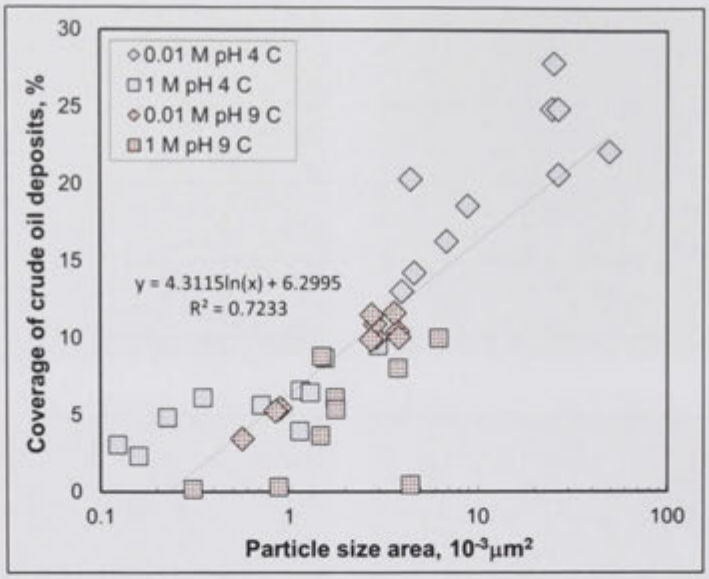

Figure 5.6. *Correlation between substrate coverage and average planar area of individual oil blobs using procedure C for all four salt solutions and all FESEM images for each.*

Procedure D

For procedure D, AFM images for the two salt solutions at pH 4, under which the substrate remained through the steps in Figure 5.1 from flooding to imaging, are given in Figure 5.7. All such AFM images exhibit artefacts, most noticeably the horizontal dark streaks, due to the tip interacting with the oil, and substrate movement caused by O-ring movement. However, the images suffice to confirm that residual oil has the form of nano-blobs separated by apparently clean substrate, i.e. a sparse dalmatian pattern qualitatively similar to the FESEM images of C (compare Figures 5.5c-d and 5.7a-b), and also similar to literature AFM images on mica (90). This suggests that the methanol immersion and drying in procedure C do not significantly alter the form or distribution of residues, and thus C is the best approach for dry preservation of the wettability state post-flooding for imaging using simpler techniques such as FESEM. From Figure 5.2 and Table 5.1, the coverage, thickness and blob size generally decrease from procedure D to C. While some decrease in all three measures could be expected from loss of volatiles within blobs at high vacuum, it is also likely that an insufficient number of AFM images were acquired to statistically represent the oil residues over the entire substrate. Without the use of decalin rinsing, each substrate piece exhibits some local variability in oil retained, in particular with occasional macro-drops. A high-throughput imaging technique such as FESEM is thus required to provide a representative topographic sampling.

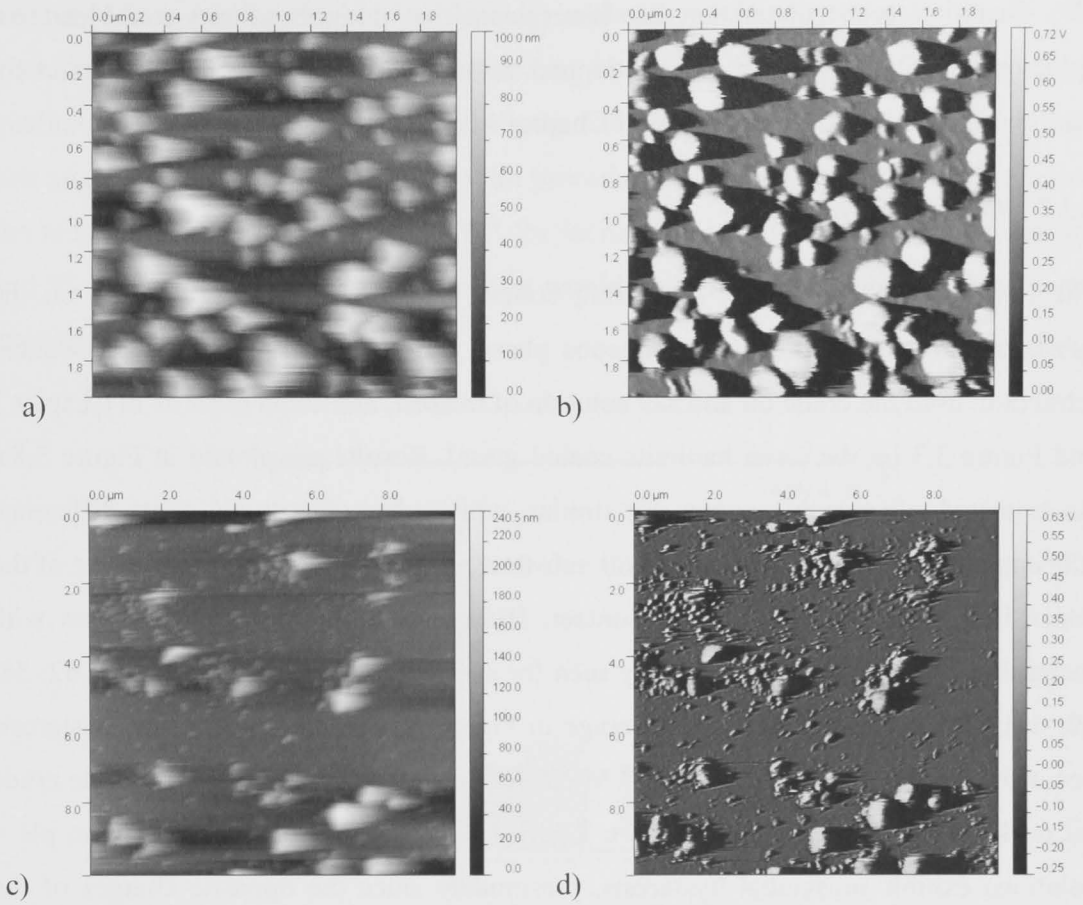

Figure 5.7. *Wet AFM images of glass substrates treated according to procedure D for 0.01 M NaCl at pH 4, showing a) height and b) amplitude (2x2 μm^2), or for 1 M NaCl at pH 4, showing c) height and d) amplitude (10x10 μm^2).*

The salt dependence observed for all four procedures is in line with literature studies on crude oil-silicate systems (38; 64; 44; 62; 87; 58; 59; 86; 65; 98). As discussed in Chapters 3-4, the lower pH is close to the isoelectric point of the Minnelusa crude-salt solution interface. Although its zeta potential values in Figure 3.2a are slightly net negative (-7.1 and -9.8 mV for 0.01 and 1 M NaCl, both at pH 4), the substantial population of protonated base polar groups adsorbed at this interface attract and transfer to bond to the negatively charged glass-salt solution interface, yielding relatively strong oil-glass adhesion. At pH 9, the oil interface is dominated by deprotonated acid groups (zeta potential is -78.9 and -16.0 mV for 0.01 and 1 M NaCl in Figure 3.2a), hence the water film separating the two negatively charged interfaces is more stable and adhesion is weaker. These effects are naturally strongest at the lower salinity in which the electrostatic interactions are less screened and thus longer ranged. Note though that in the case of pH 4 for procedure A in Figure 5.2, the coverage is slightly greater at higher salinity, as was also observed for the same oil on similarly prepared silicate substrates

(78). There it was speculated that the slower deposition at higher salinity could lead to a tighter packing of deposit with less trapped water, similar to the effect discussed for kaolinite-coated substrate at the end of Chapter 4.3.4.

5.3.2 Contact angle

The first type of experiment measuring contact angle of a captive oil drop on the substrate through the immersing aqueous phase, during drop growth and subsequent retraction, used the crude oil and salt solution of interest, and clean glass as in Chapter 3 and Figure 3.3 on the clean kaolinite-coated glass). Results are plotted in Figure 5.8a. As expected, all receding angles are similar, while advancing angle, or its difference (the angle hysteresis), is sensitive to oil-substrate adhesion established by rupture of the water film during the 30 min. in contact. Hysteresis in Figure 5.8a decreases with increasing pH and salinity, as usually seen for such measurements (38; 64; 44; 62; 58; 59; 61), and as was the case for coverage in Figure 5.2. Highest and lowest hysteresis occur for 0.01 M NaCl at pH 4 and 1 M NaCl at pH 9, as observed for the same crude oil on kaolinite-coated glass in Figure 3.10b. However, in Figure 5.8a only the pH 4 solutions exhibit substantial hysteresis, presumably since the opposite charges of the bare interfaces rapidly develop adhesion, while salt solutions such as 0.01 M NaCl at pH 9 require longer time to approach the extent of wettability alteration seen in Chapter 5.3.1 (e.g. Figures 5.2 and 5.3).

The second type of contact angle experiment instead used the glass substrates from Chapter 5.3.1, i.e. after exposure to salt solution and crude oil during 6 days of aging, followed by flooding and/or organic solvent rinsing. On these pre-prepared deposit-bearing substrates, contact angle was measured using a decane drop in water to avoid further alteration of the wettability state (as in Chapter 4 on the deposit-bearing kaolinite-coated glass). Only substrates for procedures A and B (involving decalin-heptane-methanol rinsing) were tested, since those for C and D bear residual bulk crude oil (as nano-, micro- and occasional macro-blobs), which would mix with decane and precipitate asphaltenes. Although B overestimated deposit coverage (Figure 5.2), its dependence on NaCl concentration, pH and flooding is similar to C. Both the receding (decane growth) and the larger advancing (decane retraction) angles in Figure 5.8b vary in response to the pre-imposed wettability state, and the two angles are reasonably well correlated. Aside from the substrate with least deposit (1 M NaCl at pH 9 for B), all advancing angles exceed 90°, and on the basis of contact angle can thus be classified as

oil-wet, but to varying extent. Advancing, and also receding, angles in Figure 5.8b generally decrease with increase in salinity or pH or with flooding (i.e. from A to B), in qualitative agreement with coverage in Figure 5.2. The one exception is the surprisingly low angles for 0.01 M NaCl at pH 4 with procedure A. On averaging over all samples, the reduction in advancing angle is 17° for increasing salinity, 12° for increasing pH, and 7° for flooding, although these values would be much greater on omission of this exceptional point.

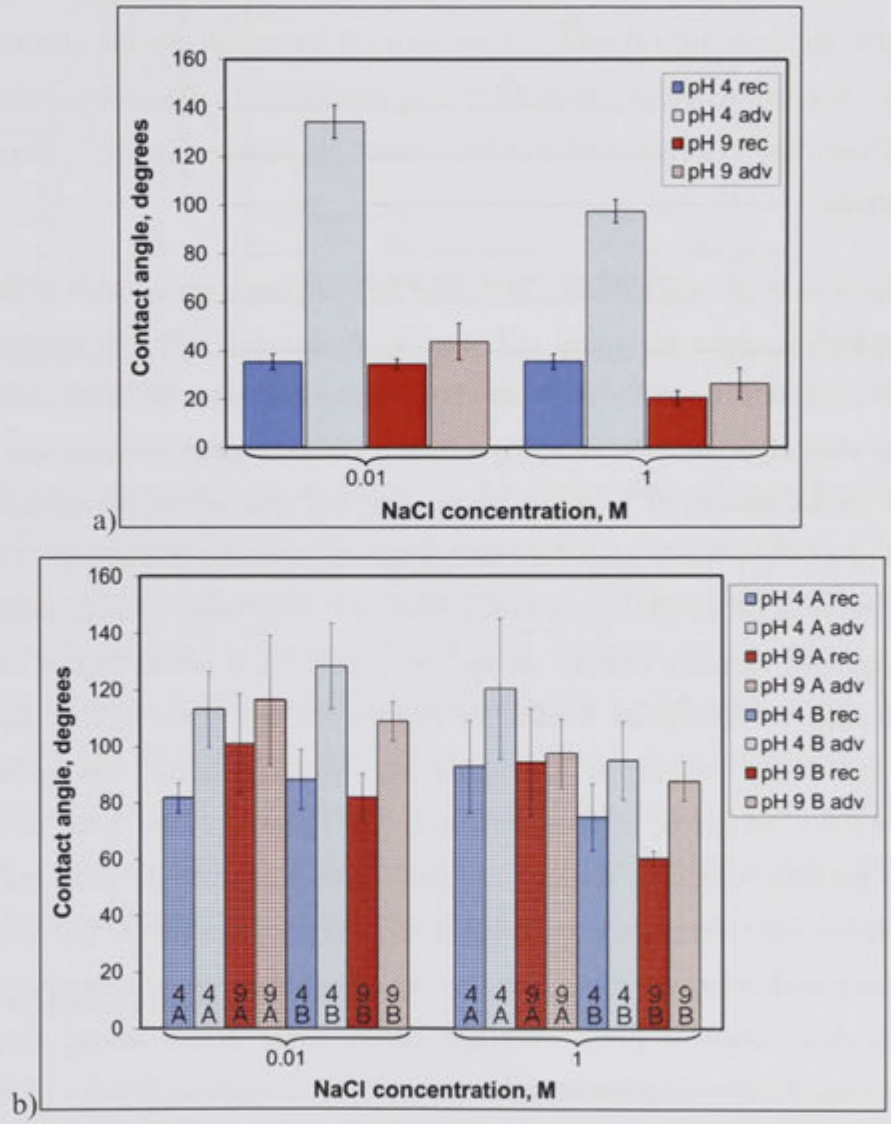

Figure 5.8. *Receding and advancing angles of a) crude oil on clean glass in the four NaCl solutions of various concentration and pH, and b) decane in water on glass bearing oil deposits from treatment via procedure A (no flooding; decalin-heptane-methanol rinsing) or B (flooding; decalin-heptane-methanol rinsing) using the crude oil and the four salt solutions. Error bars give standard deviations.*

The reduction in advancing angle due to flooding contrasts literature results (86) for quartz treated using the same Minnelusa crude oil and 0.1 M NaCl at natural pH (intermediate to our brine matrix) with a procedure similar to A, but rinsing off bulk oil with toluene. Repeated cycling of the treated quartz through the decane-brine interface in Wilhelmy plate experiments showed no decrease in receding or advancing angles from the first cycle, as was also the case for all tested crude oils with substantial asphaltene content and high base number (86). This lack of reversal of wettability alteration could be due to the insufficient shear stress of contact angle measurement, compared to the centrifugal flooding of procedure B. Moreover, rinsing of the crude oil prior to the flooding action of interfacial cycling eliminates the thermodynamic drive for the asphaltenic film to be removed with the stripped oil, as decane is a very poor solvent for asphaltene.

Differences due to pH and flooding in Figure 5.8b are more accentuated at the higher salinity, which is closer to typical salinities in oil recovery (38). Differences due to salinity and pH are stronger for procedure B, as the second exposure to the salt solution allows the electrolyte dependence of deposition reversal to come into play and increase the scope for differentiation. In particular, flooding will tend to remove aggregates held only in a relatively shallow secondary energy minimum of the free energy (100; 101). At pH 4, reversal of wettability alteration from A to B is more limited, owing to the above-mentioned opposite charges on the two interfaces, however higher salinity is more amenable to desorption, evident in Figures 5.2 and 5.8b. This is due to the decrease in decay length of the attraction, yielding more weakly adsorbed asphaltene/resin. At pH 9, reversal is greater in Figures 5.2 and 5.8b, as the bare interfaces are both negatively charged and only capable of weak adhesion via van der Waals attraction and electrostatic attraction mediated by protons (64; 61) or sodium ions or slow macromolecular reconfiguration. Further, the greater water connectivity of their initial wettability state of lower coverage allows better access during flooding to displace oil and further reduce coverage.

Figure 5.9 plots advancing contact angle from Figure 5.8b versus coverage from Figure 5.2, and displays a fair correlation, given the uncertainties in both measures. However, the lower coverage after flooding (B) generally gives somewhat larger angles than expected from non-flooded (A) samples. Given that receding angle shows a better overall correlation to coverage ($R^2 = 0.53$), the larger advancing angles for B may be due to greater heterogeneity of coverage (e.g. as seen Figure 5.5b). As expected, both

angles display a stronger correlation to coverage than to deposit thickness or particle size in Table 5.1.

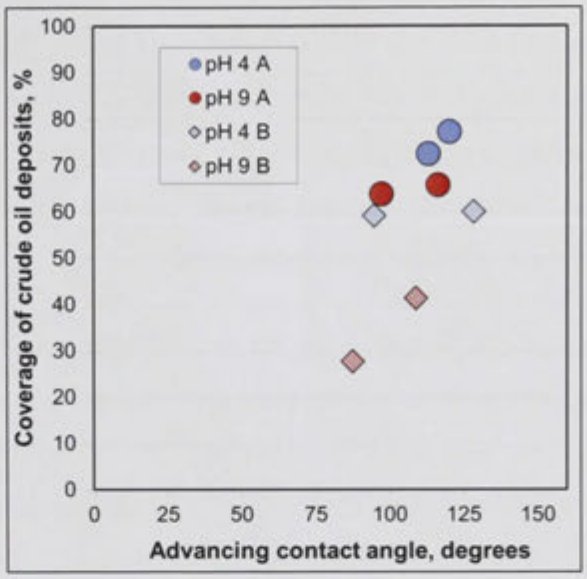

Figure 5.9. *Deposit coverage versus decane/water advancing angle for the eight glass substrates pre-treated with crude oil and the four salt solutions according to procedures A and B.*

Although no experiments were performed on the more realistically preserved substrates for procedure C, Figure 5.9 suggests that the substantially lower coverages in Figure 5.2 would yield oil/water advancing angles extending well below 90° into the water-wet regime. Combined with the results of Figure 5.8a, it appears that an initially oil-wet or mixed-wet reservoir would switch towards water-wet on advance of the flood, and remain so if pH is relatively high. Lower pH would both somewhat reduce the magnitude of this shift and increase temporal fluctuations in local wettability, as upstream oil slowly entering a flooded pore could reinstate oil-wetness prior to its displacement and re-shift towards water-wetness.

5.3.3 Oil deposits on rock

Drainage by oil and subsequent flooding by water naturally give rise to more complex interfacial configurations in rock pores than on a glass slide. On immersion of the originally salt-solution-saturated rock in oil and centrifugal drainage to establish high initial oil saturation, oil displaces bulk water from all but the tightest confines in pores, where concave menisci remain stable. The exposed pore walls are altered towards oil-wetness by adsorption/deposition of asphaltene and resin during aging. On salt solution flooding by immersion and centrifugation, the water menisci expand and advance over

pore walls to partially expel oil. As mentioned in Chapter 5.2.2, two experiments were performed on small sandstone slabs to test whether the fine-scale features of wettability alteration and reversal observed on the model substrate are applicable to the internal surfaces of rock. The sandstone was treated comparably to the glass slides, for the two cases of 0.01 M NaCl at pH 4 for procedures B and C. FESEM images of rock surfaces in pores below the cut face were acquired, chiefly focusing on relatively smooth quartz grains or overgrowths (where the deposit texture is most apparent). Representative images are given in Figures 5.10 and 5.11 for B and C.

In the bottom two images of Figure 5.10, for procedure B, the bright strips running along crevices or junctions between quartz grains correspond to confines retaining bulk water after drainage. The bulk water protects the quartz surfaces in these confines against deposition from the crude oil. The remainder of the surfaces in Figure 5.10 bear deposit (now darker), although with frequent micron-sized holes. These holes are presumably mainly created during flooding, by the sweeping water menisci and/or expansion of water micro-droplets trapped under oil on the rock surface. The highest magnification image (top right) in Figure 5.10 shows the nano-texture of deposits and fine channels connecting these holes. The texture is qualitatively similar to the corresponding image on glass (Figure 5.5b).

The analogous images for procedure C in Figure 5.11 display a quite sparse scattering of residual oil nano-blobs on otherwise apparently clean quartz surfaces, again qualitatively in line with the equivalent experiment on glass (Figure 5.5 c-d). This provides direct evidence that substantial reversal of wettability alteration towards water-wetness can occur during oil recovery by flooding, even for the chosen low salinity/low pH salt solution that is most favourable for oil-rock adhesion. Clearly, B leads to a considerable overestimate of coverage after flooding, both on glass and sandstone substrates.

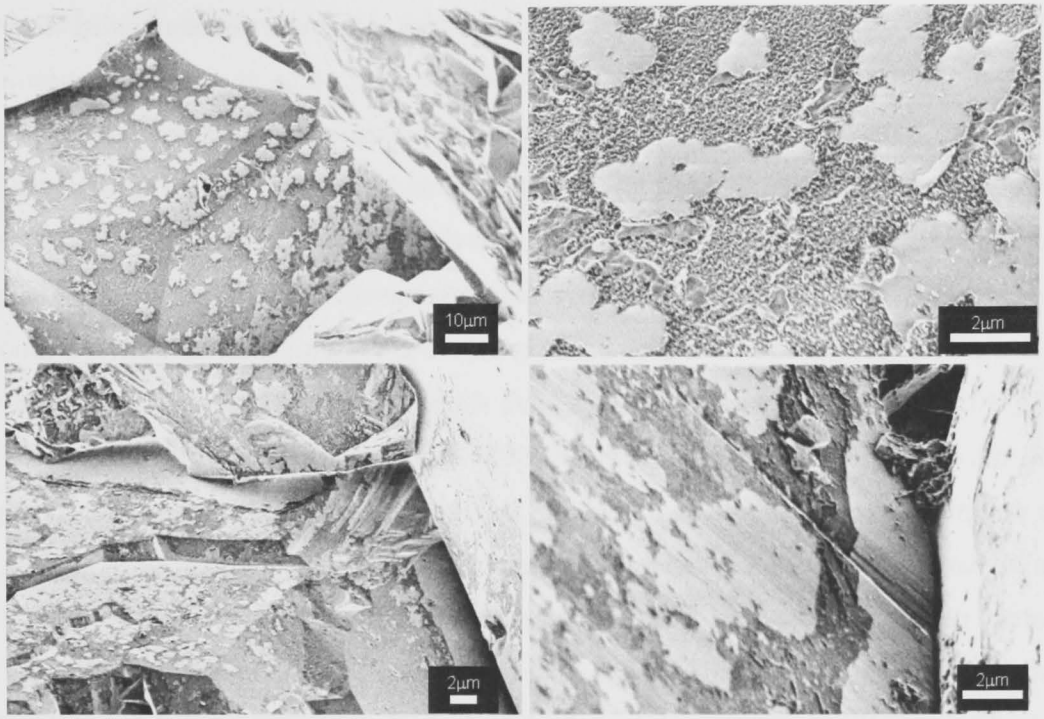

Figure 5.10. *FESEM images of sandstone rock treated in crude oil and 0.01 M NaCl at pH 4 according to procedure B.*

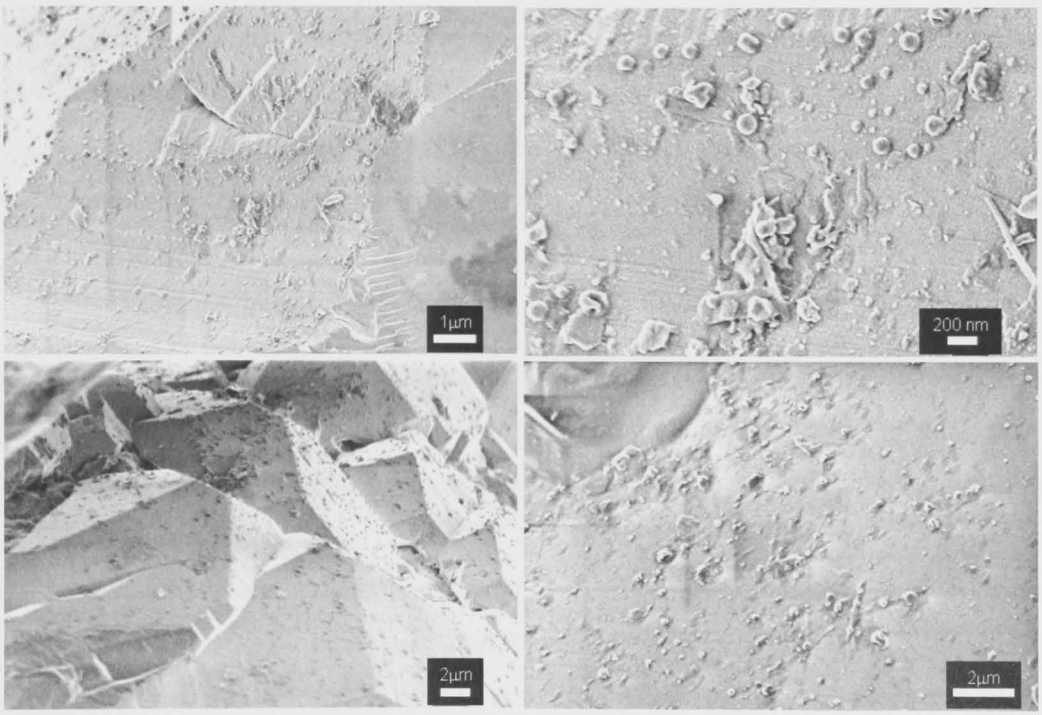

Figure 5.11. *FESEM images of sandstone rock treated in crude oil and 0.01 M NaCl at pH 4 according to procedure C.*

In applying the FESEM imaging technique to a rock, it can be recommended that for crude oil-continuous states, such as after drainage and aging, the wettability is well captured by procedure A (i.e. involving decalin-heptane rinsing), especially for delineating the boundary between water-protected and exposed regions (78). For water-continuous states, e.g. after flooding of an oil reservoir, the wettability is best represented by procedure C (omitting decalin-heptane rinsing). Numerical simulations of two-phase flow in the rock (i.e. its x-ray micro-CT digitisation or network model) (102; 103) from the initial drained/aged state should thus start by populating the pores with oil and water consistent with the FESEM-imaged boundaries from procedure A. On commencement of simulated flooding, the assignment of advancing contact angle can be based on its decane/water value measured on a flat planar substrate (e.g. glass or quartz) pre-treated according to this same procedure A (as in Figure 5.8b). For disconnected upstream oil subsequently moving into this flooded pore, the choice of its secondary receding contact angle can be based on the measured receding angle of a crude oil drop in this salt solution on the flat substrate treated according to procedure C (after removal of its residual oil macro-drops), or the similar procedure of Yang et al. (58). Depending on kinetics of re-establishment of a more oil-wet state under this newly arrived oil, as discussed in Chapter 5.3.2, the advancing angle of its later removal by continued flooding could be as high as the above-mentioned decane/water value for procedure A, or as low as the secondary advancing oil/brine value for procedure C.

5.4 Conclusion

Wettability alteration of glass caused by crude oil displacing the surrounding water (brine), and the reversal of this alteration via subsequent displacement of crude oil by flooding, was investigated as a function of concentration of NaCl in the aqueous phase and its pH. The morphology and amount of crude oil residues on the substrate is most conveniently analysed by FESEM in the dry state after removal of the non-adhering bulk liquid phases using organic solvents. Three such sample preparation procedures (A-C) were tested against a fourth procedure (D) in which the flooded substrate was maintained in its wet state and imaged by AFM. The three procedures consistently showed that wettability alteration towards oil-wetness decreases, and its flooding-induced reversal to water-wetness increases, with rising salinity and pH, in line with expectations from the interfacial electrostatic interactions. However, the procedure (B) removing bulk crude oil from the flooded state using the solvents decalin and heptane

underestimated the reversal by adding to the true deposition. The procedure (C) omitting these two solvents best preserved the wettability in the flooded state and demonstrated that reversal is substantial, even for salt solutions conducive to deposition (e.g. at low salinity and low pH). Deposit coverage from FESEM was reasonably well correlated to both receding and advancing contact angles on these treated glass substrates, and to FESEM images of deposition on sandstone rock.

6 Effect of wettability on crude oil displacement in 3D analysed by micro-CT

6.1 Introduction

Improved or enhanced oil recovery demands the continued development of viable waterflooding strategies to reduce residual oil during secondary recovery or recover this residual in tertiary mode. More systematic and predictive approaches to optimisation require further advances in our current foundational knowledge of the microscopic capillarity sub-processes of oil displacement and trapping.

A substantial body of research into waterflooding and residual oil at the pore scale has been performed on porous media such as bead and grain packs and 2D etched glass micromodels (104; 105; 106; 107). The vast majority of these results pertain to media of uniform, fixed wettability, usually water-wet. On primary drainage by oil, the irreducible water occupies the smaller pores and sheathes pore walls. On subsequent imbibition of water to displace oil, capillary oil trapping can occur via bypassing and/or snap-off. The former is mainly dictated by the pore size distribution, with rapid spontaneous advance of water through smaller pore sub-networks bypassing connected oil in larger pore clusters. Snap-off is instead determined by the aspect ratio of pore body width to connecting pore throat width, with oil rupture in tight bridging throats leading to discrete residual blobs in bodies (104; 105; 106). If the ratio of viscous forces (capillary number) or gravitational forces (Bond number) to capillary forces exceeds a threshold, entrapment decreases and mobilisation of residuals becomes possible. Mobilisation onset correlates to capillary numbers $\sim 10^{-5}$ in water-wet sandstones (108), or 10^{-3} in unconsolidated water-wet bead packs (106).

Over the past decades, awareness has grown that most reservoirs are not water-wet. Instead, a mixed-wet state is often thought to exist, comprising relatively oil-wet pore wall subareas over which oil contacts and adheres, intermingled with unaltered subareas covered by the connate brine (109; 38; 110; 22). The insights from displacement in

uniformly-wet porous media were combined with this notion of local wettability alteration to create pore-scale numerical models of mixed-wet networks (77; 111; 112). The recent advances in micro-CT have made possible the 3D pore-scale imaging of outcrop and reservoir rock plugs (113; 32; 29), providing more realistic pore spaces for modelling. Progress has also been made in micro-CT imaging of immiscible fluid phases in rock pores, via the addition of x-ray attenuating contrast agents (114; 115). Imaging to date has focused on simple fluids and idealised wettability states. More realistic scenarios in which the aqueous phase is drained by crude oil and aged, followed by waterflooding and pore-scale analysis of residual crude, remain largely unexplored at the pore-scale.

Further development of mixed-wet modelling is in need of more quantitative and realistic estimates of the wettability distributions to be assigned to the given rock pore network, in order to compare predictions of oil recovery and residuals from waterflooding to corresponding micro-CT pore-scale images of the flooded rock plug. The recent progress in characterising wettability will aid these endeavours. As one example, reservoir sandstones often contain kaolinite distributed in a variety of ways (filling, spanning and/or lining pores). The presence of kaolinite can variably increase or decrease the overall oil-wetness inferred from core analysis, depending on its associated impact on absolute permeability and initial saturations (79; 110). The work in Chapters 3-4 extended the limited set of model substrates on which reliable contact angle measurements are attainable to include kaolinite coats. This allows kaolinite's inherent ability or inability to alter wettability (in the given oil and brine) to be determined and ascribed to kaolinite regions contacting oil in network models. Further, Chapter 5 demonstrated experimental procedures for monitoring changes in asphaltenic deposits and contact angles at various stages during flooding. Chapter 5 and related studies (78; 99) also used FESEM imaging to extend the mapping of deposit distributions from model substrates to pore walls in rock.

Chapter 6 unifies these recent advances, by micro-CT imaging the pore-scale distribution of residual crude oil in plugs after drainage, aging and flooding, and combining this with FESEM and contact angle analyses of the wettability of analogue substrates and pore walls. It proves convenient to use plugs of unconsolidated quartz sand packs, rather than consolidated sandstones. This allows the freedom to increase pore size to further improve micro-CT resolution, and to pre-apply a controlled distribution of kaolinite linings on the grains before pack assembly to test their effect on recovery and wettability. The influence of the flood salinity, including the effect of the

added contrasting salt, is also addressed.

6.2 Materials and methods

6.2.1 Materials

The porous media each comprised a sand pack, without or with kaolinite on grain surfaces, confined between glass frits. The quartz sand (F-30; Ottawa, IL; U.S. Silica) is composed of 99.8% silica as unground round grains, with 22.3% retained by sieve mesh 30 (600 μm) and cumulatively 92.5% by mesh 40 (425 μm). The kaolinite (KGa-1b) is the same as that used in Chapters 3-4. The frits (Robuglas) were 3 mm thick with pore size 250-500 μm. Sand and frits were cleaned with toluene, 50/50 (v/v) toluene/methanol, methanol and water. They were further cleaned by RF water-vapor plasma (at 50 W for 1 min.) directly prior to kaolinite coating of grains or assembly of the pack. Supporting experiments on model substrates used rectangular pieces (7x26 mm^2) of microscope glass slide (the same as in Chapter 5.2.1), pre-cleaned as above, without or with a ~0.5 μm thick kaolinite coat (applied via the method in Chapter 3.2.1, although now with a slightly lower coat thickness).

The choice of crude oil was different from that in Chapters 2-5. In particular, the crude oil was from the Tensleep formation, Wyoming, with density 0.8682 gcm^{-3} at 20 °C, viscosity 14.3 mPa.s at 25 °C, n-C_7 asphaltene content 3.2 wt%, and acid and base numbers 0.16 and 0.96 mg KOH/g (88). Sand pack experiments used two aqueous salt solutions: 0.075 M CsI (cesium iodide; Sigma-Aldrich) and a 0.75 M mix of 0.125 M CsI and 0.625 M NaCl (AnalaR). The CsI enhances the attenuation difference between aqueous phase and crude oil in micro-CT imaging (115), with 0.075 M being close to the minimum required to contrast the two liquids. Model substrate experiments used these two solutions plus pure NaCl solutions of these two total concentrations. All solutions were used at their natural, unadjusted pH (5.8±0.2).

6.2.2 Sand pack preparation and flow experiments

Kaolinite-coated sand was prepared by filtering 8 g of 1 wt% kaolinite suspension through a 7 g bed of sand, which was then dried at 60 °C for 2 h. The sand was flushed with 0.75 M NaCl to strip very loosely bound kaolinite, and similarly dried. The average kaolinite coat weight was 0.28 wt% relative to sand. FESEM images show that the coat is patchy, corresponding to the darker subareas in Figure 6.1a. Kaolinite is

strewn as isolated particles, monolayers and multilayers, with platelets generally parallel to the surface, together with disoriented aggregates and pre-existing booklets (Figure 6.1b-f).

The cylindrical sample holder of the micro-CT mountable flow cell had outer and inner diameter of 10 and 8 mm and length 27 mm, with transparent plastic walls. It was packed with ~1.8 g of sand (without or with kaolinite pre-coating) to a height of 21 mm between the 8 mm diameter frits at top and bottom. The column was compacted by tapping and the ends of the holder were screwed tight. The 0.75 M CsI/NaCl solution was injected at 57 cm^3/h using a syringe pump to saturate the pack. The cell was then dismantled and the holder was contacted with filter paper in a sealed vessel at 100% humidity to drain the salt solution from the sand and frits without evaporation. Drainage was continued until ~10 wt% of the original solution remained. The holder was reconnected to the cell and pump to inject 30 pore volumes (PV, with 1 PV $\approx$ 0.35 cm^3) of crude oil in one direction through the sample at 57 cm^3/h (corresponding to capillary number $Ca = 3x10^{-4}$) to displace the air. The cell was sealed and aged for 7 days at 60 ^oC, followed by micro-CT scanning (see Chapter 6.2.3) of this oil-drained, aged state. It was then waterflooded by injecting 25 PV of the high salinity (0.75 M CsI/NaCl) or low salinity (0.075 M CsI) solution in this same direction at 2.0 cm^3/h ($Ca = 5x10^{-7}$) for 3 h., while held at 60 ^oC. This "secondary" recovered state was then micro-CT scanned. For the kaolinite-coated sand, high salinity flooding was followed by low salinity flooding and a third scan of this "tertiary" recovered state. The wettability of the kaolinite-coated sand after flooding was analysed as outlined at the end of Chapter 6.2.4.

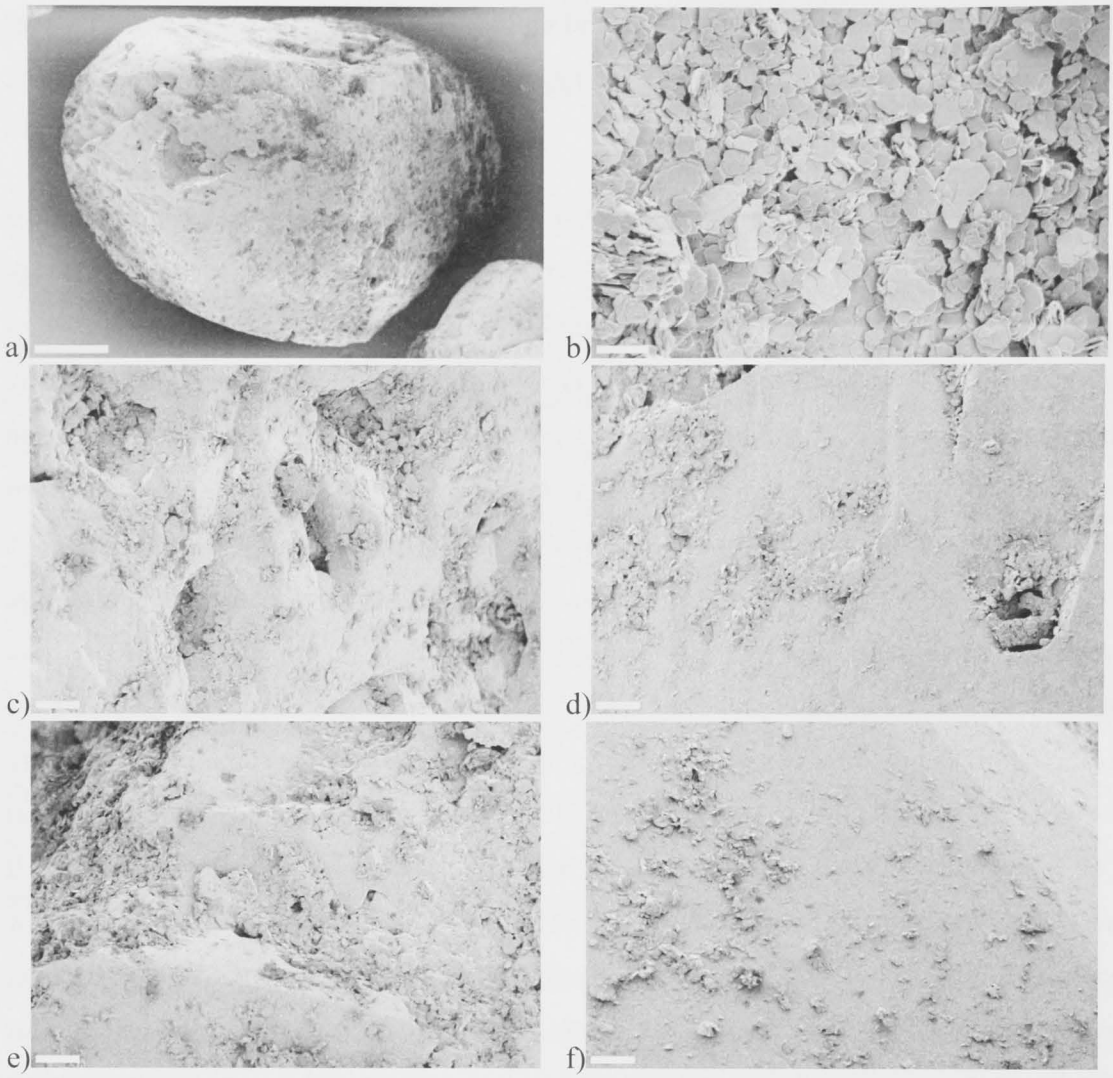

Figure 6.1. *FESEM images of a) a sand grain coated with kaolinite (scale bar 100 μm), b) a close-up within a grain subarea well coated by kaolinite (scale bar 1 μm), and c-f) four representative images at intermediate magnification (scale bars 5 μm).*

6.2.3 3D micro–CT scanning

Tomograms were obtained and analysed using the ANU micro-CT facility (29). After each of the steps in Chapter 6.2.2, the sealed flow cell was mounted in the micro-CT rotatable stage. The x-ray source was set to 80 kV and 100 mA, with filtered Bremsstrahlung used to acquire 2880 projections of 2048^2 pixels over 20 h. The projection set covered a 10.4 mm cube surrounding the centre of the sample, thus scanning its middle half to minimise the influence of any end effects. The projections were reconstructed to a 3D raw tomogram; with voxel size 5.5 μm. Tomograms were processed with Mango software, including anisotropic diffusion filtering, cropping of external walls, alignment and segmentation of the mineral, aqueous and oil phases (31; 32; 116).

6.2.4 Analysis of model systems

Zeta potential of crude oil (emulsified), quartz (finely ground F-30 sand) and kaolinite was measured in the four salt solutions with a Zetasizer Nano-ZS (Malvern Instruments), using the procedure described in Chapter 3.2.2. The ability of kaolinite particles to interfacially stabilise crude oil drops in the solutions was assessed by shaking and counting the macro-emulsion drops remaining 6 min. later, using a published procedure (99). The tendency for sand without or with lining kaolinite to alter its water-wet state towards oil-wetness during short-term crude oil exposure was tested by crude oil pendant drop experiments on the solution-immersed glass slide without or with its kaolinite coat, using the same procedure as in Chapters 3.2.4 and 5.2.3. Longer-term wettability alteration was established using a similar procedure to those in Chapters 4.2.3 and 5.2.2 (procedure A). In particular, the salt solution surrounding the model substrate was centrifugally drained by crude oil and aged for 7 days at 60 ^{o}C, as in the sand pack experiments. Bulk oil was removed with decalin and the salt with methanol, to leave the adsorbed/deposited asphaltenics. This adhering material was imaged by FESEM (as in Chapter 3.2.3). It was also extracted from the kaolinite-coated glass using an azeotropic chloroform/methanol blend to determine its dissolved mass using fluorescence spectroscopy (as in Chapter 4.2.4). In particular, the emission intensity at 496 nm from 340 nm excitation was calibrated to concentration via the same analysis of prepared solutions of Tensleep asphaltenes. The spectra and calibration curves are given in Figure 6.2a-c.

These latter two techniques were also applied to the kaolinite-coated sand after flooding and micro-CT. The holder contents were transferred to a tube with the corresponding salt solution and centrifuged at 1000 g for 10 min. to remove oil, and then methanol immersed and ambiently dried. Some grains with kaolinite were inspected by FESEM; the remainder was solvent extracted for fluorescence spectroscopy. The resulting spectra are plotted in Figure 6.2d.

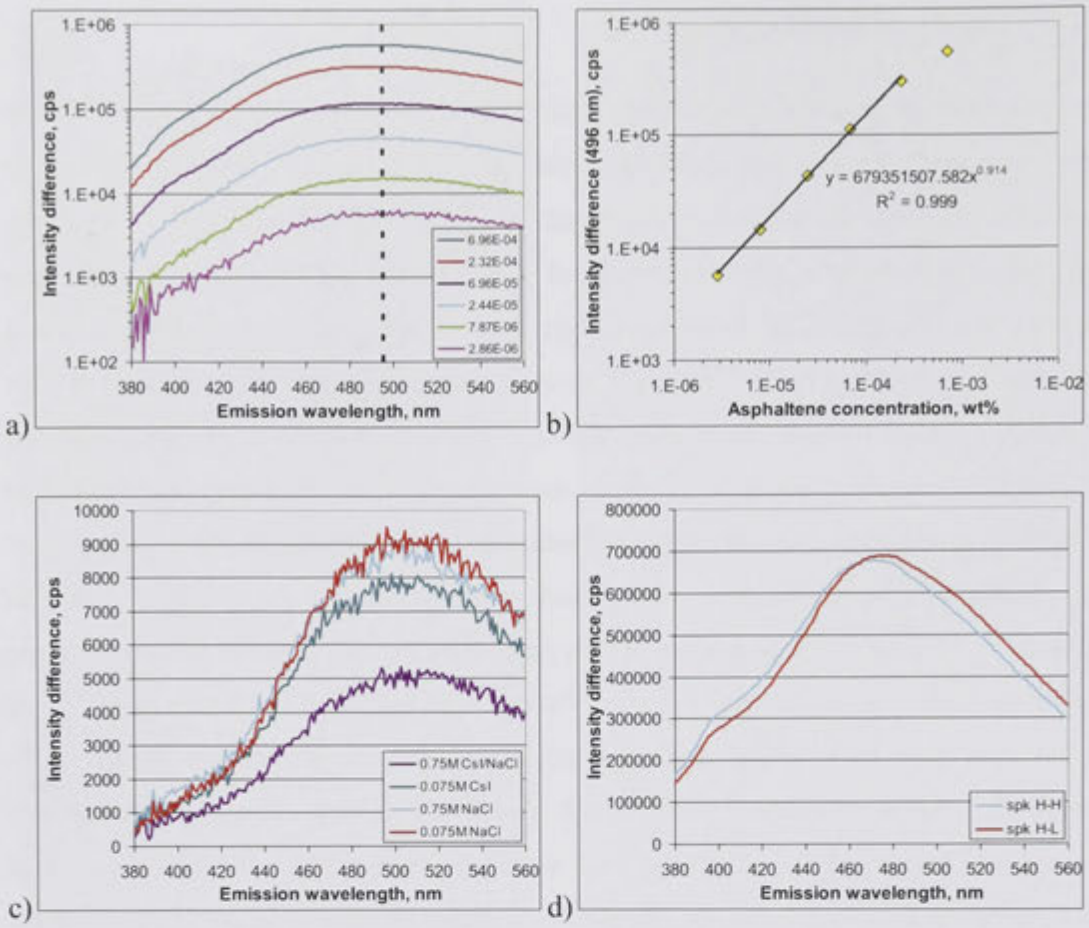

Figure 6.2. *Fluorescence emission spectra of solutions in azeotropic chloroform/methanol excited at 340 nm, for: a) calibration solutions of asphaltenes from Tensleep crude oil, of the wt% concentrations in the legend, showing their broad peak at 496 nm (dotted line), and with b) plotting the resulting calibration relation between these concentrations and their intensity peaks; c) asphaltenic deposits extracted from the kaolinite-coated glass samples after drainage of the four salt solutions in the legend by the crude oil and aging, followed by decalin-methanol rinsing; d) asphaltenic deposits extracted from the kaolinite-coated sand pack samples after flooding with 0.75 M CsI/NaCl (spk H-H) or 0.075 M CsI (spk H-L), followed by removal of the bulk crude oil and methanol rinsing. The intensities at 496 nm in c) and d) are converted to asphaltene concentrations using b), and by normalising by the masses of solvent and sample, yield the deposit amounts in the final two columns of Table 6.1.*

6.3 Results and discussion

6.3.1 3D micro-CT characterisation of pore space and drained state

The micro-CT sample matrix comprised two sand packs without kaolinite (denoted *sp*) and two with kaolinite coating (denoted *spk*), each of which was initially saturated with high salinity solution (0.75 M CsI/NaCl, denoted *H*), drained by oil and aged, and then flooded with this same solution or its low salinity counterpart (0.075 M CsI, denoted *L*).

Samples are thus referred to as *sp H-H*, *sp H-L*, *spk H-H* and *spk H-L*. The tomograms distinguished the 3D locations of grains (the most strongly attenuating phase, appearing very light grey), and aqueous (intermediate, hence darker grey) and oil (weakest, hence darkest) phases occupying the pore space, readily facilitating their segmentation. The 0.2 mm annulus closest to the holder wall was excluded from analysis. The pore space was topologically partitioned into pore bodies and throats (113). The following analysis pertains to the four tomograms after aging (prior to flooding).

For all samples, the grain packs appeared homogeneous and similar. Statistics of the inscribed radii of all pores and their body/throat aspect ratio are presented in Figure 6.3. Porosity and pore size vary only slightly between samples in Figure 6.3a, with the dominant contribution to volume coming from inter-grain pore radii tightly distributed between 50 and 150 μm, with median in the range 89-106 μm. The direct effect of the thin kaolinite lining (Figure 6.1) on structural properties and absolute permeability of the coarse sand packs is expected to be minimal, thus the tendency for coated grains to give slightly larger porosity and pore size may be due to greater friction during compaction. Aspect ratio in Figure 6.3b also varies little between samples, with median from 3.0 to 3.5. The pore spaces are thus structurally very similar, highly permeable and well connected.

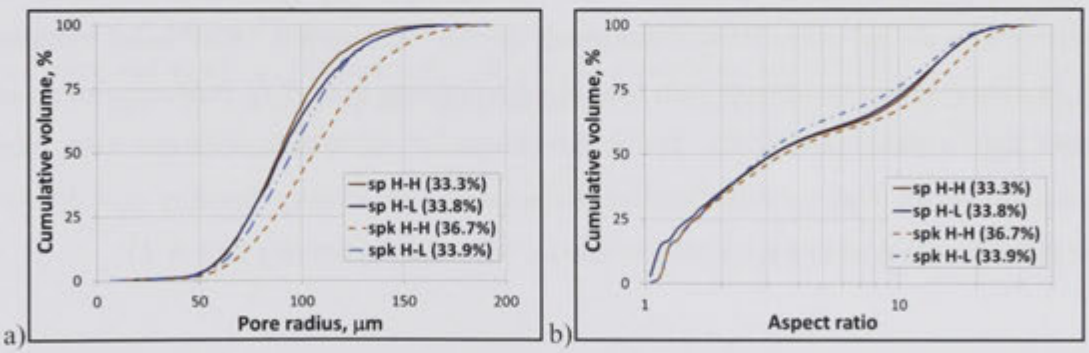

Figure 6.3. *Volume-weighted distributions of pore a) inscribed radius and b) aspect ratio, from the segmented tomograms of the four samples after aging, with overall porosity in the legend.*

Representative images of *spk H-H* and *spk H-L* after aging are given in Figure 6.4. As expected, the salt solution has been drained to remain only in the tighter confines, filling smaller pores or occupying the corners of larger pores, often in the form of rings collaring grain contacts. These pendular rings are more apparent in the visualisations of Figure 6.4c-d using Drishti software. Some rings are connected to neighbors, while

others appear isolated and/or incomplete, however hydraulic connectivity may persist in grain roughness and lining kaolinite, below micro-CT resolution. All samples appear qualitatively as in Figure 6.4. Moreover, their irreducible water saturation, S_{wi}, resolved in the pore space of the segmented tomograms for this initial state is very similar (9.9, 11.2, 10.1 and 8.6% for *sp H-H*, *sp H-L*, *spk H-H* and *spk H-L*). These values tally with the gravimetric estimate at the conclusion of air drainage (in Chapter 6.2.2), and are in line with other studies of granular packs (104; 117). The kaolinite linings do not lead to bulk water drainage from small pores, as was inferred from a micro-CT study of water-wet Berea sandstone (114).

6.3.2 3D micro-CT pore-scale characterisation of residual oil

Owing to the small sample size required for micro-CT, oil production was not monitored volumetrically during flooding. Instead, the residual oil saturation, S_{or}, after the 25 PV flood was determined from the segmented tomograms. Figure 6.5 plots the percentage of pore space occupied by oil voxels post-flooding relative to the initial-state percentage (100–S_{wi}) of original oil in place (OOIP), for the four once-flooded samples and the one subsequent low-salinity flooding (*spk H-H-L*) in "tertiary" mode. The most striking feature is the detrimental effect of the small amount of kaolinite (comprising only 0.28 wt% of the sand pack), which on average more than doubles S_{or}. The kaolinite-free sand pack flooded at high salinity (*sp H-H*) gave the most complete recovery, with its low salinity counterpart *sp H-L* leaving 5% OOIP more residual. Kaolinite reverses this trend, with low salinity flooding (*spk H-L*) producing more oil than high salinity (*spk H-H*). The disadvantageous effect of kaolinite is thus most pronounced for high salinity flooding. Subsequent low salinity flooding (*spk H-H-L*) reduced the residual to a level comparable to "secondary" recovery (*spk H-L*).

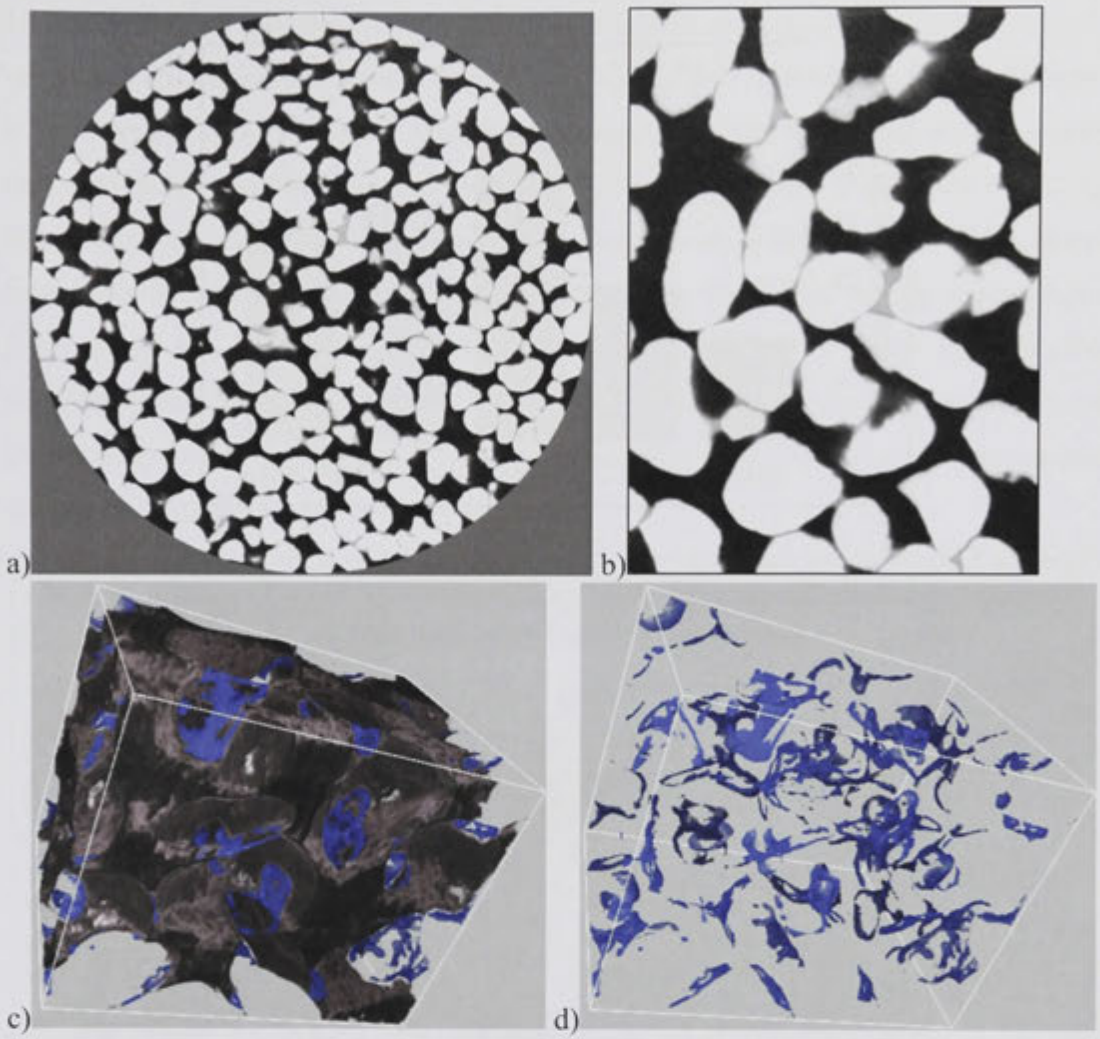

Figure 6.4. *Micro-CT images of kaolinite-coated sand packs after oil drainage of salt solution and aging: a) 2D horizontal slice of the 8 mm diameter of spk H-H, b) subarea (2.0x2.7 mm^2) of this slice, c) 3D visualisation of a subvolume (1.7x1.3x1.3 mm^3) of spk H-L showing crude oil (black) and salt solution (blue) without grains, and d) showing only the solution.*

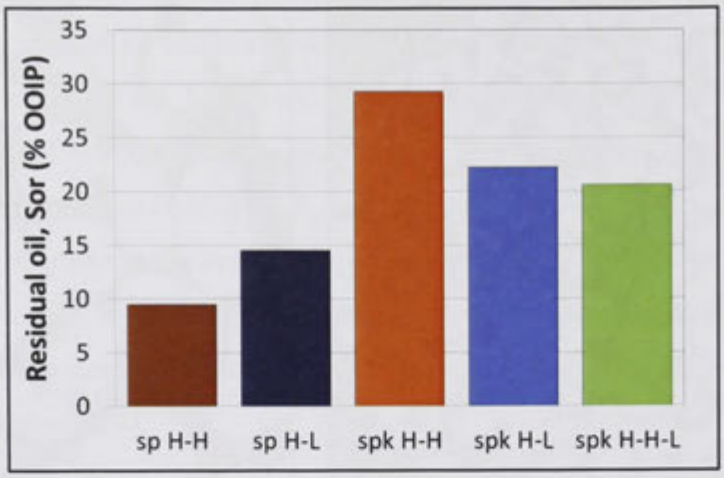

Figure 6.5. *Residual oil fractions resolved from micro-CT of sand packs without (sp) or with (spk) kaolinite linings, after flooding at high (-H) or low (-L) salinity, or both sequentially (-H-L) for the final sample.*

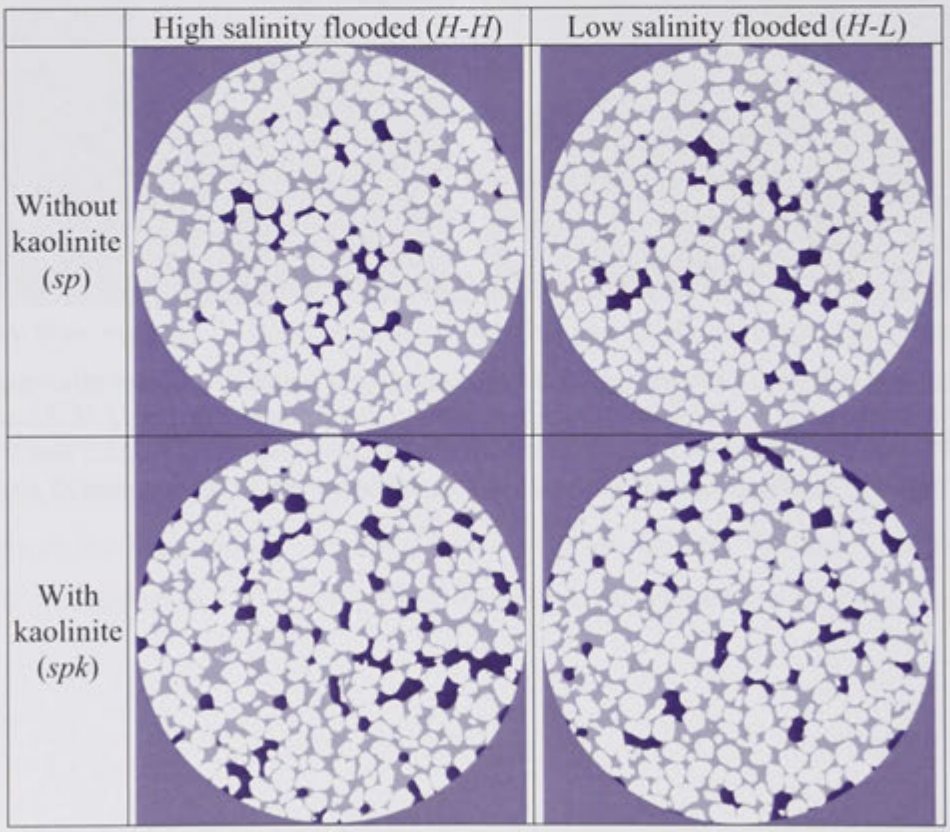

Figure 6.6. *2D horizontal slices of the segmented tomograms for the 8 mm diameter sand packs without or with kaolinite after high or low salinity flooding. Grains are white, salt solution is light purple and oil is darkest purple.*

Understanding of the mechanisms responsible entails investigation of oil residuals at pore-scale (in the remainder of Chapter 6.3.2) and down to molecular scales (Chapter 6.3.3). Typical slices within the segmented tomograms of the four packs after secondary recovery (single flooding) are compared in Figure 6.6. Although *sp H-H* has lowest S_{or}, the residual oil blobs appear to span many pores (even in the 2D slice which under-represents 3D connections), tending to snake along somewhat tighter macro-pores. Although *sp H-L* has more residual, it appears less connected in Figure 6.6, and often occupies somewhat larger pores. Sample *spk H-H* has greatest residual, in the form of highly connected clusters often filling somewhat larger pores, while the lower residual for *spk H-L* exhibits less pore spanning.

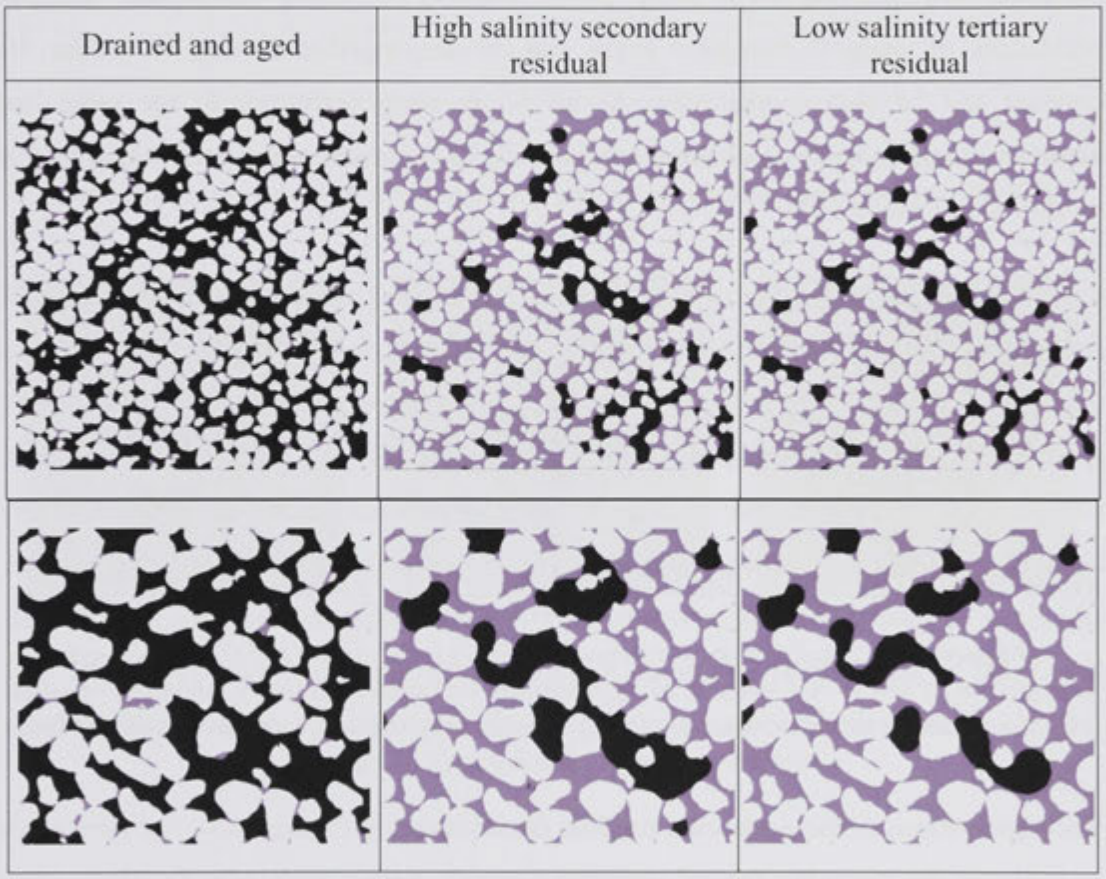

Figure 6.7. *A corresponding vertical slice (after flow in the upwards direction) of the registered segmented tomograms of spk H-H-L in its three imaged states, showing a subarea (7.4x7.6 mm^2, above) and a close-up (3.7x3.3 mm^2, below) near its center.*

Tomograms after aging and after flooding(s) were aligned and superposed using a registration algorithm (32). Comparison of these registered images showed no significant grain movement during flooding. The differences in recovery are thus due to

kaolinite and the flood salinity. Figures 6.7 and 6.8 show registered 2D slices and 3D visualisations of the coated grain pack after aging and the *H*-flood (*spk H-H*) and following *L*-flood (*spk H-H-L*). From the drained and aged state in Figure 6.7, the flooding aqueous phase largely maintains its initial occupation of tighter pore confines (as seen in other studies (115)), while advancing to displace oil, leaving residuals ranging from isolated blobs in single pores (singlets) to connected clusters spanning many pores. From the secondary recovered state, the pore-scale changes in residual on tertiary recovery in Figures 6.7 and 6.8 are identifiable as resulting from further advance of aqueous phase causing further oil retraction. Smaller blobs isolated after secondary recovery typically remain unperturbed. Oil in larger clusters recedes, leading to complete displacement from some pores, thinning in other pores, and frequent incidences of snap-off in tighter pores and throats, together serving to reduce the residual and its blob connectivity. As all floods were performed at the same low capillary number ($5x10^{-7}$) and Bond number ($\sim 3x10^{-3}$), the extra recovery cannot be due to blob mobilisation (106).

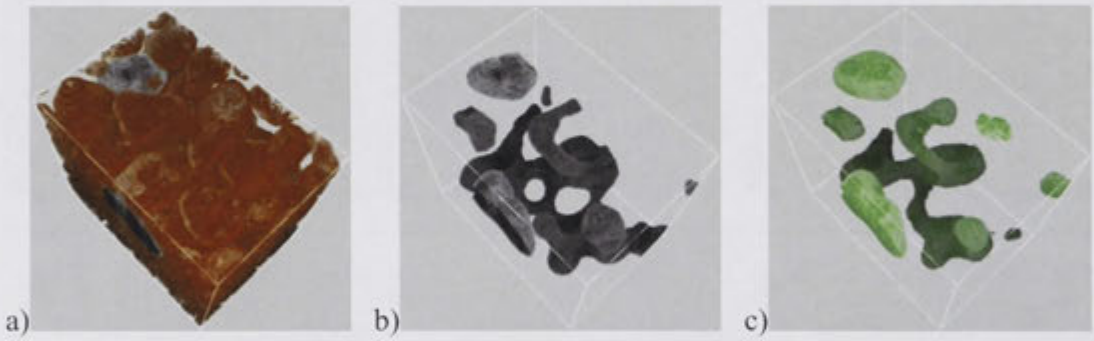

Figure 6.8. *Visualisation of a subvolume (1.7x1.4x2.0 mm^3) of the registered tomograms of spk H-H-L after a, b) high salinity secondary recovery, showing residual oil (black) and grains (brown, only in a)) without salt solution, and after c) low salinity tertiary recovery, showing only oil (green).*

The observations of the pore-scale residual distributions in Figures 6.6 - 6.8 were made quantitative by summing the oil-segmented voxels within each pore to obtain their volume per pore volume and thus the pore's oil saturation (115; 118). The oil occupancy statistics are presented in Figures 6.9 - 6.11. The first, least discerning measure is the volume-weighted histogram of residual oil in Figure 6.9. The plotted range of pore volumes corresponds to equivalent sphere radii from 13 to 620 μm. (This radius definition is to be distinguished from that in Figure 6.3a, which refers to the radius of the largest inscribed sphere, and is lower by a factor of 1.7-2.) The sub-range significantly contributing to residual volume in Figure 6.9 equates to radii from ~110 to

330 μm. The distributions for all flooded samples appear similar, with median pore radius within 220-240 μm. Among the slight differences, the residual for *sp H-H* is in smaller pores than *sp H-L*, and that for *spk H-H* is in larger pores than *spk H-L*.

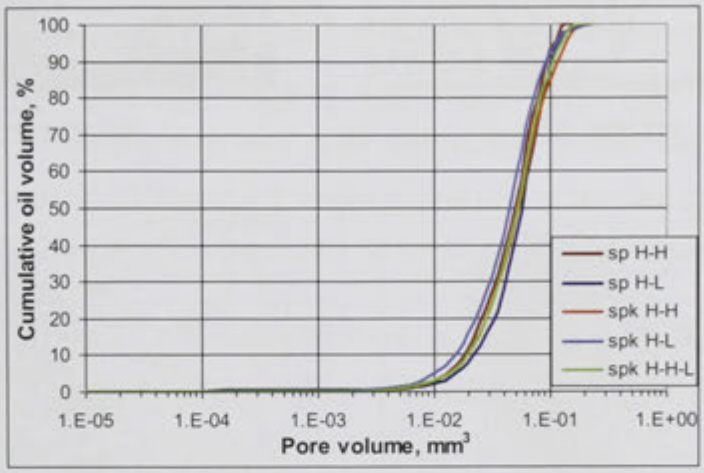

Figure 6.9. *Normalised cumulative distribution of total volume of residual oil versus volume of pores in which it is trapped, from the segmented tomograms of the five flooded samples.*

Figure 6.10 again summarises the pore occupancies versus their volume over this same range, but now in the more sensitive form of number-weighted statistics. As most pores are completely water saturated, the scatter plots in Figure 6.10a-e include only those containing at least 1% oil. Moving averages of oil saturation are given over all pores (brown curve) and the subsets with at least 1% (red) or 50% (blue) oil occupancy. To put the plots into perspective, the number-weighted histograms of all pores are given by the unfilled pink symbols, normalised to 100%, compared to the frequency of pores less than 1% oil-occupied (i.e. those not included in the scatter plot), given by filled pink symbols. The latter are similarly normalised by the total number of all pores.

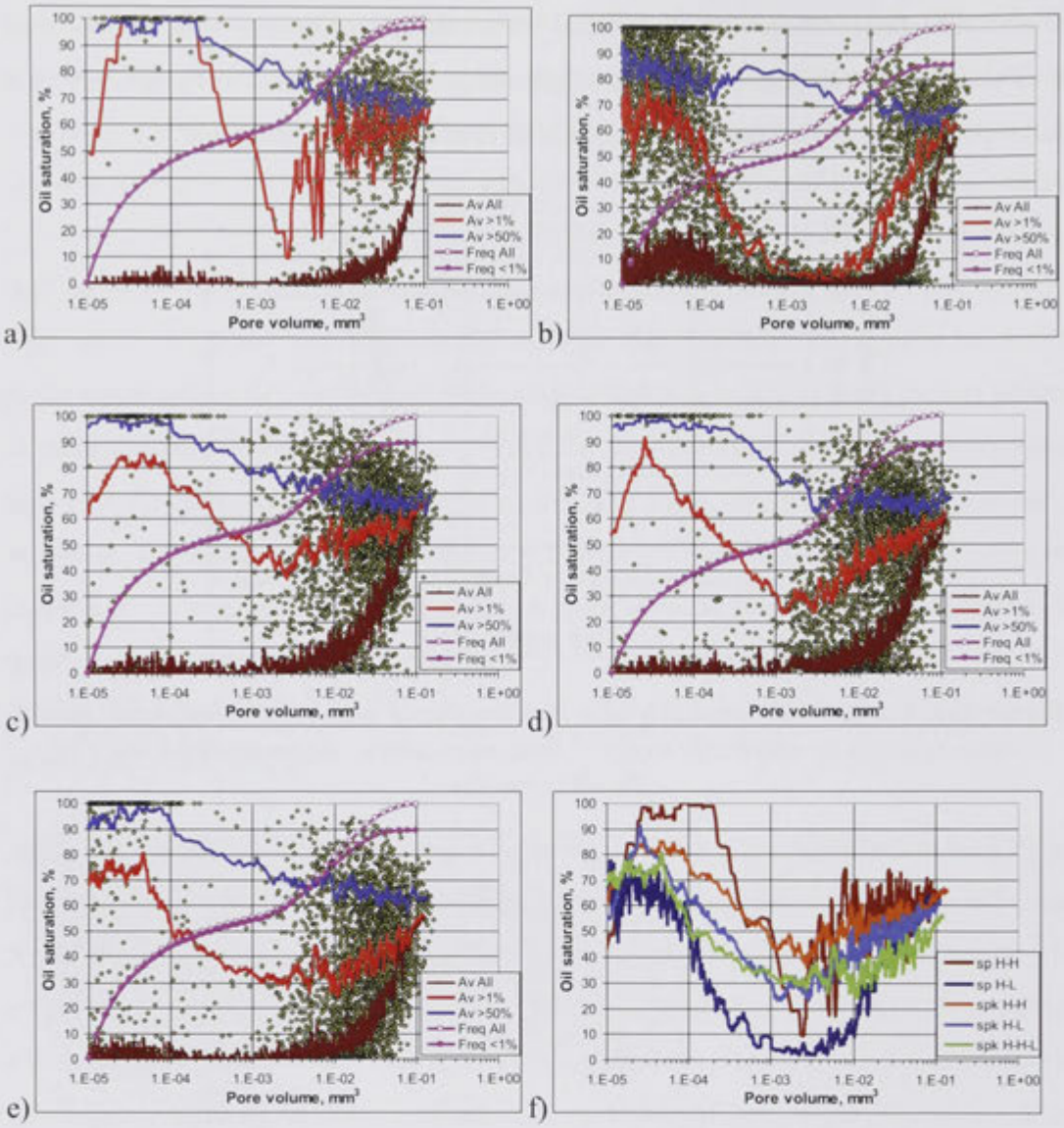

Figure 6.10. *Scatter plots of oil saturation in each pore having >1% oil occupancy versus its pore volume, from the segmented tomograms of the flooded samples: a) sp H-H, b) sp H-L, c) spk H-H, d) spk H-L, e) spk H-H-L. Moving averages are in brown (all pores), red (pores >1% occupied) and blue (>50% occupied); the curves for >1% occupation are compared in f). The pink curves in a)-e) are cumulative frequency distributions of all pores (unfilled symbols) and pores with <1% occupancy (filled symbols).*

Prior to interpreting Figure 6.10, it serves to further quantify the residual oil in terms of its connectivity. Oil in each pore was checked for connections to oil in neighboring pores to identify the continuous blobs and characterise their size via the number of pores each spans (115; 118). The histograms of blob size, weighted by the volume of oil in each, are given in Figure 6.11 for the five flooded packs. As in Figure 6.10, a lower cut-off for oil occupancy must be imposed. The dependence of the distributions on this definition is shown in Figure 6.11a for *spk H-L*. The 50% cut-off was chosen here as the

fairest compromise between over- or under-estimation. The resulting distributions are shown in Figure 6.11b; alternative cut-off choices change the sizes but not the hierarchy between samples (as also seen in other studies (115)). While the relative volume of oil trapped as singlets or doublets is greatest for the kaolinite-free packs having lowest overall residual (Figure 6.5), the population of larger blobs is more dependent on the flood salinity. High salinity leaves more connected oil, with over half of the total residual volume comprising one very large cluster. The median blob size in Figure 6.11b increases with S_{or} in Figure 6.5 within the subsets of two and three samples last flooded at high or low salinity, respectively; however, there is no universal relation.

The trends in Figures 6.6 - 6.8 discussed above are consistent with these distributions. For *spk H-H*, the 64% of its residual oil left connected as one multi-cluster occupying 1110 pores provides a ready target for the tertiary recovery (*spk H-H-L*) in Figures 6.7 and 6.8. This lowers its residual fraction and blob size to levels comparable to *spk H-L* directly flooded with low salinity. Indeed, the corresponding curves without the normalisation by total residual volume (Figure 6.11c) are almost overlain for all three low-salinity flooded samples. A micro-CT study of residuals after flooding of Fontainebleau sandstone and carbonates (115) generally gave blob sizes of similar order of magnitude to the current study, while water-wet Berea sandstone (114) showed mostly singlets and with the largest blob size mirroring S_{or}. For cases such as *spk H-H* in which residual features span a substantial fraction of the tomogram dimensions, the imaged volume cannot be regarded as truly representative, and thus the trends (e.g. to large clusters for *spk H-H*) and their causes, rather than the absolute values, are the focus of this study.

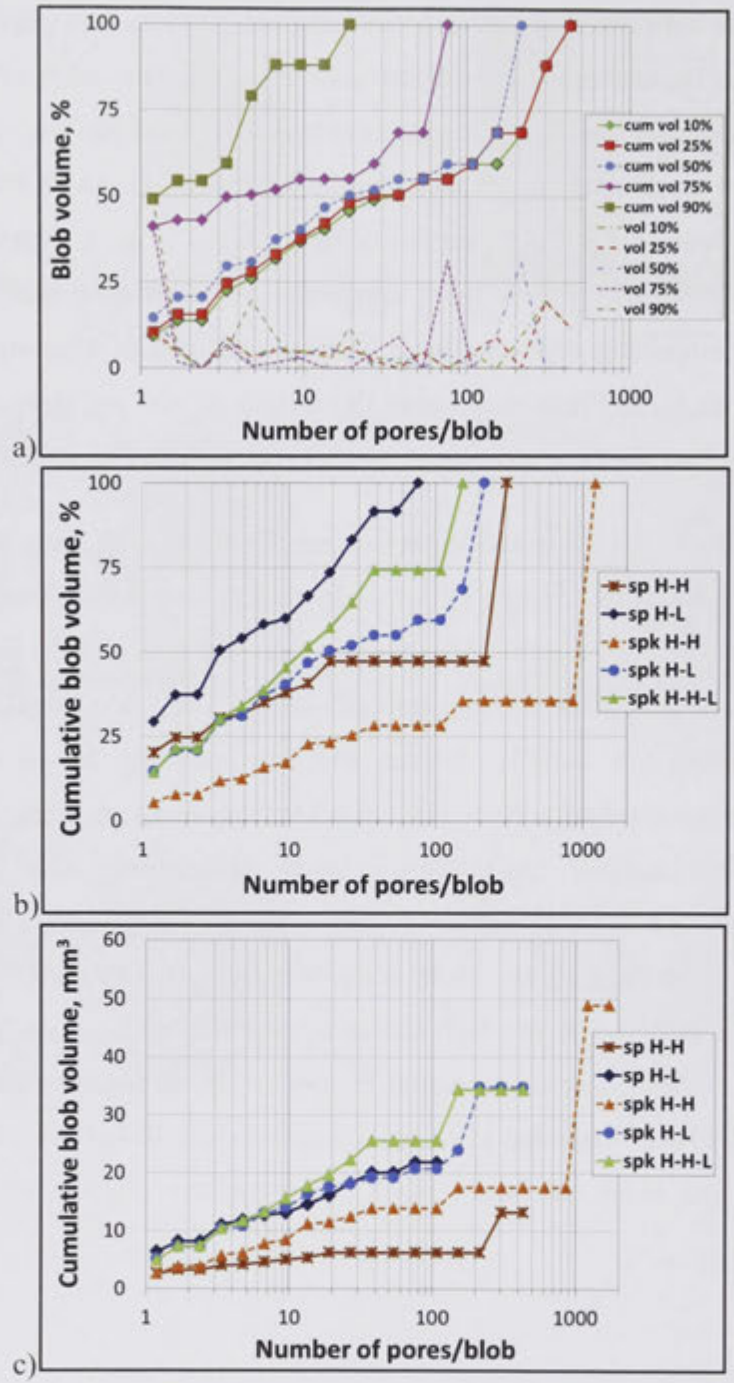

Figure 6.11. *a) Normalised incremental and cumulative volume distributions of residual oil blobs in spk H-L versus blob size, defined as the number of pores each spans, using the occupancy criteria of the blob filling >10, 25, 50, 75 or 90% of a given pore's volume. b) Cumulative volume distribution of blobs for all flooded samples, using the 50% occupancy cut-off. c) As for b) but with the vertical axis not normalised to 100%, and thus the curves increase to the total volume of residual oil in each tomogram.*

We now return to Figure 6.10 and consider first the leftmost part of the plots, covering pore volumes of 10^{-5}-10^{-4} mm^3, corresponding to inter-grain smaller pores and deeper depressions in irregular grains. Despite their insubstantial contribution to the overall volumes in Figure 6.9, these pores are frequent; indeed even smaller pores arise in the segmented tomograms, but are difficult to differentiate from image noise and are not considered. The small pores in Figure 6.10 are most often water-filled, by retention of the initial solution and/or oil displacement on flooding, and for three samples, the frequency of oil occupation is insignificant, as shown by the all-pores average curve (brown) and the coincidence of the pair of cumulative curves (pink). For *sp H-L*, and to a lesser degree *spk H-H-L*, oil occupation is more common and displays a range of saturations. Their moving average for >1% occupation (red curve) in Figure 6.10b and e are misleadingly lower than the other three samples, as the few occupied small pores of the latter tend to have high saturations. These two samples *sp H-L* and *spk H-H-L* also have the most finely divided blobs in Figure 6.11b, suggesting that oil trapping by snap-off is prevalent. Further, in the course of oil break-up and displacement from the large clusters of *spk H-H* in Figure 6.11b by tertiary recovery (*spk H-H-L*), the oil occupation of small pores somewhat increases.

For larger pore volumes around 10^{-3} mm^3, the continued lack of contribution to oil volume in Figure 6.9 is due both to the paucity of pores of this size in Figure 6.10 (shown by the low slope of the cumulative frequency distributions) and the incomplete saturation of those which are occupied. Thus the >1% and >50% moving averages dip, although the statistics there are poorest (especially for *sp H-H* with least residual). Again *sp H-L* has most number of occupied pores, although generally less than 10% saturated. As there is virtually no evidence of its pores bearing oil linings, these low saturations are mainly due to very small singlets (some of which are seen in Figure 6.6) and to the pore partition including small contributions from neighboring blob terminations.

For pore volumes increasing further to 10^{-2}-10^{-1} mm^3, the strong contribution to oil volume in Figure 6.9 reflects 1) the larger capacity, 2) the coinciding onset of a significant frequency of occupied pores (marked by the divergence of the pair of cumulative curves in Figure 6.10), and 3) their increased oil saturation (i.e. the upturn of the all-pores and >1% moving averages). For *sp H-H* the occupied pores are generally at least half full of oil, while for *sp H-L* the broader range of low-intermediate saturations is again thought to be due to its frequent blob terminations partly intruding into

neighboring pores. The density of scatter points is naturally greater for the high-residual kaolinite-coated samples. Their saturations shift downwards and to a more uniform, random distribution in the sequence from *spk H-H* to *spk H-L* to *spk H-H-L* in Figure 6.10c-e, again mirroring the corresponding blob size decrease in Figure 6.11b. The slight differences in the five all-pores average curves follow the same hierarchy as their residuals in Figure 6.5. Compared to other micro-CT studies, the scatter plots and all-pore averages are qualitatively similar to those from Fontainebleau sandstone flooding (115), while a wider spread of saturations across all pore sizes was inferred from water-wet Berea flooding (114).

6.3.3 Molecular-scale mechanisms

The micro-CT analysis characterises the differences in pore-scale oil distributions, but cannot resolve kaolinite particles and wettability-altering asphaltenic deposits to pinpoint the molecular-scale causes. The supplementary suite of surface analytical techniques probes the interactions between oil, salt solution and mineral, which dictate the underlying wettability. The simplified systems replace grains by a glass slide (as in Chapter 5) and kaolinite-coated grains by kaolinite-coated glass (as in Chapters 3-4), to facilitate quantification of contact angles and asphaltenic deposits. The analyses for the two solutions, 0.75 M CsI/NaCl and 0.075 M CsI, are compared to those using 0.75 and 0.075 M NaCl, to assess the influence of the micro-CT contrast agent on the observed recovery.

The receding and advancing contact angles of growing and retracting crude oil drops on these two clean model substrates in each of the four solutions are plotted in Figure 6.12. Judging from the advancing angles, glass is altered from water-wet to intermediate-wet or moderately oil-wet after the 30 min. in contact. The two 0.075 M solutions behave similarly, while surprisingly, the 0.75 M counterparts diverge somewhat. For NaCl, the advancing angle decreases with salinity, as often observed in such systems (62; 57) and in Figure 5.8a for Minnelusa crude oil, while it increases for CsI/NaCl. As the receding angle tends to mirror the advancing trends in Figure 6.12, the alteration begins on first contact. In contrast, on kaolinite-coated glass, the receding angles in all solutions are very similar, and the advancing angles are only slightly greater. For example, they are significantly smaller than the corresponding advancing angles for Minnelusa crude oil in NaCl solutions at natural pH in Figure 3.10a. The Tensleep crude oil has a very limited ability to displace water surrounding kaolinite particles and instil adhesion

during the 30 min. While kaolinite remains largely water-wet, the advancing angle increases slightly with NaCl salinity, and decreases with CsI/NaCl, i.e. the opposite of the trends on glass in Figure 6.12.

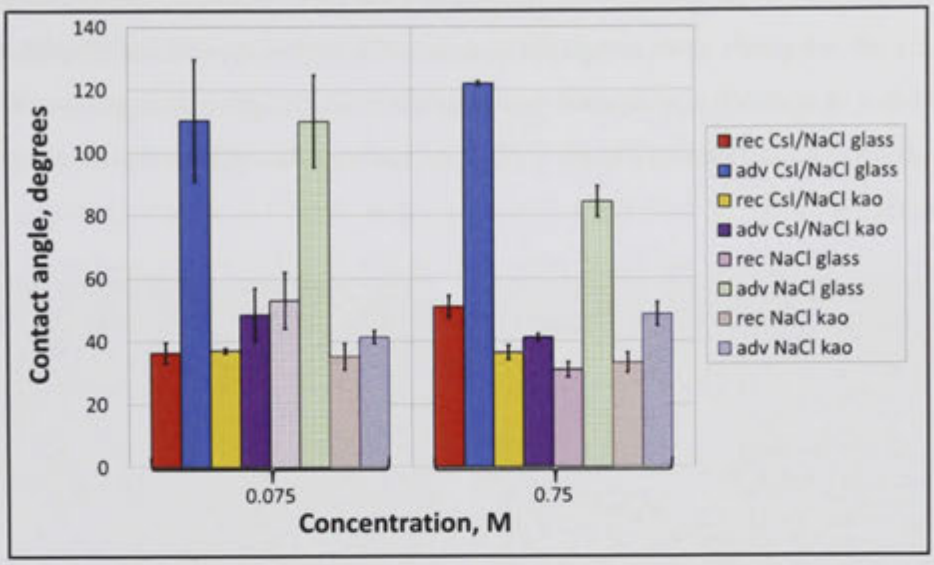

Figure 6.12. *Average and standard deviation (error bar) of receding (rec) and advancing (adv) angles of crude oil drops (3 replicates) on glass and kaolinite-coated glass (kao) in the CsI/NaCl or pure NaCl solutions at the two concentrations.*

The wettability alteration of the model substrates after drainage of each of the solutions by crude oil and aging was assessed by the extent of asphaltenic deposition. This procedure is not identical to that for the sand packs, in which the initial solution was 0.75 M CsI/NaCl and salinity of the flood was varied, however it provides insight into the salt dependence of longer-term adhesion. Figures 6.13 and 6.14 show representative FESEM images of the deposits on glass and kaolinite substrates, respectively. On glass the deposits are a scattering of nanoparticle aggregates separated by relatively clean subareas. The area coverage of glass by deposit was quantified by image analysis (as in Chapter 5.3.1), giving the coverage statistics in Table 6.1 from all micrographs. The coverage values are quite low compared to Minnelusa oil; for example, compare Figure 6.13 to Figure 5.3a and c, and Table 6.1 to Figure 5.2 for procedure A. However, these coverage values for Tensleep oil are strongly correlated ($R^2 = 0.95$) to the advancing angles on glass in Figure 6.12, further evidencing that wettability alteration is established early and proceeds little, or intact, thereafter.

For kaolinite-coated glass in Figure 6.14, the platelets remain almost completely free from nanoscopic deposits; the occasional larger agglomerate is due to sedimentation of asphaltene flocs preexisting in Tensleep oil (88). For example, compare the relatively

clean platelets in Figure 6.14 to the platelets with heavy deposits after Minnelusa oil aging in Figure 4.4b. The asphaltenics were extracted in chloroform/methanol for spectroscopy of their natural fluorescence (see Figure 6.2a-c), yielding the inferred deposit mass per planar area of kaolinite-coated slide in Table 6.1. As expected, these values are all extremely low (compared to around 20 mg/m^2 typical for Minnelusa oil in Figure 4.3a), despite the extraneous contribution from the preexisting flocs. Thus, the water-wetness of kaolinite in Figure 6.12 is maintained throughout the long-term aging in Tensleep oil.

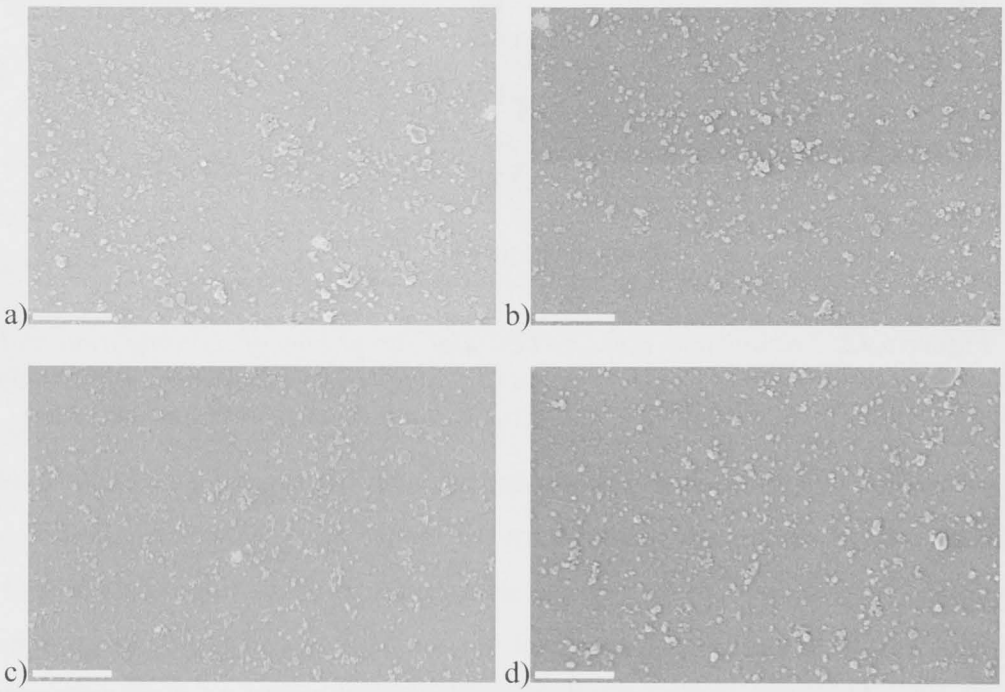

Figure 6.13. *Representative FESEM images of asphaltenic deposits on glass after drainage of a) 0.75 M CsI/NaCl, b) 0.075 M CsI, c) 0.75 M NaCl, or d) 0.075 M NaCl solution by crude oil and aging, followed by decalin-methanol rinsing. Scale bars are 0.5 μm. The very fine texture visible within subareas of glass between asphaltenic deposits in all images is the conductive platinum coat.*

These observations are consistent with those of the kaolinite-coated grains after flooding and disassembly of the pack to remove bulk oil. Representative FESEM images for *spk H-L* are shown in Figure 6.15; *spk H-H* is qualitatively comparable. Open grain surfaces bear an incompletely covering texture of nanoscopic aggregated asphaltenics, similar to glass (Figure 6.13), plus occasional submicron oil droplets (seen at the right of Figure 6.15b). Kaolinite remains relatively deposit-free, as for the model coats (Figure 6.14). The asphaltenic mass extracted from the kaolinite-coated grains and assayed spectroscopically as above (see Figure 6.2d) is listed in Table 6.1. Both values are expectedly low, with *spk H-H* being the slightly smaller.

It appears that the differing residuals and pore-scale distributions in the sand packs mainly reflect their differing wettability. This is borne out by the negative correlation in Figure 6.16 between S_{or} in Figure 6.5 for the sand without or with kaolinite and advancing angle in Figure 6.12 on glass or kaolinite-coated glass, respectively. As the mixed-wet samples are at most only moderately oil-wet in their altered subareas, further weakening of this oil-wetness and adhesion would be expected to reduce recovery by favoring oil disconnection during flooding (22; 110; 111; 112). On glass, the higher contact angles in Figure 6.12 and slightly greater deposition in Table 6.1 for 0.75 M CsI/NaCl composed to 0.075M CsI thus tally with the greater recovery from uncoated sand by high salinity flooding (*sp H-H*). The finely divided blobs in Figure 6.11b for *sp H-L* evidence the increased snap-off to which the increased water-wetness contributes.

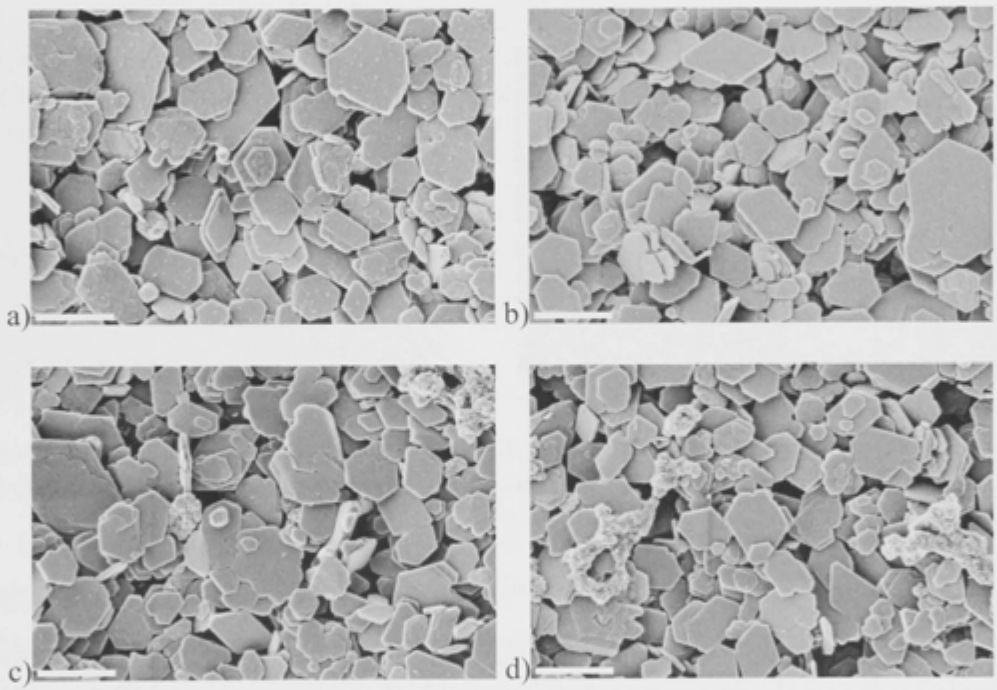

Figure 6.14. *Representative FESEM images of asphaltenic deposits on kaolinite-coated glass after drainage of a) 0.75 M CsI/NaCl, b) 0.075 M CsI, c) 0.75 M NaCl, or d) 0.075 M NaCl solution by crude oil and aging, followed by decalin-methanol rinsing. Scale bars are 0.5 μm. The very fine texture visible within subareas of kaolinite platelets between asphaltenic deposits in all images is the conductive platinum coat.*

Table 6.1. *Average and standard deviation of measured surface properties of oil and mineral phases in the four salt solutions of given CsI and NaCl concentrations: Zeta potential (ζ) of oil, quartz and kaolinite; Number of oil drops stabilised by kaolinite; Area coverage of glass slides by asphaltenic deposit after aging; Mass (mg) of asphaltenic deposit on kaolinite-coated glass per slide area (m^2) after aging; Mass (mg) of asphaltenic deposit remaining on kaolinite-coated sand per sand mass (g) after flooding by the CsI/NaCl solutions.*

[CsI], M	[NaCl], M	ζ oil, mV	ζ quartz, mV	ζ kaolinite, mV	Emulsion oil drops, no.	Glass deposit, coverage %	Kaolinite deposit, mg/m^2	spk deposit, mg/g
0.125	0.625	-15.8±2.5	-11.1± 1.7	4.2± 0.6	79±3	6.38±0.85	0.70	0.027
0.075	0	- 27.3±1.4	-29.1± 1.6	7.8± 0.4	133±14	6.20±1.08	1.17	0.030
0	0.75	-4.2±1.1	-14.7± 0.9	-6.4± 0.7	74±12	4.65±0.67	1.21	-
0	0.075	-1.2±2.5	-36.6± 0.6	-15.1± 0.5	64±36	5.88±1.44	1.17	-

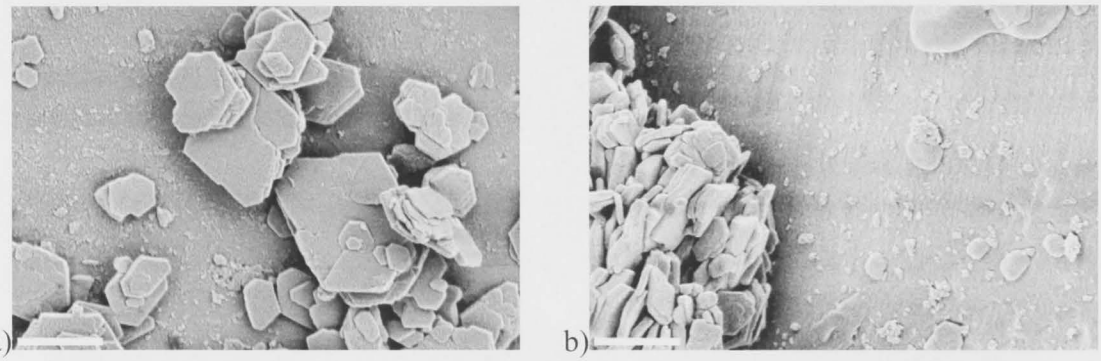

Figure 6.15. *FESEM close-ups of kaolinite-coated sand from spk H-L after drainage, aging and flooding with 0.075 M CsI solution, followed by methanol rinsing. Scale bars are 0.5 μm.*

The S_{or} of around 15% typical for capillarity-driven recovery from homogeneous, water-wet bead packs (104; 106) is thus consistent with the lower value for *sp H-H* and similar value for *sp H-L* in Figure 6.5. It is possible that the water-wet shift for *sp H-L* is compounded by the osmotic pressure acting to dilute and thicken the high salinity connate film intermingled between the sparse asphaltenic deposits, which anchor oil to grains. As the concentration trends in Figure 6.12 and Table 6.1 are reversed if CsI/NaCl is switched to NaCl, low salinity flooding may give more complete recovery for the NaCl solutions of greater relevance to real reservoir brines.

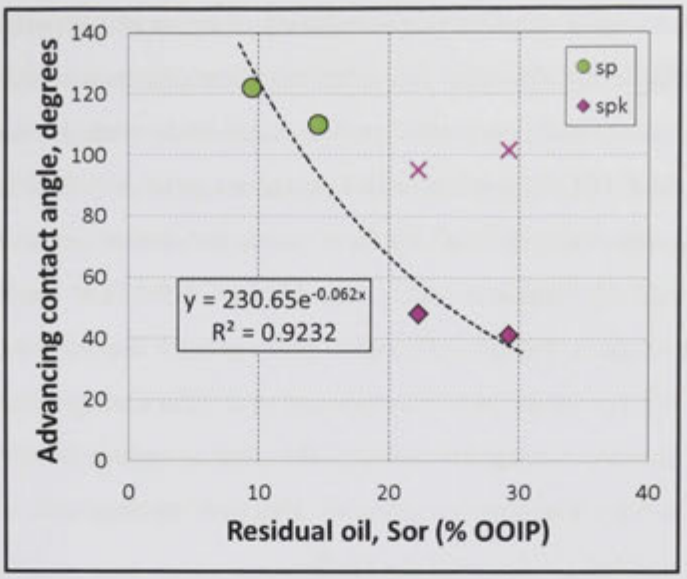

Figure 6.16. *Correlation between residual oil in the sand packs without (sp) or with (spk) kaolinite after flooding and the advancing angle of a crude oil drop on glass without or with kaolinite coating, respectively, in the corresponding flooding solution. Crosses indicate the contact angles predicted by eq. 6.1 for kaolinite-coated sand.*

The partial coverage of grains by kaolinite particles, which retain surface water, strongly increases residual oil. An effective contact angle can be estimated for kaolinite-coated grains via Cassie's law (119):

$$\cos\theta_c = f_1 \cos\theta_1 + f_2 \cos\theta_2 \qquad (6.1)$$

Here θ_c is the contact angle on the composite surface comprising materials i =1 and 2 of area fraction f_i within which the corresponding angles are θ_i. From analysis of 60 FESEM images, each 60x40 μm^2, of untreated coated grains (e.g. see Figure 6.1c-f), the projected area fraction covered by kaolinite averages 26% with standard deviation 16%. The composite advancing angle from eq. 6.1 for this fraction and the advancing values on glass and kaolinite-coated glass in Figure 6.12 gives the two points marked by crosses in Figure 6.16. The correlation for the composite is poorer than for kaolinite alone, suggesting that kaolinite plays a greater role than merely contributing to wettability via eq. 6.1. This is further evidenced by the fact that the S_{or} in Figure 6.5 for all three coated packs significantly exceed the 15% expected in the strongly water-wet extreme (104; 106).

One possible explanation for the largest residual and cluster size in Figure 6.11b-c for *spk H-H* is that the grains are sufficiently water-wet, and thickly sheathed by water films in the roughness and pores of the kaolinite lining, that the pack becomes prone to

oil bypassing due to rapid spontaneous imbibition of water along pathways preferred or established by capillarity. Despite the relatively homogeneous packing, domains of somewhat larger, connected pores exist and often coincide with the location of residual oil (Figures 6.7 and 6.10). Bypassing in homogeneous pore networks has also been seen in 2D glass micromodels (104) of uniform pore and throat sizes with intermediate aspect ratio (around 3) similar to our packs (Figure 6.3b). On kaolinite, the slightly higher advancing angle in Figure 6.12 and slightly greater deposition (also on the lined grains) in Table 6.1 for 0.075 M CsI composed to 0.75M CsI are in line with *spk H-L* becoming less water-wet during low salinity flooding to reduce bypassing and increase recovery. The primary trapping mechanism switches to snap-off, evidenced by the decrease in blob size for *spk H-L* and *spk H-H-L*.

It is again conceivable that osmotic pressure aids the drawing in of low salinity solution between oil and grain, especially given the increased access afforded by the kaolinite, to displace or trap oil, depending on the aspect ratio. Further, some degree of kaolinite mobilisation may occur. As one check for migration, the effluent from *spk H-H* and *spk H-L* was centrifuged at 1000 g for 10 min. No kaolinite sediment was visually apparent; however, this test cannot detect traces in such small volumes, and mobilised particles may be recaptured by downstream grains or the frit. It is possible that for *spk H-L* and *spk H-H-L*, the expected increase in electrostatic repulsions at low salinity leads to partial removal of kaolinite and rapid alteration of exposed grain patches towards oil-wetness to aid recovery. The emulsion test in Table 6.1 shows that mobilised kaolinite can interfacially stabilise crude oil drops in all salt solutions, and more so in 0.075 M CsI. This may further aid recovery by reducing snap-off, or disadvantage recovery by hindering snapped-off blobs from re-coalescing (99).

Zeta potential of oil, quartz and kaolinite in the solutions can give insight into the electrostatic interactions contributing to the observed wettability and in turn oil recovery. The measured potentials, all at natural pH around 6, are listed in Table 6.1. In the NaCl solutions, the oil is close to its isoelectric point and thus a significant fraction of its surface base groups are protonated and attracted to the deprotonated acid sites on quartz. This is consistent with the glass wettability alteration in Figure 6.12, which reduces at high NaCl in line with the weakened attraction. However, as Tensleep crude has relatively low acid and base numbers, and many of these groups are internalised in pre-existing asphaltene aggregates, the coarse but sparse deposition on glass is presumably driven not only by electrostatic and van der Waals attractions but also by

surface precipitation and hydrophobic attractions. Kaolinite is less negatively charged than quartz in Table 6.1, partly contributing to its water-wetness, although the above-mentioned capillary retention of thicker water films is presumably the main cause. Compared to the NaCl solutions, zeta potentials in their CsI/NaCl analogues in Table 6.1 are slightly less negative for quartz, but much more negative for oil, and reverse to positive for kaolinite. Unlike NaCl, CsI is potential determining, with I^- ions binding to the oil interface and Cs^+ to kaolinite. The fact that angles and deposits are relatively unchanged by this drastic switch again points to the importance of non-electrostatic interactions for the pre-aggregated Tensleep oil. Further, these oppositely-charged monovalent ions on oil and kaolinite give little or no extra scope for interfacial bonding to develop adhesion.

6.4 Conclusion

This study demonstrated the integration of micro-CT imaging with supplementary surface analyses (procedures for which were developed in Chapters 3-5) to visualise and quantify both the distribution of residual oil blobs in pores after waterflooding and the finer features such as nanoscale oil deposits on pore walls, to thus trace the effect of recovery to its cause. The approach is expected to be broadly applicable to reservoir rocks having micro-CT resolvable pores, since FESEM imaging of deposits can be performed on cut rock faces and the parallel analyses of dressed model substrates can be further extended to other relevant minerals. For the quartz sand packs addressed here, the presence of a gravimetrically minute fraction of kaolinite had a substantial effect on oil recovery, owing to its distribution as a patchy lining of considerable grain coverage. The kaolinite was found to diminish oil recovery and reverse its dependence on waterflood salinity, in line with the wettability trends. These results are naturally tied to the choice of crude oil and salt solutions. Many other oils display a high affinity for kaolinite, as shown in our studies in Chapters 3-4 and reported in the literature (85), in which case the platelets can increase, rather than reduce, overall oil-wetness. Moreover, such affinities are dependent on the presence of divalent cations, which were omitted from the study to simplify both the interpretation of interactions and analysis of the effect of the added x-ray contrasting salt. While this CsI did not appear to substantially influence the results as compared to NaCl, the impact of its binding to oil and mineral surfaces must be evaluated in such micro-CT studies.

7 Summary

Chapter 2 studied interaction forces between carbonate and quartz surfaces in various salts solutions. The largest influence on adhesion between the surfaces occured in the presence of sulphate salts with monovalent cations. Analysis of the depth profile within the carbonate exposed to sulphate anions showed that these ions were incorporated into the carbonate surface to a depth of up to 80 Å. In the case study, it was shown how these surface chemical reactions between such minerals in rock could affect spatial distribution and mobilisation of fines in pores at larger scales.

Chapter 3 analysed the effect of mono- and divalent ion concentration and pH of the aqueous phase on short-term wettability alteration of kaolinite exposed to crude oil. A method for kaolinite substrate preparation suitable for surface chemical experiments was developed. The kaolinite coat is much thinner and smoother than other such model substrates in the literature and remained stable in contact with oil liquids tested. Contact angle experiments showed that kaolinite wettability alteration was substantial, and strongly dependent on ion valency and pH, at total ionic strengths below 0.1 M, while above this threshold the kaolinite typically remained largely water-wet.

Chapter 4 focused on the effect of salinity, ion valency and pH on the adsorption/deposition of crude oil polar compounds onto kaolinite, responsible for its long-term wettability alteration. Microscopic investigations showed that such asphaltenic deposits have the form of nanoparticle aggregates accumulating on edges and/or faces of kaolinite platelets. Increase in salt concentration and pH tended to decrease deposition, in line with contact angle measurements. High sodium concentration limited deposition to platelet edges, whereas high content of dissolved calcium kept both platelet edges and faces cleaner and hindered deposits from penetrating deeper into kaolinite aggregates.

Chapter 5 analysed the wettability alteration of quartz surfaces after primary exposure to brine and crude oil and secondary exposure to brine, the latter step imitating

waterflooding in secondary recovery mode. The primary wettability alteration decreased with increasing salt concentration and pH, as seen in Chapters 3 and 4, and waterflooding was found to further diminish oil-wetness by retraction and detachment of the oil film from the substrate. This removal was similarly greatest for increased concentration and pH of the flooding salt solution. A number of procedures were tested for organic solution rinsing of bulk oil from the substrate to inspect the underlying wettability state. Solvents such as decalin and heptane were found to lead to overestimation of deposit remaining after waterflooding.

Chapter 6 integrated the approaches developed in all previous Chapters, by combining analysis of the wettability alteration of model substrates, of glass and kaolinite-coated glass, with micro-CT determination of the 3D distribution of residual oil in quartz sand packs without and with kaolinite linings after waterflooding. The dependence of the amount of residual oil and the connectivity of these trapped blobs on the flood salinity and presence of kaolinite were found to be well correlated to the corresponding wettability trends. The kaolinite linings increased water-wetness, which led to greater oil residuals, and with more or less connected oil blobs depending on whether bypassing or snap-off was the dominant trapping mechanism.

Potential future research directions

The thesis developed a number of new tools for analysing the molecular-scale interactions of liquid phases with mineral model substrates, ranging from carbonate dissolution-reprecipitation to silicate wettability alteration by crude oil. Further, it integrated these findings with pore-scale observations of phenomena related to oil recovery from cores of the related rock types. In this way, the work served to help bridge the gap in understanding between model systems and real systems. The tools and understanding can now be applied to even more realistic reservoir scenarios. For example, micro-CT analysis of a sandstone reservoir rock after restoration and waterflooding can be integrated with FESEM imaging of its pore walls after flooding to image the remaining asphaltenic deposits indicative of its wettability state. Corresponding drainage, aging and flooding treatment of the analogous model substrates allows the assignment of receding and advancing contact angle, to aid in more predictive network modelling of recovering in the oil reservoir. Further, all wettability analyses in this thesis of sandstone-related systems can be extended to carbonate reservoirs, using calcite and dolomite single crystals as the model substrates.

Bibliography

1. *Colloidally-induced fines release in porous media.* **Khilar, K.C., R.N. Vaidya, R.N. and Fogler, H.S.** 1990, J. Pet. Sci. Eng., Vol. 4, pp. 213-221.

2. *Application of coalbed methan water to oil recovery by low salinity waterflooding.* **Pu, H.; Xie, X.; Yin, P.; Morrow, N.R.** Tulsa, Oklahoma : s.n., 2008. Proceedings of SPE/DOE Improved Oil Recovery Symposium. SPE 113410.

3. *How minerals react with water.* **Brown, G.E.J.** 2001, Science, Vol. 294, pp. 67-70.

4. *Mobilization of quartz fines in porous media.* **Cerda, M. C.** 1988, Clays Clay Miner., Vol. 36, pp. 491-497.

5. **Milliman, J. D.** *Marine Carbonates.* Berlin : Springer-Verlag, 1974. p. 375.

6. **Wilson, J. L.** *Carbonate Facies in Geologic History.* New York : Springer-Verlagmew, 1975. p. 471.

7. **Sellwood, B . W.** Shallow water carbonate environments. [book auth.] H. G. Reading. *Sedimentary Environments and Facies.* New York : Elsevier , 1978, pp. 259-313.

8. *An Atomic Force Microscopy study of the growth of calcite in the presence of sodium sulfate.* **Vavouraki, A.I.; P., Christine V.; P., Andrew; K., Petros G.** 2008, Chemical Geology, Vol. 253, pp. 243–251.

9. *X-ray standing wave investigation of the surface structure of selenite anions adsorbed on calcite.* **Cheng, L.; Lyman, P.F.; Sturchio, N.C.; Bedzyk, M.J.** Surface Science, Vol. 382, pp. 690–695.

10. **Morse, J.W. and Mackenzie, F.T.** *Geochemistry of sedimentary carbonates.* Amsterdam : Elsevier Science Publishers, 1990. p. 707.

11. *Surface speciation of calcite observed in situ by high-resolution X-ray reflectivity.* **Fenter, P.; Geissbuhler, P.; DiMasi, E.; Srajer, G.; Sorensen, L.B.; Sturchio, N.C.** 2000a, Geochimica et Cosmochimica Acta, Vol. 64, pp. 1221-1228.

12. *A surface complexation model of the carbonate mineral-aqueous solution interface.* **Cappellen, van P.; Charlet, L.; Stumm, W.; Wersin, P.** 1993, Geochimica et Cosmochimica Acta, Vol. 57, pp. 3505-3518.

13. *Mechanisms of metal ion sorption on calcite: composition mapping by lateral force microscopy.* **Hay, B.M., Workman, K.R. and Manne, S.** 2003, Langmuir, Vol. 19, pp. 3727-3740.

14. *The zero point of charge of calcite.* **Somasundaran, P. and Agar, G. E.** 1967, J. Colloid Interface Sci., Vol. 24, pp. 433-440.

15. **Israelachvili J., N.** *Intermolecular and Surface Forces.* 2nd. s.l. : Academic Press, 1991.

16. *Phenomenological Theory of Ion Salvation. Effective Radii of Hydrated Ions.* **Nightingale, O.J.** 1959, J. Phys. Chem., Vol. 69, pp. 1381-87.

17. *Coprecipitation of alkali metal ions with calcium carbonate.* **Okumura, M. and Kitano, Y.** 1986, Geochimica et Cosmochimica Acta, Vol. 50, pp. 49-58.

18. *Variations in atmospheric sulphate recorded in stalagmites by synchrotron micro-XRF and XANES analyses.* **Frisia, S.; Borsato, A.; Fairchild, I.J.; Susini, J.** 2005, Earth and Planetary Science Letters , Vol. 235, pp. 729–740.

19. *Effect of inorganic anions on the morphology and structure of magnesium calcite.* **Kralj, D.; J., Kontrec; L., Brecević; G., Falini; V., Nöthig-Laslo.** 2004, Chemistry, Vol. 10, pp. 1647-1656.

20. *Influence of brine composition and fines migration on crude oil/brine/rock interactions and oil recovery.* **Tang, G. and Morrow, N. R.** 1999, J. Pet. Sci. Eng., Vol. 24, pp. 99-111.

21. *Effects of brine composition on wettability and oil recovery of a Prudhoe bay crude oil.* **Yildiz, H.O., Valat, M. and Morrow, N. R.** 1999, J. Can. Pet. Tech., Vol. 38, pp. 26-31.

22. *Effect of wettability on waterflood recovery for crudeoil/oil/brine/rock systems.* **Jadhunandan, P.P. and Morrow, N.R.** 1995, SPE Res. Eng., Vol. 10, pp. 40-46.

23. *Low salinity oil recovery - log inject log.* **Webb, K.J., Black, C.J.J. and Al-Jeel, H.** Tulsa, Oklahoma : s.n., 2004. Proceedings of SPE/DOE Fourteenth Symposium on Improved Oil Recovery. SPE 89379.

24. *Waterflood Performance by Injection of Brine With Different Salinity for Reservoir Cores.* **Zhang, Y., Xie, X. and Morrow, N.R.** Anaheim, CA : s.n., 2007. Proceedings of SPE Annual Technical Conference and Exhibition. SPE 109849.

25. *Low salinity oil recovery: an exciting opportunity for Alaska's North Slope.* **Mcguire, P.; J.R., Chatham; Paskvan, F.K.; Sommer, D.M.; F.H., Carini.** Irvine, CA : s.n., 2005. Proceedings of SPE Western regional Meeting. SPE 93903.

26. *Oil recovery by waterflooding and imbibition - invading brine cation valency and salinity.* **Tang, G. and Morrow, N.R.** Golden, Colorado : s.n., 1999. Proceedings of the International Symposium of the Society of Core Analysts.

27. *Low salinity oil recovery - an experimental investigation.* **Lager, A.; Webb, K. J.; Black, C. J. J.; Singleton, M.; Sorbie, K. S.** Trondheim, Norway : s.n., 2006. The International Symposium of the Society of Core Analysts. SCA 2006-36.

28. *Wettability and oil recovery from carbonates: effects of temperature and potential determining ions.* **Zhang, P. and Austad, T.** 2006, Colloids Surf. A, Physicochem. Eng. Asp., Vol. 279, pp. 179–187.

29. *An x-ray tomography facility for a wide range of mesoscale physics applications.* **Sakellariou, A.; Senden, T.J.; Sawkins, T.J.; Knackstedt, M.A.; Limaye, A.; Arns, C.H.; Sheppard, A.P.; Sok, R.M.** Bellingham, WA : s.n., 2004. U. Bonse (ed.) - Proceedings of SPIE. pp. 166-171. 5535.

30. *Assessment of Bone ingrowth into Porous Biomaterials using micro-CT.* **Jones, A.C.; Arns, C. H.; Sheppard, A. P. ; Hutmacher, D. W. ; Milthorpe, B.; Knackstedt, M. A.** 2007, Biomaterials, Vol. 28, pp. 2491-2504.

31. *Techniques for Image enhancement and segmentation of tomographic images.* **Sheppard, A.P., Sok, R. M. and Averdunk, H.** 2004, Physica A, Vol. 339, pp. 145-151.

32. *Image Registration: Enhancing and calibrating x-ray micro-CT imaging.* **Latham, S., Varslot, T. and Sheppard, A.** Abu Dhabi : s.n., 2008. 22nd International

Symposium of Core Analysts. SCA2008-42.

33. *Overview - clay mineral applications.* **Murray, H.H.** 2000, Appl. Clay Sci. , Vol. 17, pp. 207-221.

34. *Direct determination of contact angles of model soils in comparison with wettability characterization by capillary rise.* **Ramirez-Flores, J. C., Bachmann, J. and Marmur, A.** 2010, J. Hydrol., Vol. 382, pp. 10-19.

35. *Effect of wetting on the dynamics of drainage in porous media.* **Shahidzadeh-Bonn, N.; Tournié, A.; Bichon, S.; Vié, P.; Rodts, S.; Faure, P.; Bertrand, F.; Azouni, A.** 2004, Transport Porous Med., Vol. 56, pp. 209–224.

36. **Goebel, M. O.** *Impact of surface wetting properties on soil physical processes relevant for organic matter decomposition.* Faculty of Natural Sciences, Leibniz University, Hannover : s.n., 2007. p. 132 pp. PhD Thesis.

37. *How water moves in a water repellent sandy soil. 1. Potential and actual water repellency.* **Dekker, L. W. and Ritsema, C. J.** 1994 : s.n., Water Resour. Res., Vol. 30, pp. 2507–251.

38. *Wettability and its effect on oil recovery.* **Morrow, N.R.** 1990, J. Pet. Tech., Vol. 42, pp. 1476-1484.

39. *Oil Recovery by Low Salinity Brine Injection: Laboratory Results on Outcrop and Reservoir Cores.* **Boussour, S.; Cissokho, M.; Cordier, P.; Bertin, H.; Hamon, G.** New Orleans, Luisiana : Society of Petroleum Engineers, 4-7 October 2009. SPE Annual Conference and Exhibition. SPE 124277-PP.

40. *Adsorption of a few heavy metals on natural and modified kaolinite and montmorillonite: A review.* **Bhattacharyya, K. G. and Gupta, S. S.** 2008, Adv. Colloid Interface Sci., Vol. 140, pp. 114-131.

41. *Clay mineral-enhanced bioremediation of marine oil pollution.* **Warr, L. N.; Perdrial, J. N.; Lett, M. C.; Heinrich-Salmeron, A.; Khodja, M.** 2009, Appl. Clay Sci., Vol. 46, pp. 337-345.

42. *Remediation technologies for metal-contaminated soils and groundwater: an evaluation.* **Mulligan, C. N., Yong, R. N. and Gibbs, B. F.** 2001, Engineering

Geology, Vol. 60, pp. 193-207.

43. *Wettability literature survey: Part I. Rock/oil/brine interactions and the effect of core handling on wettability.* **Andreson, W.G.** 1986, J. Pet. Technol., Vol. 38, pp. 1125-1144.

44. *Asphaltenes and crude oil wetting – the effect of oil composition.* **Buckley, J. S.; Liu, Y.; Xie, X.; Morrow, N. R.** 1997, SPE Journal, pp. 107-119. SPE 35366.

45. *The chemical and physical structure of petroleum: effects on recovery operations.* **Speight, J.G.** 1999, J. Pet. Sci. Eng., Vol. 22, pp. 3-15.

46. **Mullins, O.C. and Sheu, E.Y.** *Structure and Dynamics of Asphaltenes.* New York : Springer, 1998.

47. *Contact angles of aluminosilicate clays as affected by relative humidity and exchangeable cations.* **Shang, J.; Flury, M.; Harsh, J. B.; Zollars, L. R.** 2010, Colloid Surf. A, Vol. 353, pp. 1-9.

48. *Surface force measurements at the basal planes of ordered kaolinite particles.* **Gupta, V. and Miller, J. D.** 2010, J. Colloid Interface Sci., Vol. 344, pp. 362–371.

49. *Influence of exchangeable cations on the surface free energy of kaolinite as determined from contact angles.* **Jańczuk, B.; Chibowski, E.; Hajnos, M.; Bialopiotrowicz, T.; Stawinski, J.** 1989, Clays Clay Miner., Vol. 37, pp. 269-272.

50. *Development and application of a new sessile drop contact angle method to assess soil water repellency.* **Bachmann, J., Ellies, A. and Hartge, K. H.** 2000, J. Hydrol., Vol. 231, pp. 66-75.

51. *Role of crystal structure in flotation separation of diaspore from kaolinite, pyrophyllite and illite.* **Hu, Y., Lui, X. and Xu, Z.** 2003, Miner. Eng., Vol. 16, pp. 219-227.

52. *Flocculation of kaolinite clay suspensions using a temperature-sensitive polymer.* **Li, H.; Long, J.; Xu, Z.; Masliyah, J. H.** 2007, AIChE J., Vol. 53, pp. 479-488.

53. *Baseline studies of the Clay Mineral Society Source Clays: Colloid and Surface Phenomena.* **Wu, W.** 49, 2001, Clays Clay Miner., pp. 446-452.

54. *Comparison of different methods to measure contact angles of soil colloids.* **Shang, J.; Flury, M.; Harsh, J. B.; Zollars L.R.** 2008, J. Colloid Interface Sci., Vol. 238, pp. 299-307.

55. *Improving oil displacement efficiency by wettability adjustment.* **Wagner, O.R. and Leach, R.O.** 1956, Trans. AIME , Vol. 216, pp. 65-72.

56. *Crude oil/brine contact angles on quartz glass.* **Xie, X., Morrow, N. R. and Buckley, J. S.** Calgary, Canada : s.n., September 1997. Proceedings of the International Symposium of the Society of Core Analysts.

57. *Alteration of wetting of mica surfaces.* **Liu, L. and Buckley, J. S.** 1999, J. Pet. Sci. Eng., Vol. 24, pp. 75-83.

58. *Mechanisms for contact angle hysteresis and advancing contact angles.* **Yang, S.-Y.; Hirasaki, G. J.; Basu, S.; Vaidya, R.** 1999, J. Pet. Sci. Eng., Vol. 24, pp. 63-73.

59. *Fundamental studies of crude oil–surface water interactions and its relationship to reservoir wettability.* **Drummond, C. and Israelachvili, J.** 2004, J. Pet. Sci. Eng., Vol. 45, pp. 61-81.

60. *Measurement of critical disjoining pressure for dewetting of solid surfaces.* **Basu, S. and Sharma, M. M.** 1996, J. Colloid Interface Sci., Vol. 181, pp. 443-455.

61. *Influence of electrical surface charges on the wetting properties of crude oils.* **Buckley, J.S., Takamura, K. and Morrow, N.R.** 1989, SPE Res. Eng., pp. 332-340.

62. **Buckley, J.S. and Morrow, N.R.** An overview of crude oil adhesion phenomena. [book auth.] H., Lecourtier Toulhoat. *Physical Chemistry of Colloids and Interfaces in Oil Production.* Paris : Éditions Technip, 1992, pp. 39-45.

63. *Contact angle measurement on rough surfaces.* **Meiron, T. S., Marmur, A. and Saguy, I. S.** 2004, J. Colloid Interface Sci., Vol. 274, pp. 637–644.

64. *Predicting the wettability of quartz surfaces exposed to dense nonaqueous phase liquids.* **Zheng, J.; Behrens, S.H.; Borkovec, M.; Powers, S.E.** 2001, Environ. Sci. Technol., Vol. 35, pp. 2207-2213.

65. *Wettability alteration of kaolinite exposed to crude oil in salt solutions.* **Lebedeva,**

E.V. and Fogden, A. 2011, Colloids Surf. A, Vol. 377, pp. 115-122.

66. *Wettability: fundamentals and surface forces.* **Hirasaki, G.J.** 1991, SPE Form. Eval., pp. 217-227.

67. *Baseline studies of The Clay Minerals Society source clays: Powder x-ray diffraction analyses.* **Chipera, S. J. and Bish, D. L.** 2001, Clays Clay Miner., Vol. 49, pp. 398–409.

68. *Baseline studies of the clay minerals society source clays: cation exchange capacity measurements by the ammonia-electrode method.* **Borden, D. and Giese, R.F.** 2001, Clays Clay Miner., Vol. 49, pp. 444-445.

69. *Sampling and analysis of KGa-1b well-crystallized kaolin source clay.* **Pruett, R.J. and Webb, H.L.** 1993, Clays Clay Miner., Vol. 41, pp. 514-519.

70. *The effect of different crude oil/brine/rock combinations on wettability through spontaneous imbibition.* **Tie, H.G., Tong, Z.X. and Morrow, N.R.** Pau, France : s.n., 2003. Proceedings of the Society of Core Analysts. Paper 2.

71. *Electrokinetic properties of kaolinite in mono- and multivalent electrolyte solutions.* **Alkan, M., Demirbas, O. and Dogan, M.** 2005, Microporous Mesoporous Mater., Vol. 83, pp. 51–59.

72. *Mechanism of formation of two-dimensional crystals from latex particles on substrates.* **Denkov, N.; Velev, O.; Kralchevski, P.; Ivanov, I.; Yoshimura, H.; Nagayama, K.** 1992, Langmuir, Vol. 8, pp. 3183–3190.

73. *Contact angle and their hysteresis as a measure of liquid-solid.* **Extrand, C.W.** 2004, Langmuir, Vol. 20, pp. 4017-4021.

74. *Wettability and morphology of mica surfaces after exposure to crude oil.* **Buckley, J.S. and Lord, D.L.** 2003, J. of Pet. Sci. Eng., Vol. 39, pp. 261-273.

75. **Buckley, J. S. and Morrow, N. R.** *Wettability and imbibition: Microscopic distribution of wetting and its consequences at the core and field scales.* 2003. p. 184, Final report. US DOE contract DE-AC26-99BC15204.

76. *Recovery of oil by spontaneous imbibition.* **Morrow, N.R. and Mason, G.** 2001,

Curr. Opin. Colloid Interface, Vol. 6, pp. 321-337.

77. *A pore-level scenario for the development of mixed wettability in oil reservoirs.* **Kovscek, A.R., Wong, H. and Radke, C.J.** 1993, AIChE J., Vol. 39, pp. 1072-1085.

78. *Patterned wettability of oil and water in porous media.* **Kumar, M. and Fogden, A.** 2010, Langmuir, Vol. 26, pp. 4036-4047.

79. *A pore-level scenario for the development of mixed wettability in oil-reservoirs.* **Durand, C. and Rosenberg, E.** 1993, AIChE J., Vol. 39, pp. 1072-1085.

80. *Study of asphaltenes adsorption onto different minerals and clays. Part 1. Experimental adsorption with UV depletion detection.* **Dudasova, D.; Simon,S.; Hemmingsen,P.V.; Sjoblom, J.** 2008, Colloids Surf. A, Vol. 317, pp. 1-9.

81. *Adsorption of asphaltenes and water on reservoir rock minerals.* **Collins, S.H. and Melrose, J.C.** Denver, USA : International Symposium on Oilfield and Geothermal Chemistry, 1983. Paper SPE 11800.

82. *Adsorption of asphaltenes from toluene on mineral surface.* **Marczewski, A.W. and Szymula, M.** 2002, Colloids Surf. A, Vol. 208, pp. 259-266.

83. *Asphaltene adsorption on clays and crude oil reservoir rocks.* **Pernyeszi, T.; Patzko, A.; Berkesi, O.; I., Dekany.** 1998, Colloids Surf. A, Vol. 137, pp. 373-384.

84. *Wettability contrasts in kaolinite and illite clays: Characterization by infrared and X-ray absorption spectroscopies.* **Bantignies, J.L., Moulin, C.C.D. and Dexpert, H.** 1997, Clays Clay Miner., Vol. 45, pp. 184-193.

85. *Use of XPS for reservoir sandstone wettability evaluation. Application to kaolinite and illite.* **Durand, C. and Beccat, P.** 1998, J. Pet. Sci. Eng., Vol. 20, pp. 259-265.

86. *Contact angle hysteresis and the stability of wetting changes induced by adsorption from crude oil.* **Xie, X., Morrow, N.R. and Buckley, J.S.** 2002, J. Pet. Sci. Eng., Vol. 33, pp. 147-159.

87. *Investigating the role of crude oil components on wettability alteration using atomic force microscopy.* **Basu, S. and Sharma, M.M.** Houston : s.n., 1997. SPE International Symposium on Oilfield Chemistry. SPE 37231.

88. *An AFM study of the morphological features that affect wetting at crude oil-water-mica interfaces.* **Lord, D.L. and Buckley, J.S.** 2002, Colloids Surf. A, Vol. 206, pp. 531-546.

89. *AFM study of mineral wettability with reservoir oils.* **Kumar, K., Dao, E. and Mohanty, K.K.** 2005, J. Colloid Interface Sci., Vol. 289, pp. 206-217.

90. *The role of interfacial rheology in reservoir mixed wettability.* **Freer, E.M., Svitova, T. and Radke, C.J.** 2003, J. Pet. Sci. Eng., Vol. 39, pp. 137-158.

91. *Asphaltene adsorption and desorption from mineral surfaces.* **Dubey, S.T. and Waxman, M.H.** 1991, SPE Res. Eng., pp. 389-395.

92. **Hansen, C.M.** *Hansen Solubility Parameters: A User's Handbook.* 2nd. s.l. : CRC Press, 2007.

93. *Colloid chemistry of in-situ clay-induced formation damage.* **Tchistiakov, A.A.** Lafayette, USA : s.n., 2000. SPE International Symposium on Formation Damage Control. SPE 58747.

94. *Experimental investigation of deposition of crude oil components in brine-filled pores.* **Fogden, A.** Noordwijk, The Netherlands : s.n., 2009. Proceedings of the Society of Core Analysts. Paper 23.

95. *A small angle neutron scattering study of the adsorbed asphaltene layer in water-in-hydrocarbon emulsions: structural description related to stability.* **Jestin, J.; Simon, S.; Zupancic, L.; Barre, L.** 2007, Langmuir, Vol. 23, pp. 10471-10478.

96. *An atomic force microscopy study of asphaltenes on mica surfaces. Influence of added resins and demulsifiers.* **Ese, H.-M.; Sjöblom, J.; Djuve, J.; Pugh, R.** 2000, Colloid Polym. Sci., Vol. 278, pp. 532-538.

97. *Oil recovery by sequential waterflooding of mixed-wet sandstone and limestone.* **Loahardjo, N., Xie, X. and Morrow, N.R.** 2010, Energy Fuels, Vol. 24, pp. 5073-5080.

98. *Spontaneous imbibition for mixed-wettability states in sandstones induced by adsorption from crude oil.* **Tong, Z.X., Morrow, N.R. and Xie, X.** 2003, J. Pet. Sci. Eng., Vol. 39, pp. 351-361.

99. *Mobilization of fine particles during flooding of sandstones and possible relation to enhanced oil recovery.* **Fogden, A.; Kumar, M.; Morrow, N.M.; Buckley, S. J.** 2011, Energy and Fuels, Vol. 25, pp. 1605-1616.

100. *Modeling microbial transport in porous media: traditional approaches and recent developments.* **Tufenkji, N.** 2007, Adv. Water Resour., Vol. 30, pp. 1455-1469.

101. *Effects of solution chemistry on straining of colloids in porous media under unfavorable conditions.* **Chongyang, S.; Yuanfang, H.; Baoguo, L.; Yan, J.** 2008, Water Resour. Res., Vol. 44, p. W05419.

102. *Digital Rock Physics: 3D imaging of core material and correlations to acoustic and flow properties.* **Knackstedt, M.A.; Latham, S.; Madadi, M.; Sheppard, A.; Varslot, T.; Arns, C.** 2009, The Leading Edge, Vol. 28, pp. 28-33.

103. *Flow in porous media-pore-network models and multiphase flow.* **Blunt, M.J.** 2001, Curr. Opin. Colloid Interface Sci., Vol. 6, pp. 197-207.

104. *Magnitude and detailed structure of residual oil saturation.* **Chatzis, I., Morrow, N. and Lim, H.L.** s.l. : Society of Petroleum Engineers, 1983, SPE Journal, Vol. 23, pp. 311-326.

105. *Mechanisms of the displacement of one fluid by another in a network of capplilary ducts.* **Lenormand, R., Zarcone, C. and Sarr, A.** 1983, J. of Fluid Mech., Vol. 135, pp. 337-353.

106. *Entrapment and mobilization of residual oil in bead pack.* **Morrow, N., Chatzis, I. and Taber, J.J.** 1988, SPE Res. Eng., Vol. 3, pp. 927-934.

107. *Effect of cappilary number on the microstructure of residual oil in strongly water-wet sandstones.* **Chatzis, I., Kuntamukkula, M.S. and Morrow, N.R.** 1988, SPE Res. Eng., Vol. 3, pp. 902-912.

108. *Correlation of capplilary number relationships for sandstone.* **Chatzis, I. and Morrow, N.R.** 1984, SPE Journal, Vol. 25, pp. 555-562.

109. **Salathiel, R. A.** 1973, Trans. Am. Inst. Min. Metall. and Pet. Eng., Soc. Min. Eng. AIME, Vol. 255, pp. 1216-1224.

110. *Field-wide variations of wettability.* **Hamon, G.** Dallas, Texas : s.n., 2000. SPE Annual technical conference and exhibition. SPE 63144.

111. *Empirical measures of wettability in porous media and the relationship between them derived from pore-scale modelling.* **Dixit, A. B.; Buckley, J.S.; McDougall, S.R.; Sorbie, K.S.** 2000, Trans. in Porous Med., Vol. 40, pp. 27-54.

112. *Reconstruction of Berea sandstone and pore-scale modeling of wettability effects.* **Øren, P. -E. and Bakke, S.** 2003, J. of Pet. Sci. Eng., Vol. 39, pp. 177-199.

113. **Sheppard, A. P., Sok, R.M. and Averdunk, H.** Toronto, Canada : s.n., 2005. Proceedings of the 2005 International Symposium of the Society of Core Analysts. SCA 2005-20.

114. *X-ray computed microtomography studies of fluid partitioning in drainage and imbibition before and after gel placement: disproportionate permeability reduction.* **Seright, R.S., Prodanovic, M. and Lindquist, W.B.** 2006, SPE Journal.

115. *Visualizing and quantifying the residual phase in core material.* **Kumar, M.; Senden, T.J.; Sheppard, A.P.; Middleton, J.P.; Knackstedt, M.A.** 2010, Petrophysics, Vol. 51, pp. 323-332.

116. **Middleton, J.P., Avendruck, H. and Sheppard, A. P.** Mango User Guide. [Online] 2010. http://people.physics.anu.edu.au/~jpm110/Guides/UGforappMaths.pdf.

117. *Wetting phase connectivity and irreducible saturation in simple granular media.* **Bryant, S. and Johnson, A.** 2003, J. of Colloid Interface Sci., Vol. 263, pp. 572-579.

118. *Remobilization of Residual Non-Aqueous Phase Liquid in Porous Media by Freeze−Thaw Cycles.* **Singh, K.; Niven, K.R.; Senden, T.J.; Turner, M.L.; Sheppard, A.S.; Middleton, J.P.; Knackstedt, M.A.** 2011, Enviro. Sci. Technol., Vol. 45, pp. 3473-3478.

119. *Wettability of porous surfaces.* **Cassie, A.B.D. and Baxter, S.** 1944, Transactions of the Faraday Society, Vol. 40, pp. 546-551.